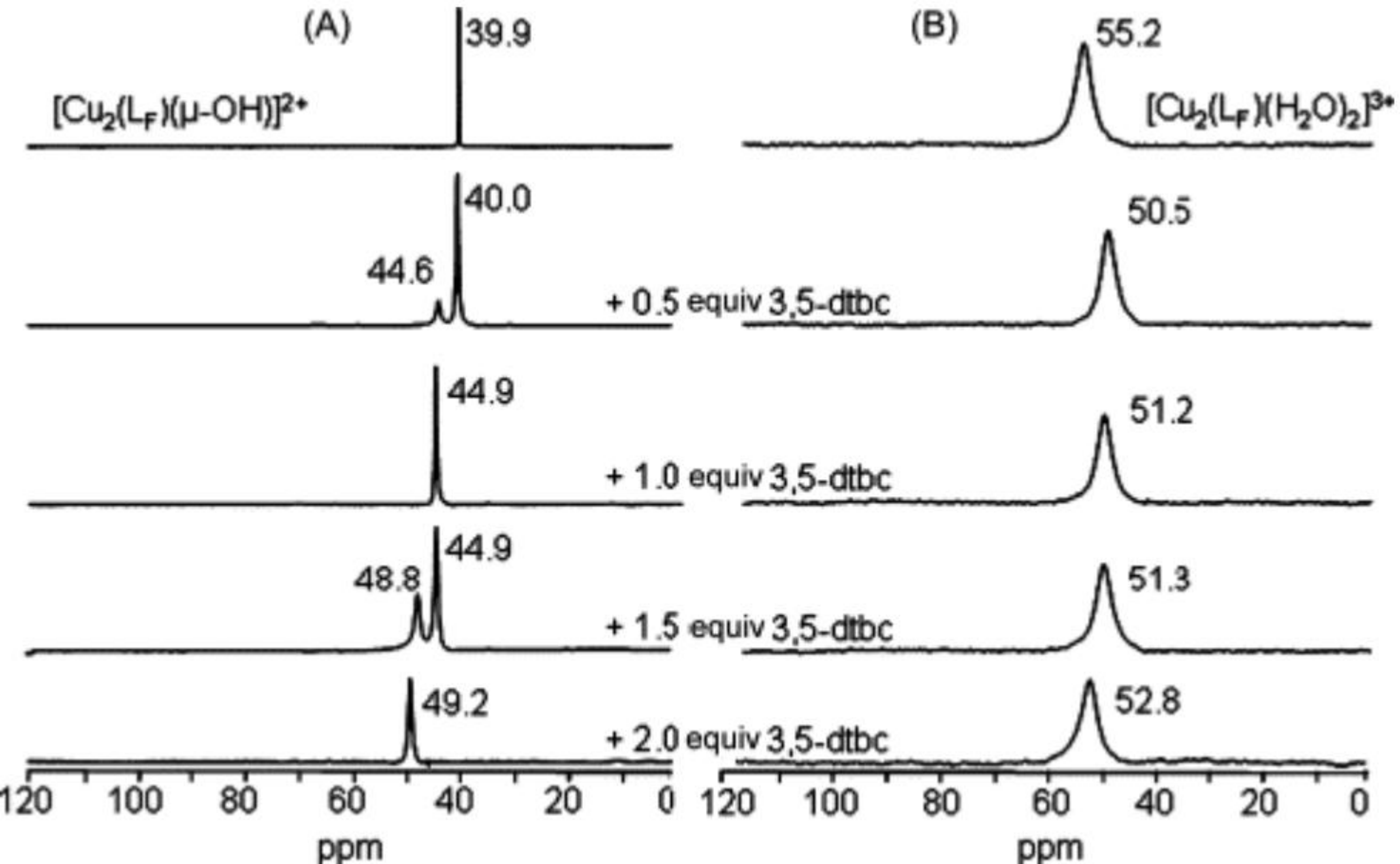
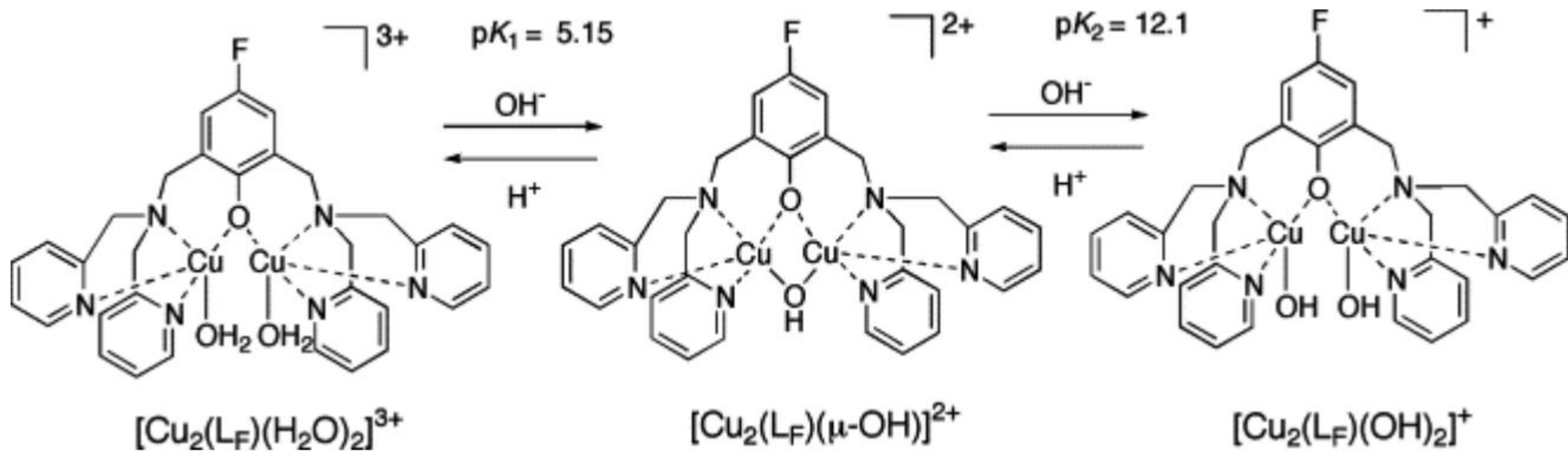


1. Download: [Download full-size image](#)



1. [Download: Download full-size image](#)



Volume 30(1) Issues 1-4 April 2009

ISSN 0277-0420



COORDINATION CHEMISTRY REVIEWS

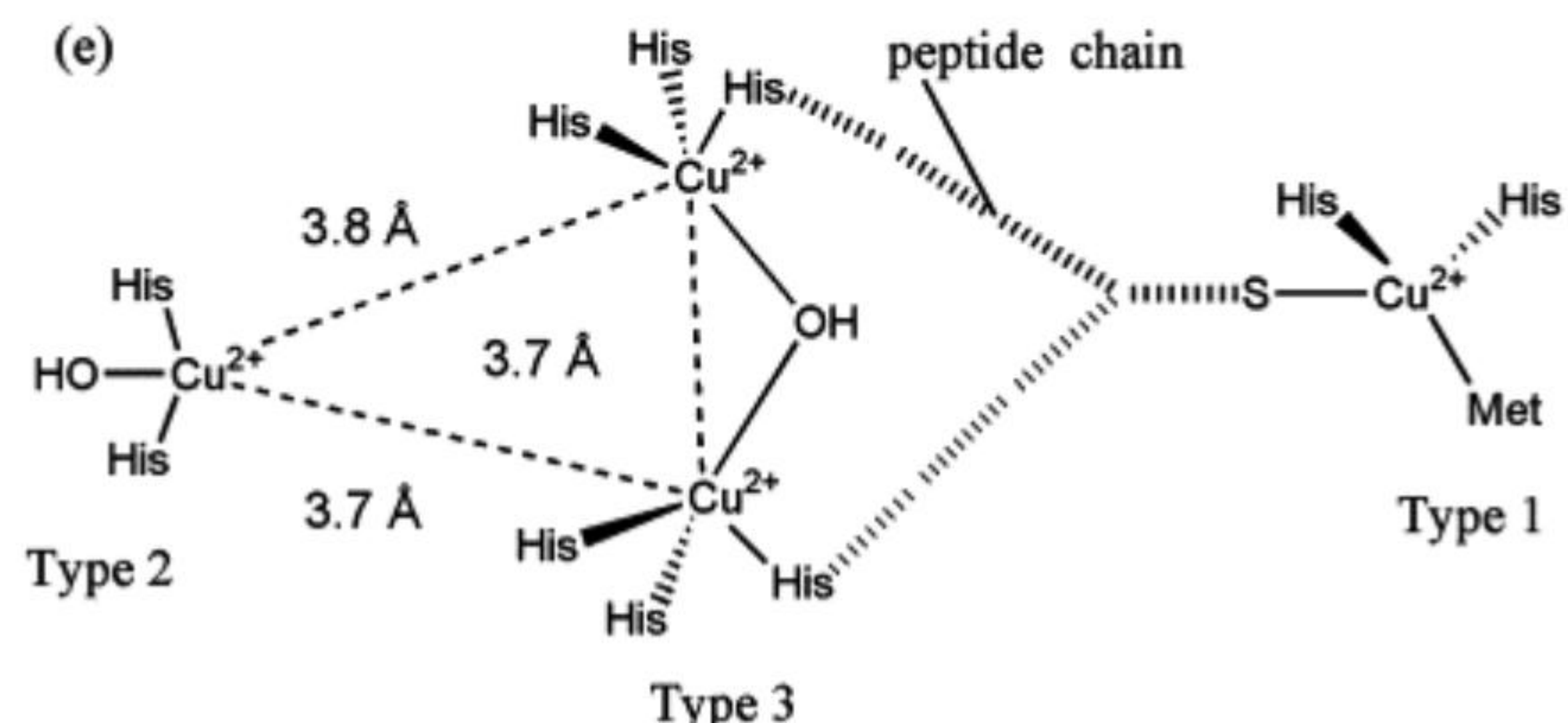
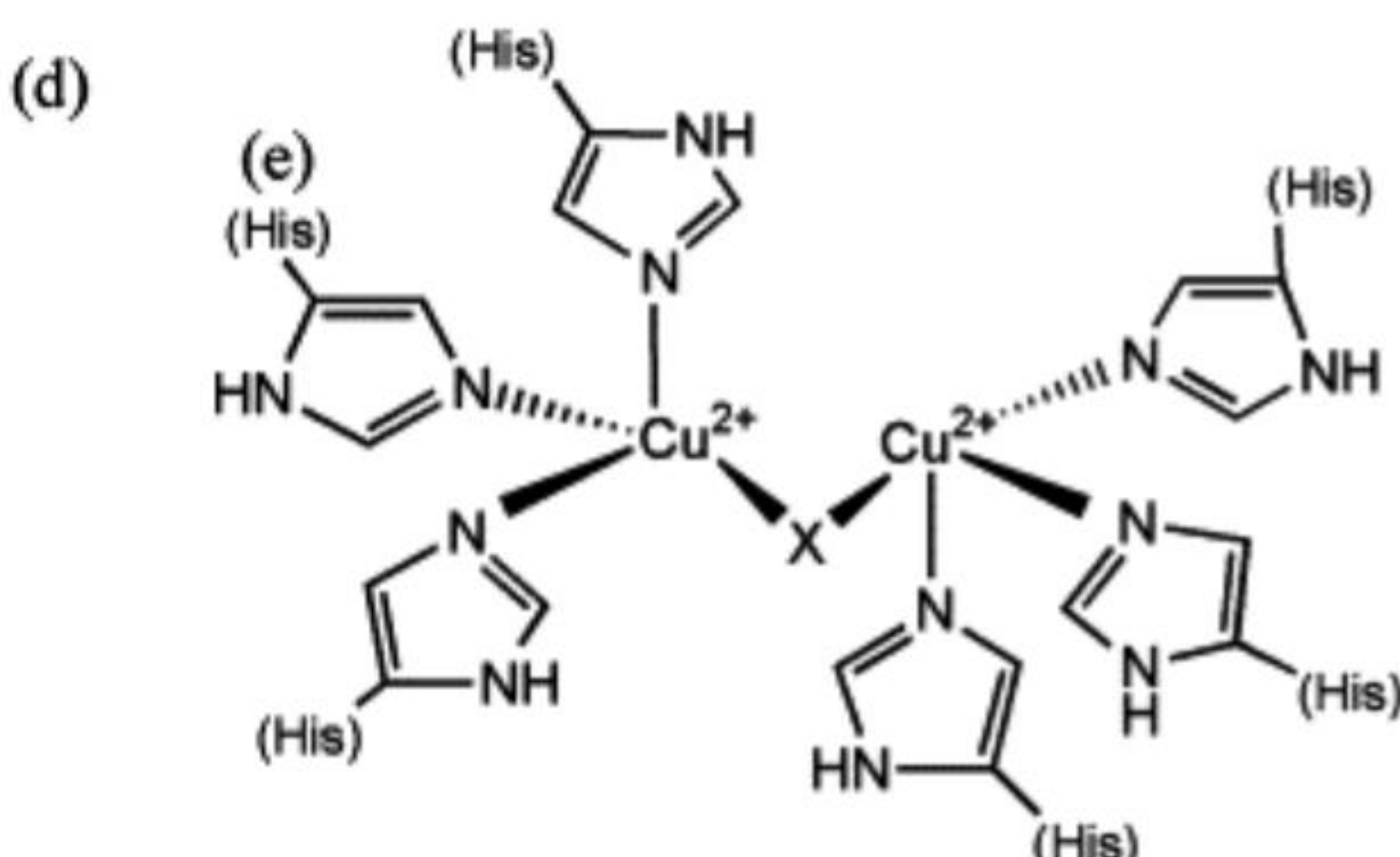
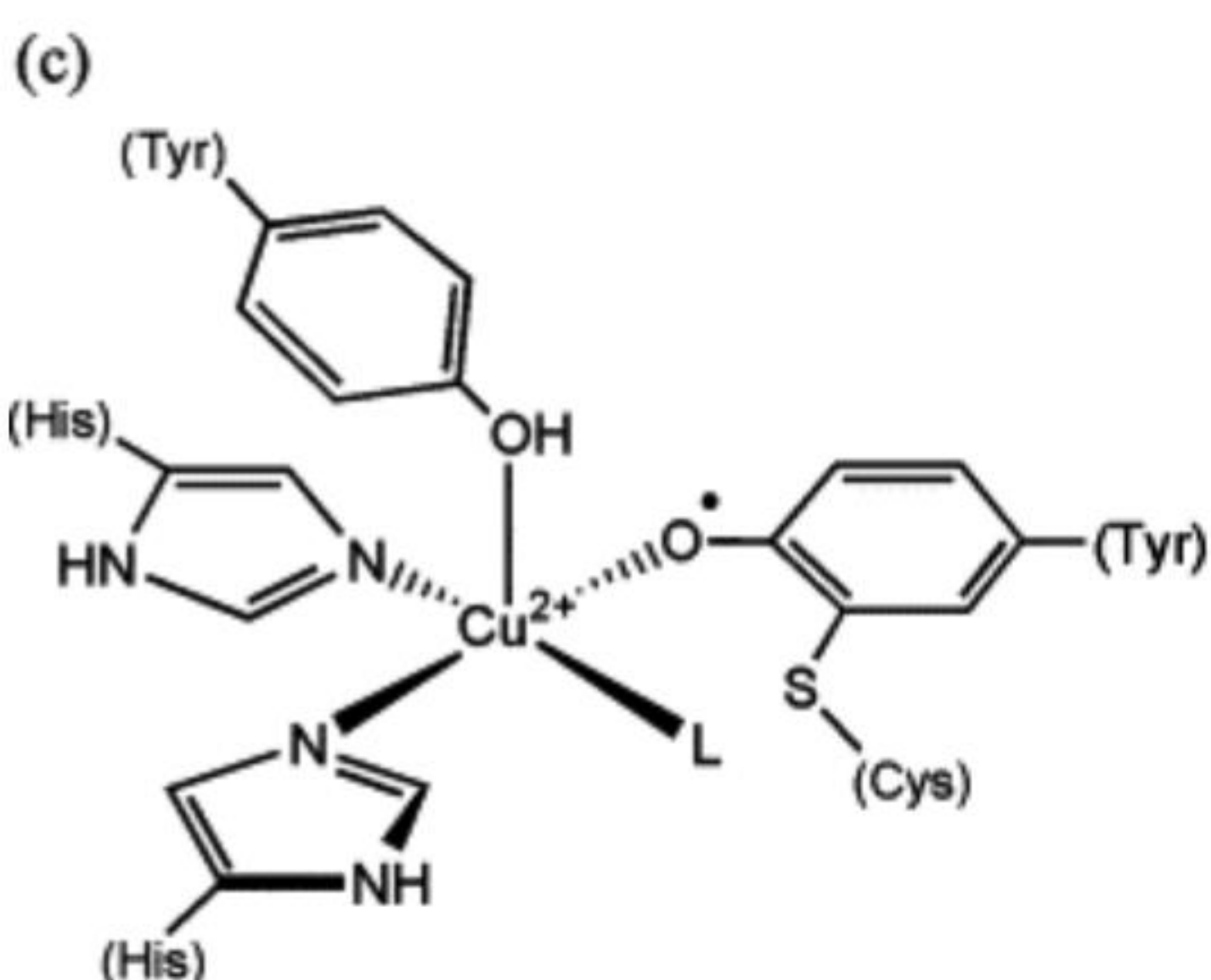
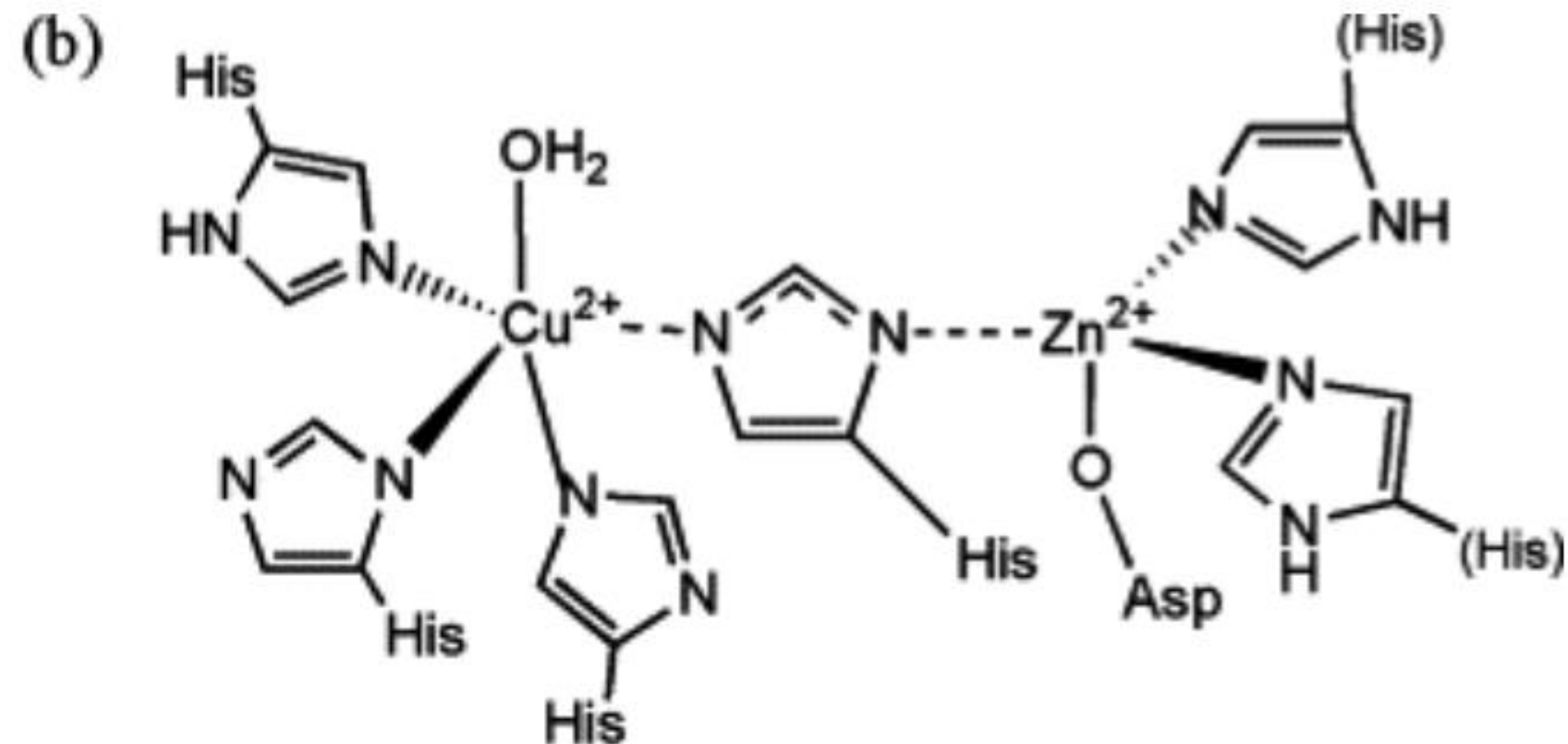
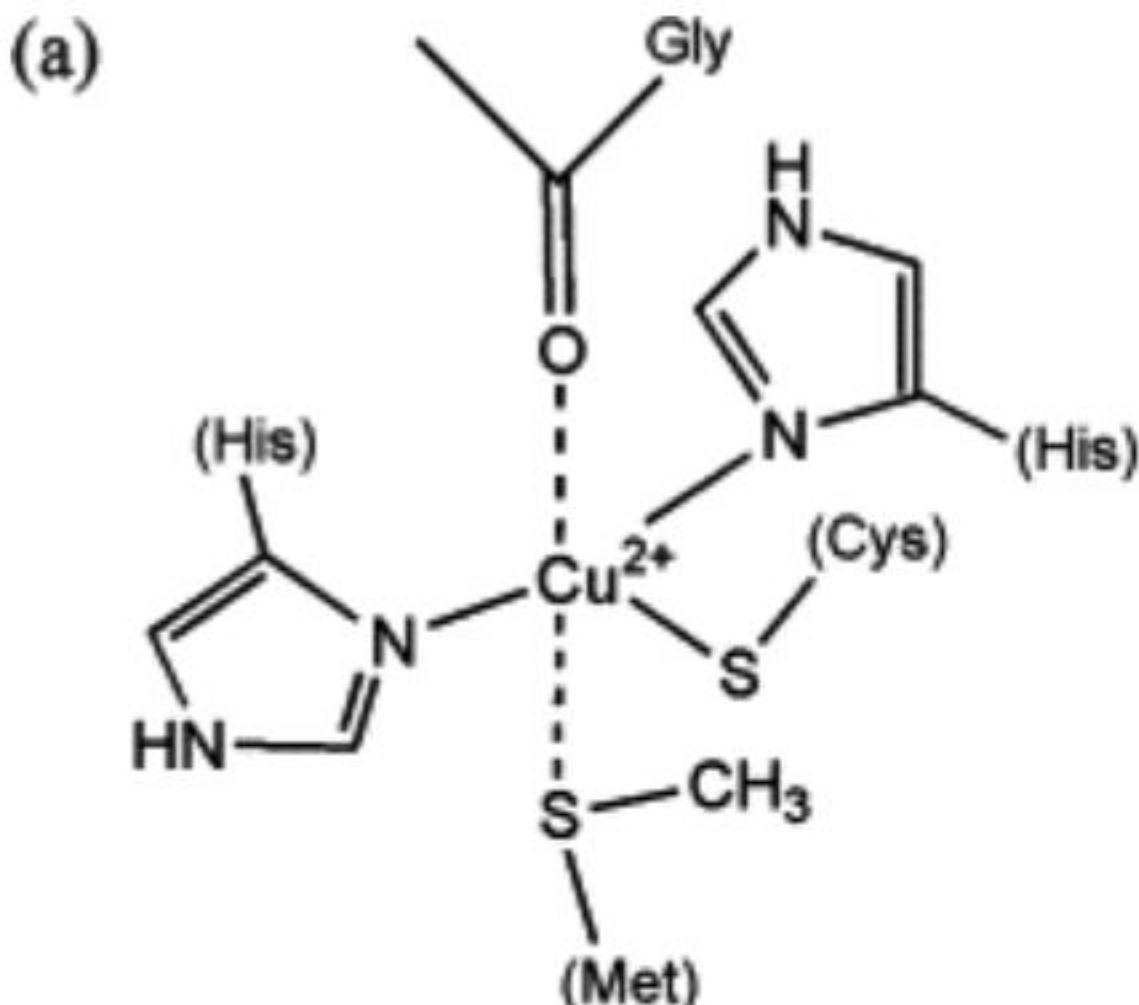
Editor: ALLEN LEVINE

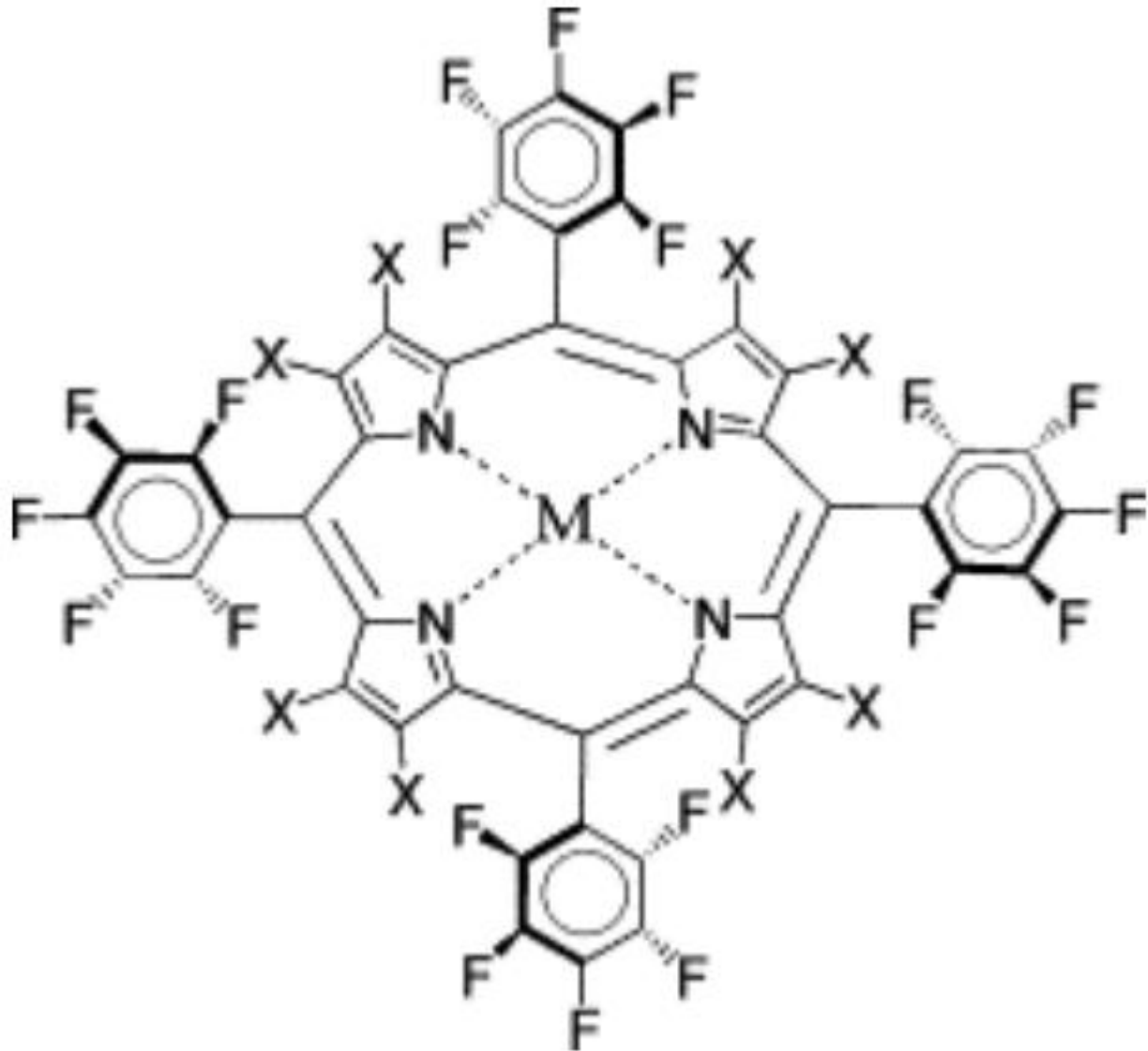
Associate Editors:
Sabine and Olav Olsufieff
www.wiley.com/jcr/CCR

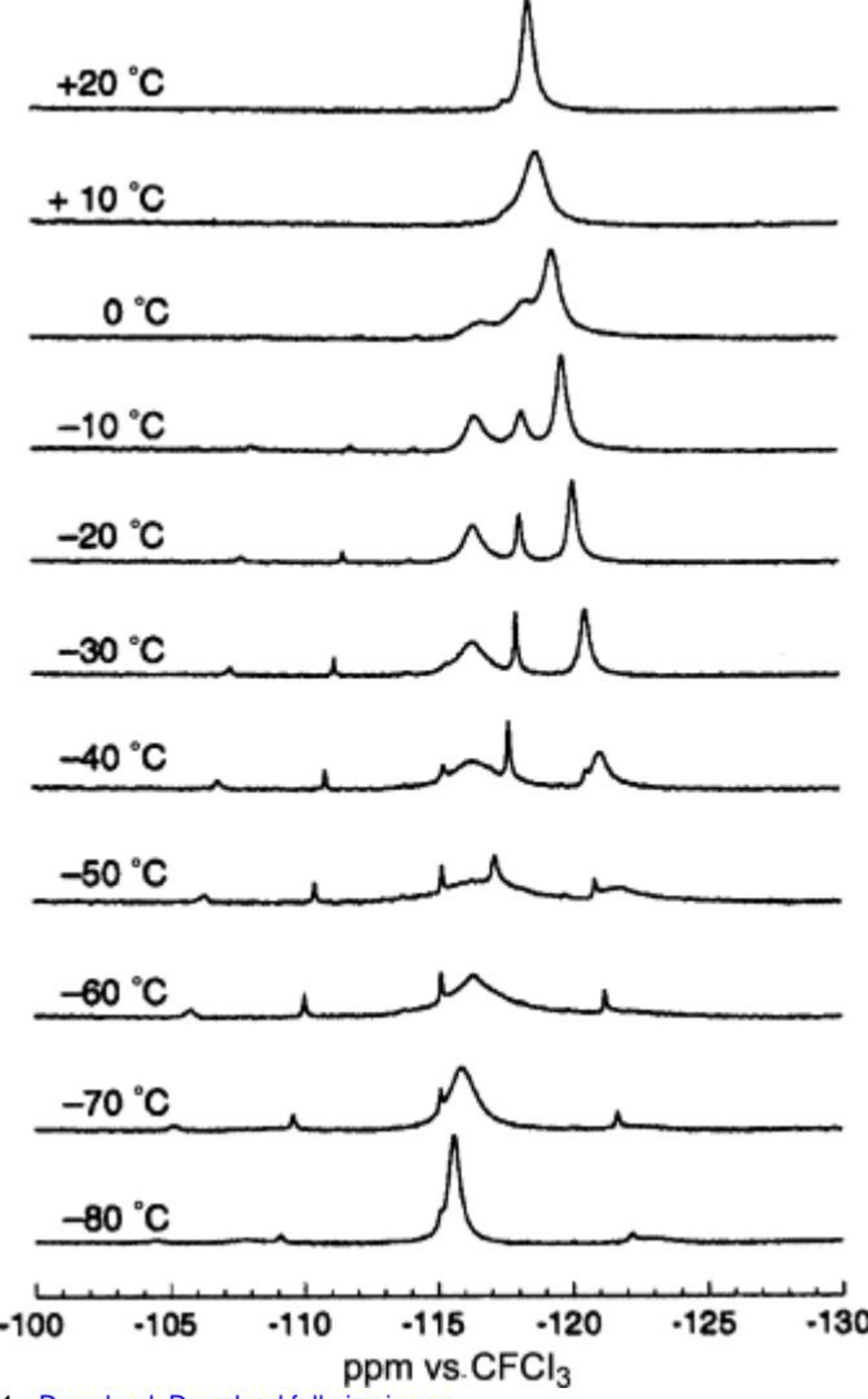
Online submission and review system available at
www.manuscriptcentral.com



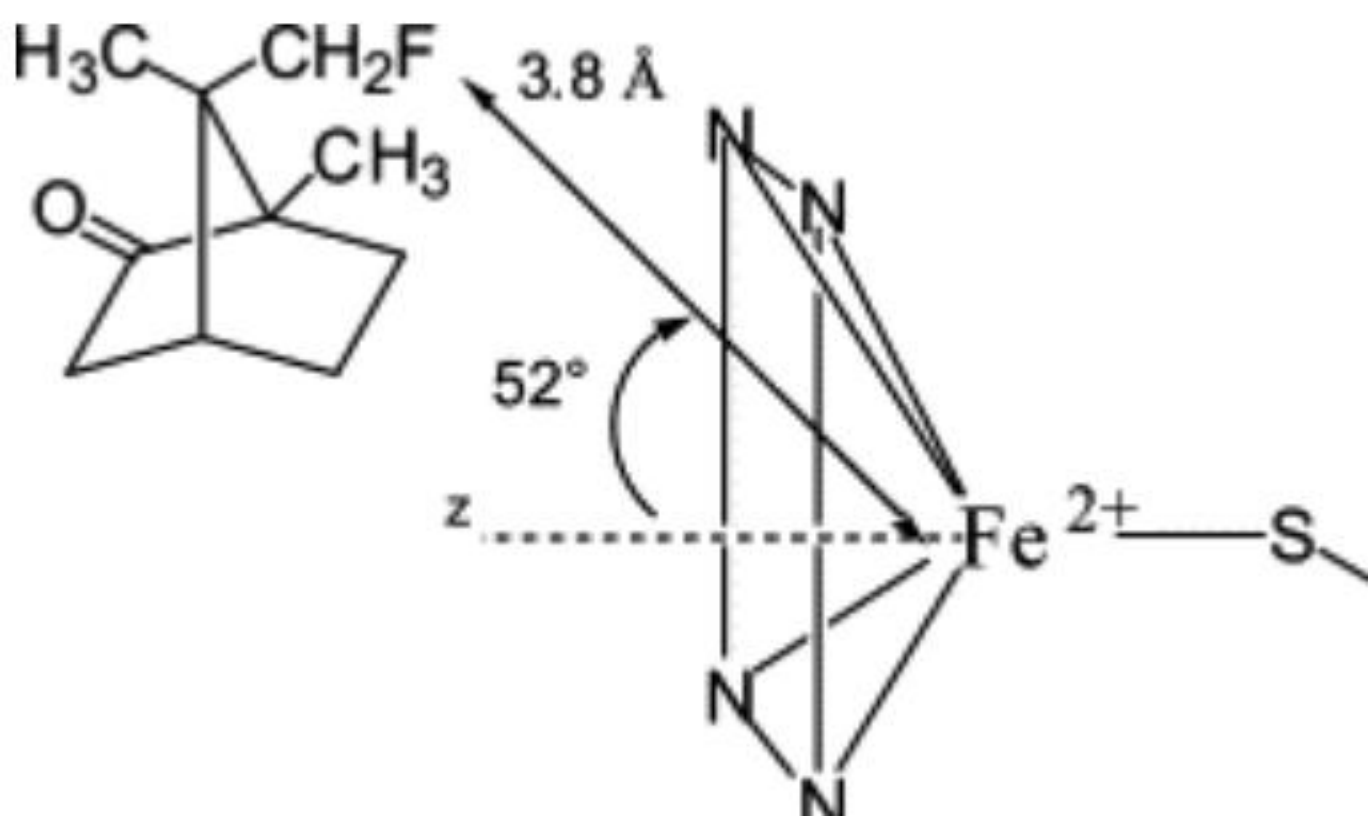
[View details](#)



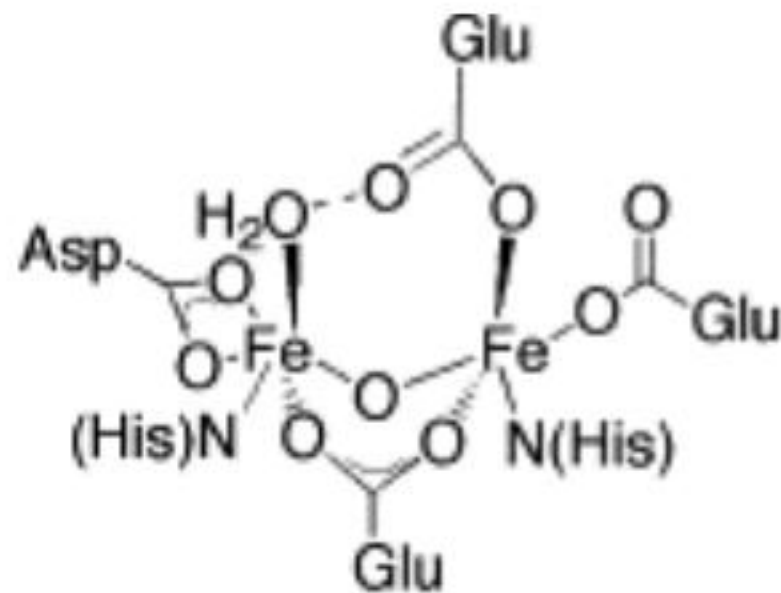
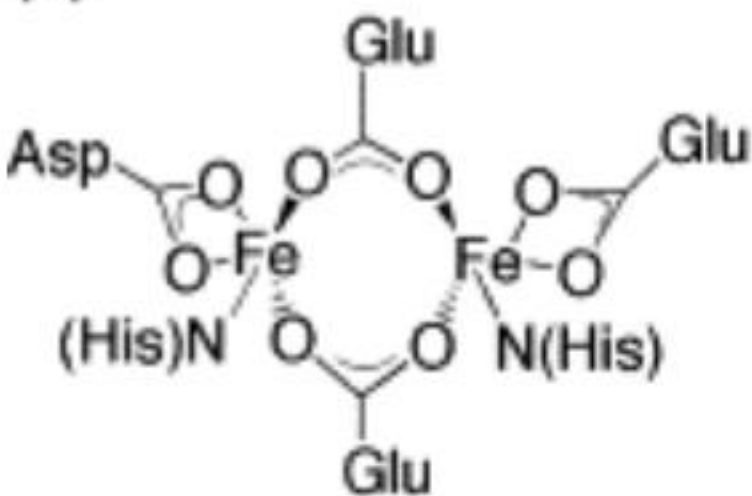




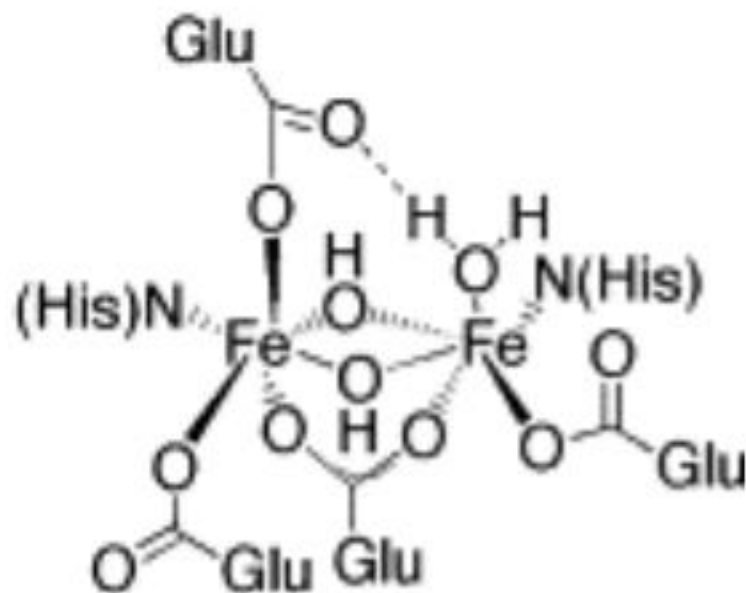
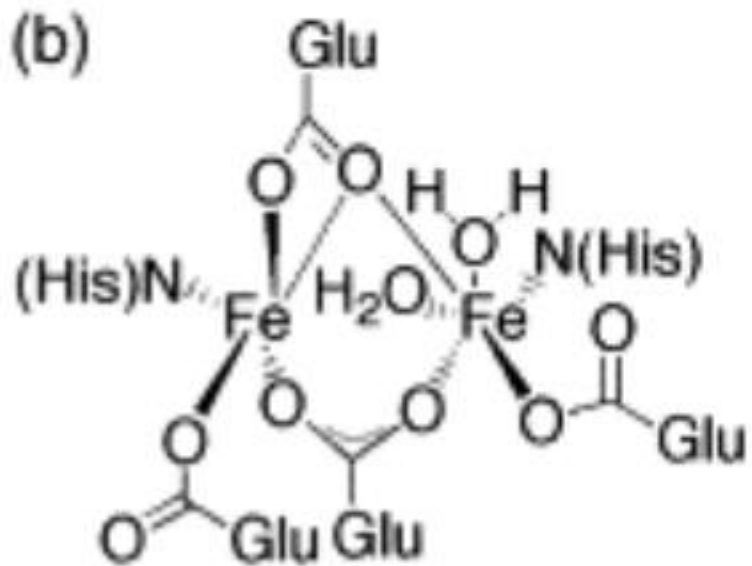
1. [Download: Download full-size image](#)



(a)

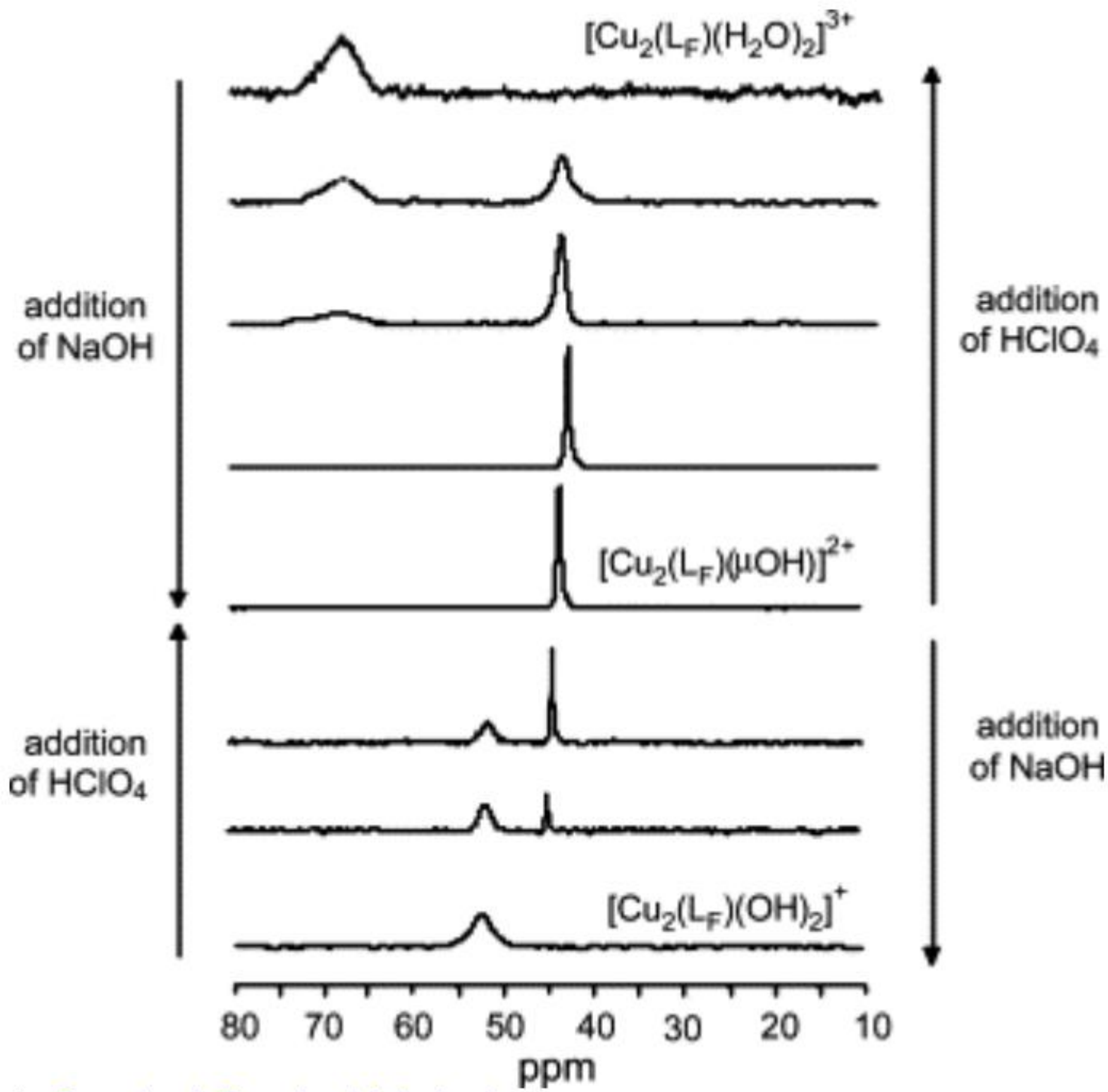


(b)

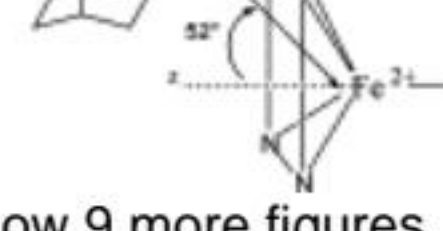
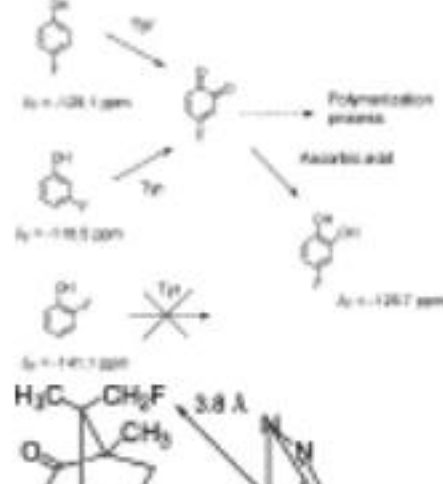
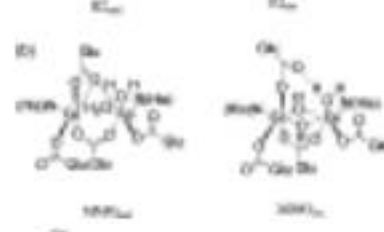
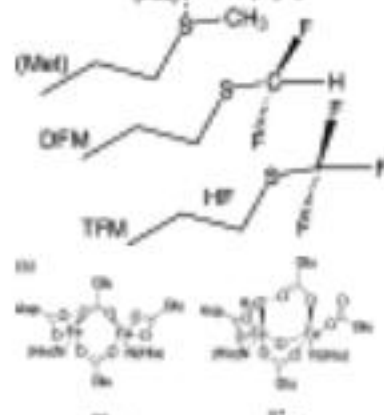
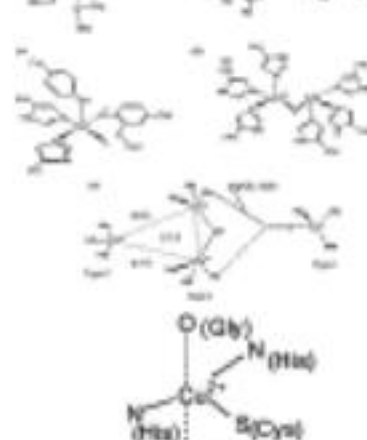
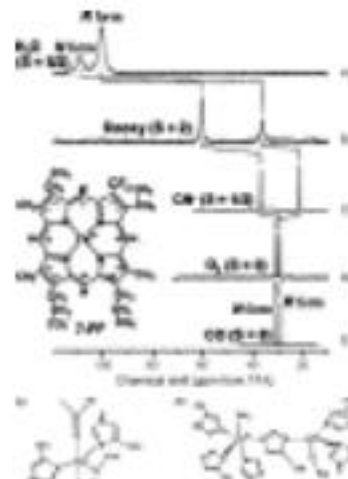
 MMO_{red} MMO_{ox}



[View details](#)



1. [Download full-size image](#)



NON SOLUS

Volume 39(1) March 2010 1–282 ISSN 0277-047X

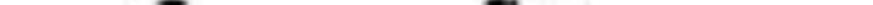
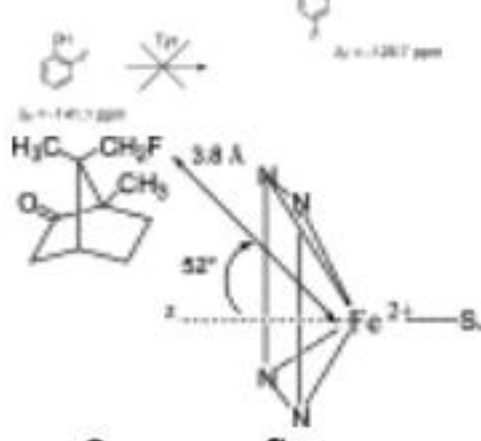
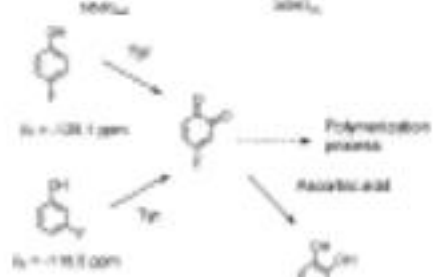
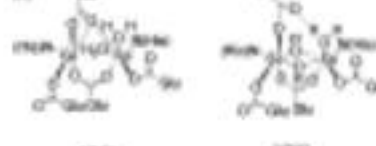
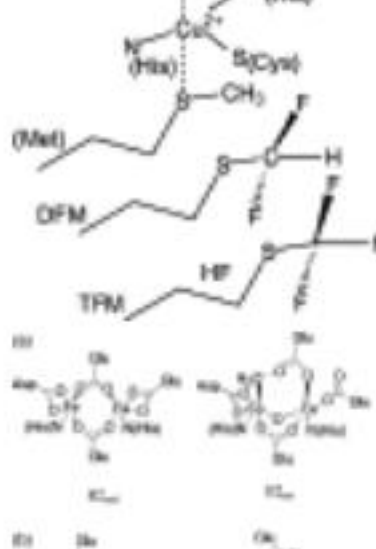
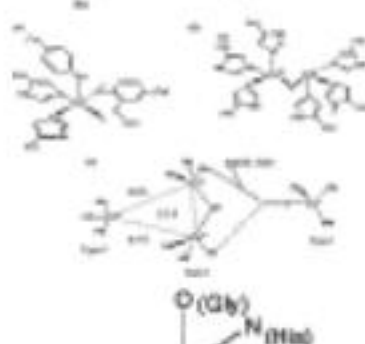
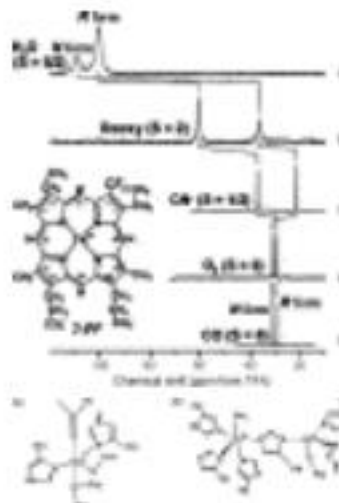
ISSN 1469-7770

COORDINATION CHEMISTRY REVIEWS

Editor: ALI JAFAR

Associate editor of
SelectedTopics
www.wiley.com/10.1002/ctrc

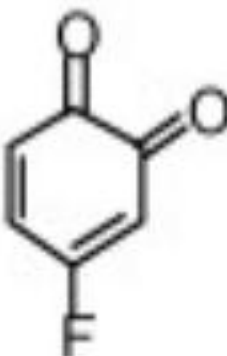
Submit manuscripts to the journal online at www.manuscriptcentral.com



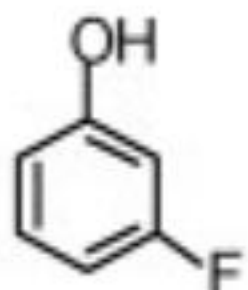


Tyr

$\delta_F = -129.1 \text{ ppm}$



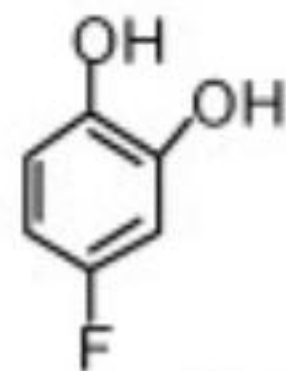
Polymerization
process



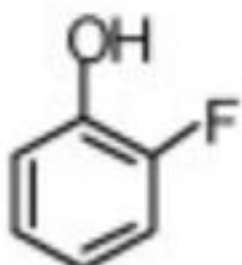
Tyr

$\delta_F = -116.5 \text{ ppm}$

Ascorbic acid

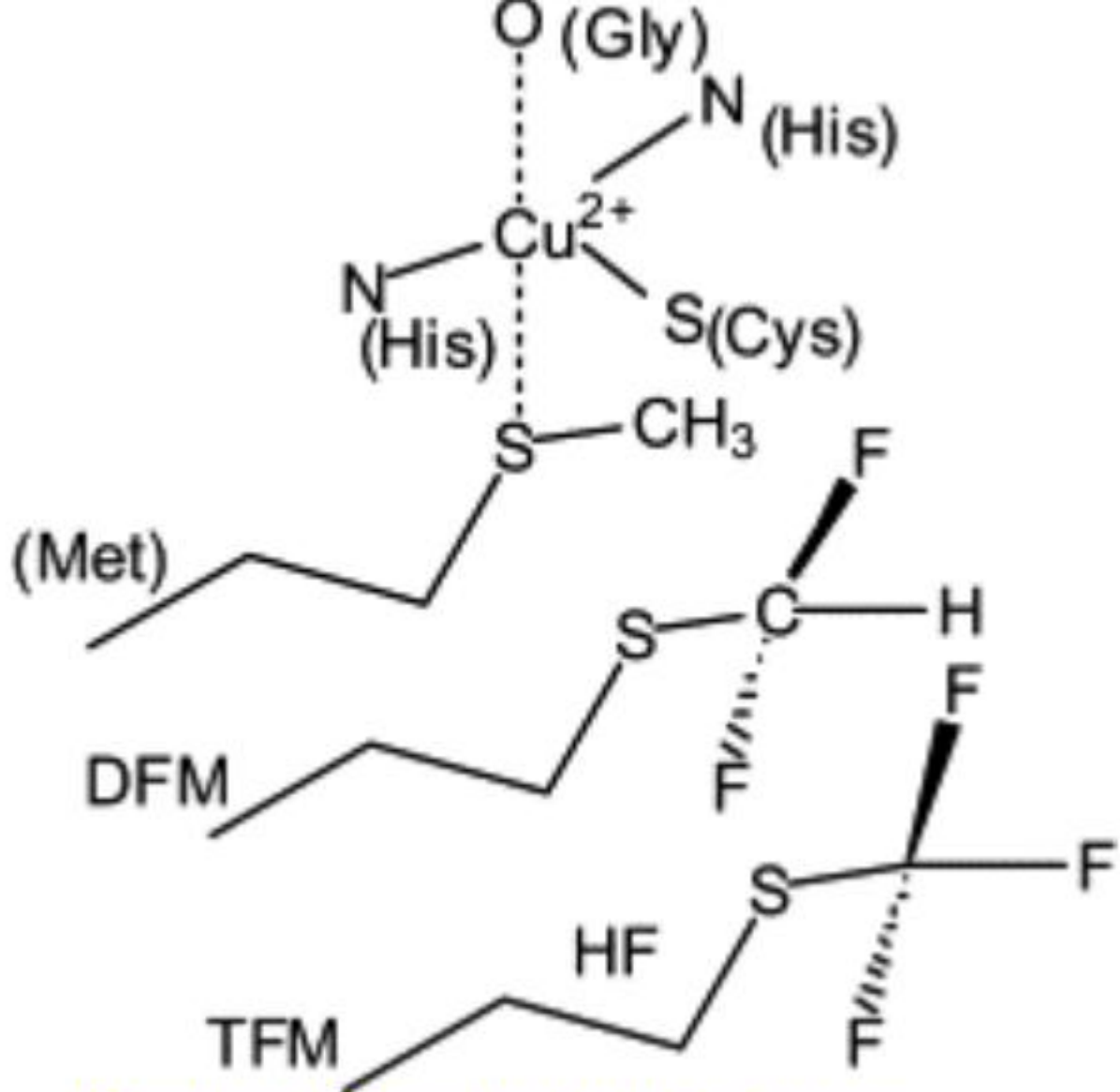


$\delta_F = -126.7 \text{ ppm}$

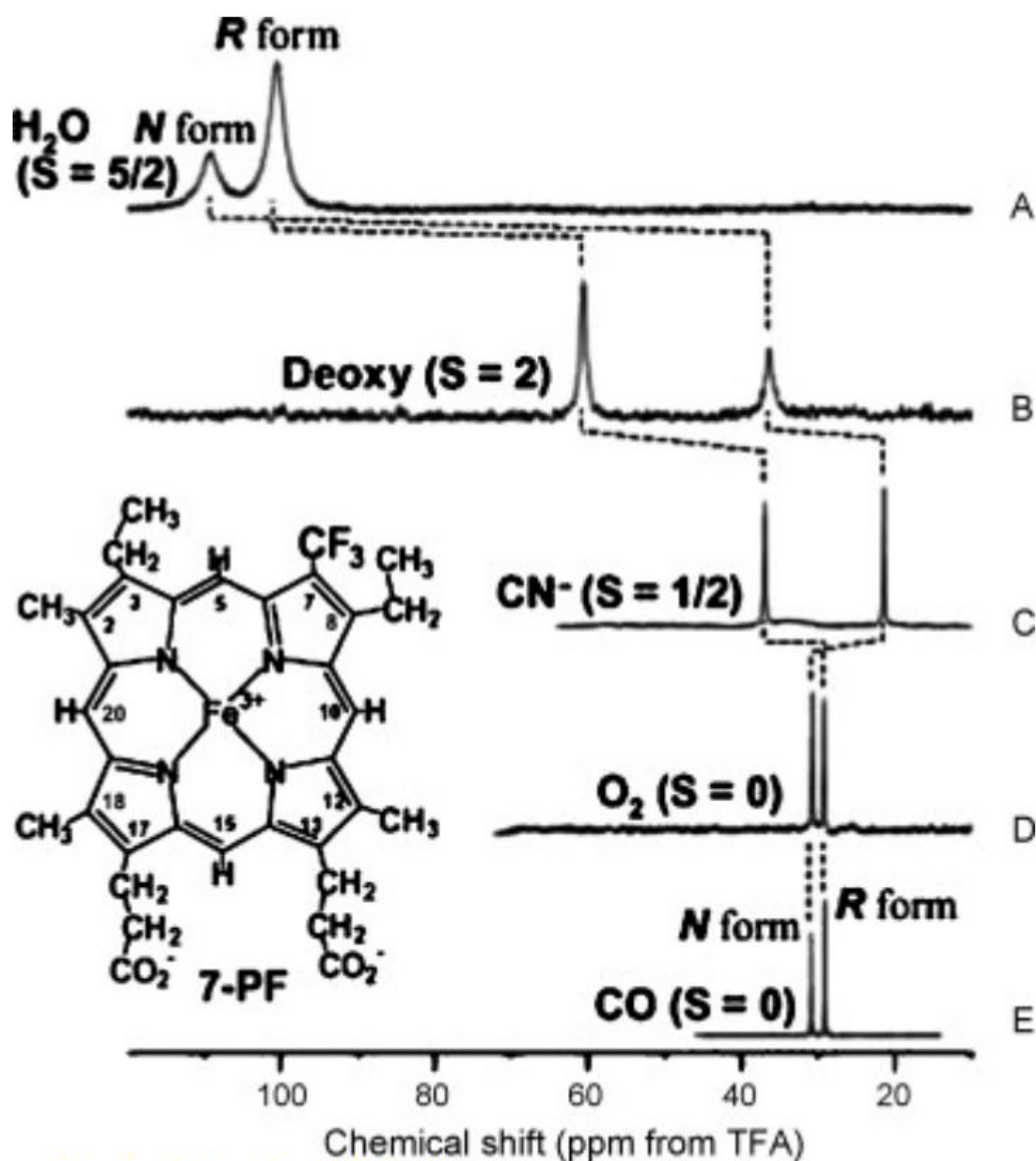


Tyr



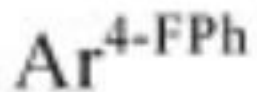
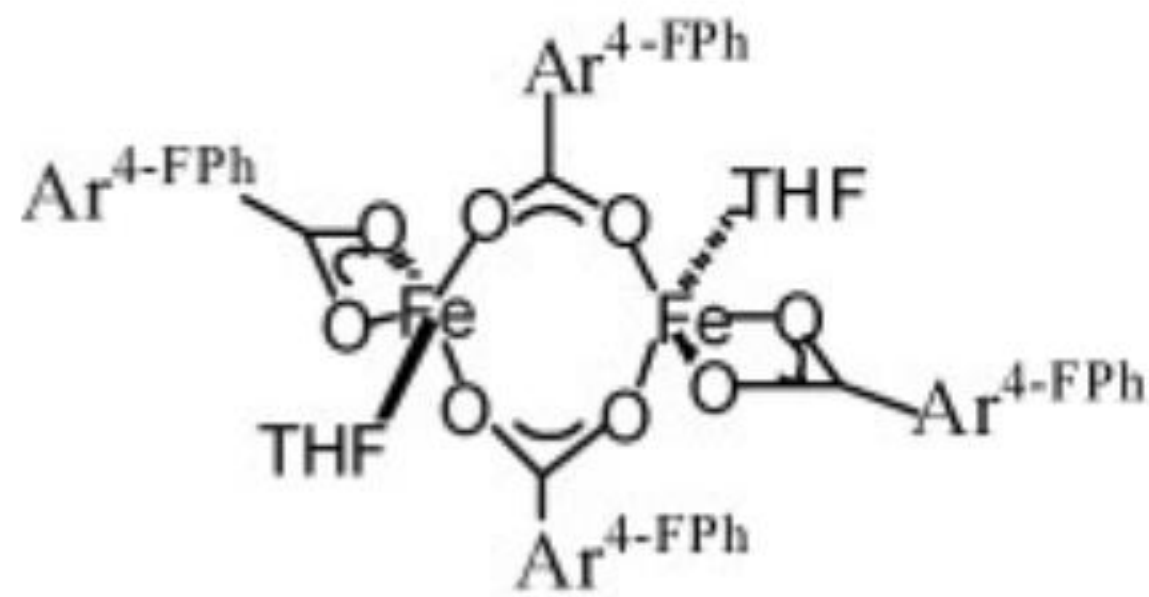
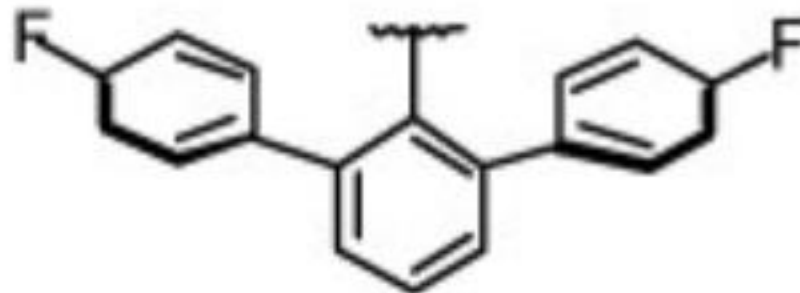


1. [Download: Download full-size image](#)

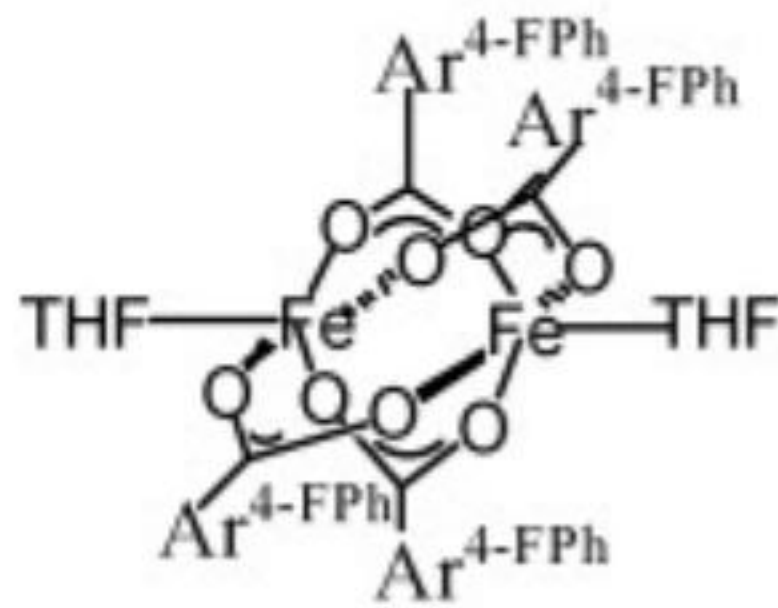




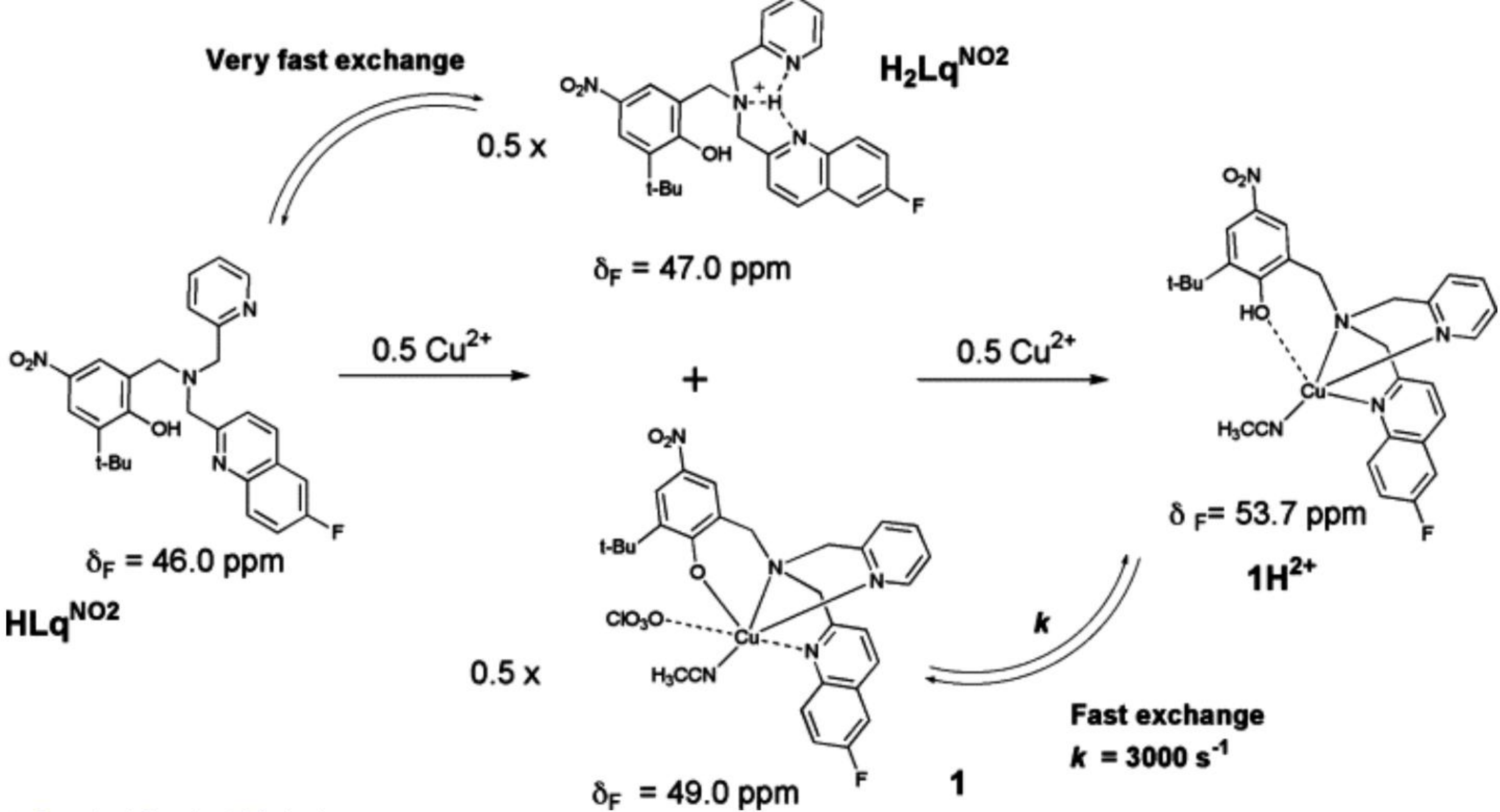
ELSEVIER

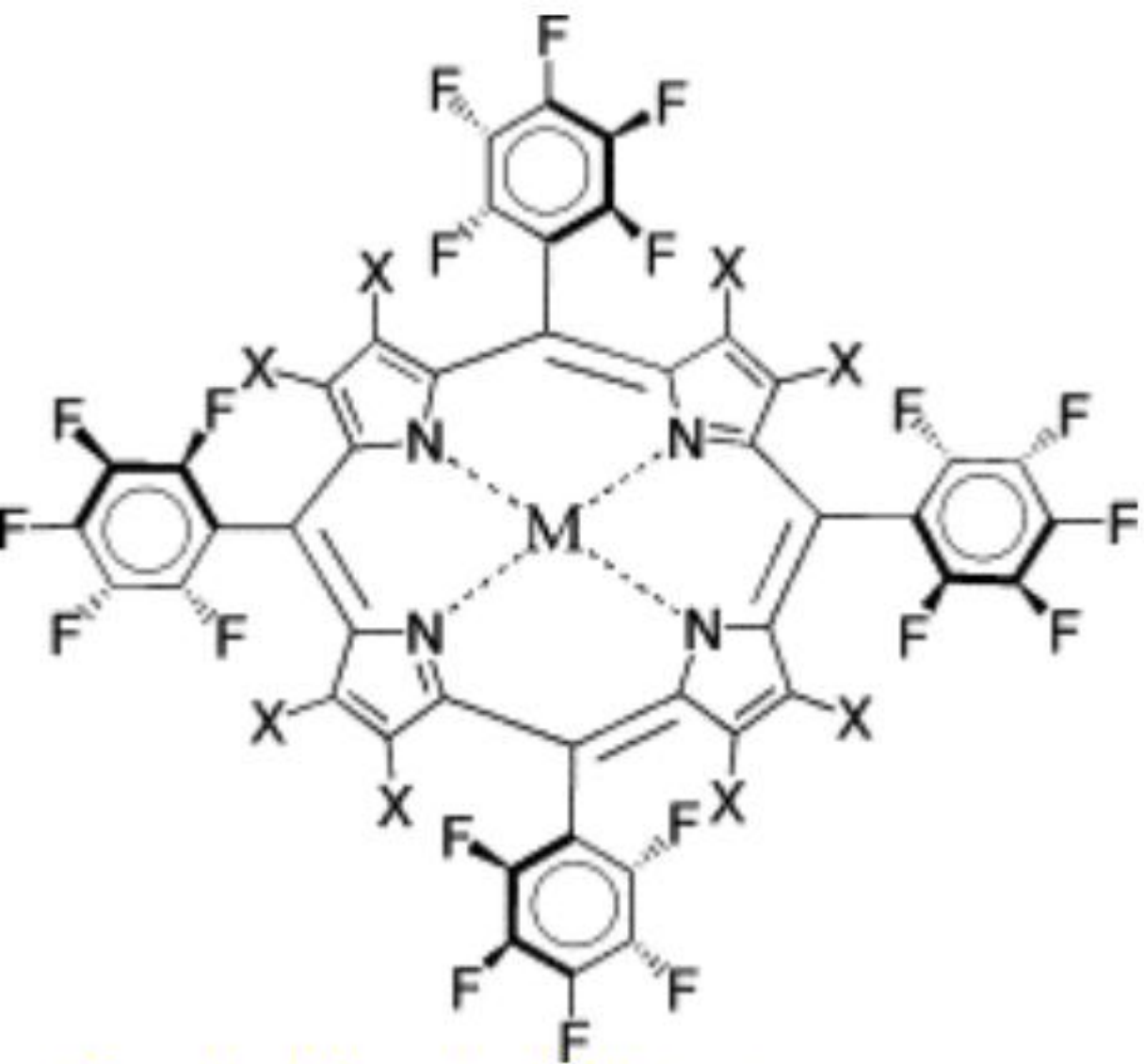
 \equiv 

I



II





(a)

40.0

33.3

29.8

(b)

31.9

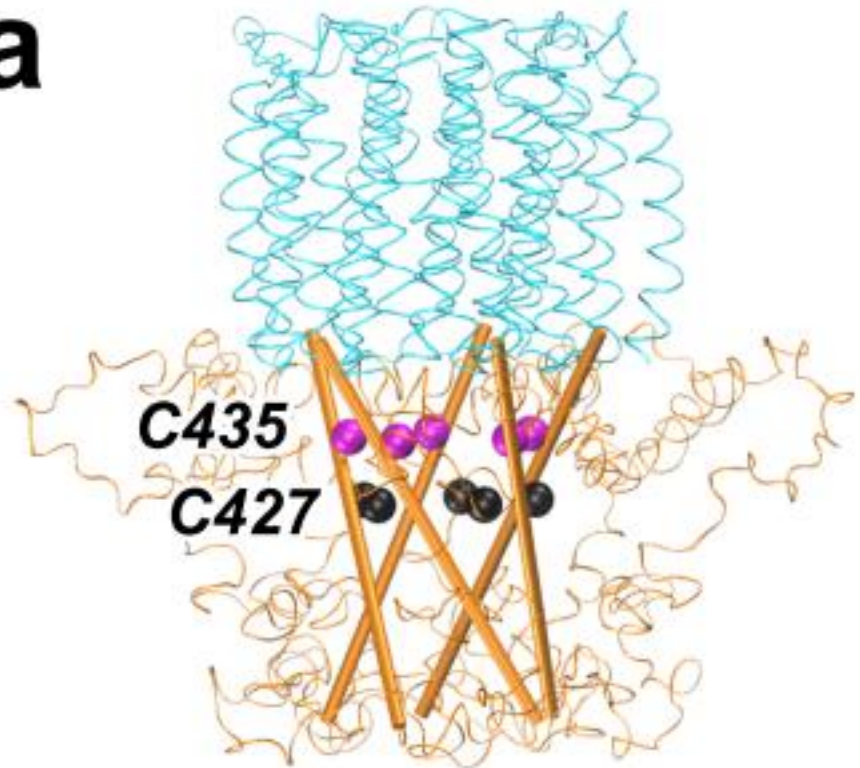
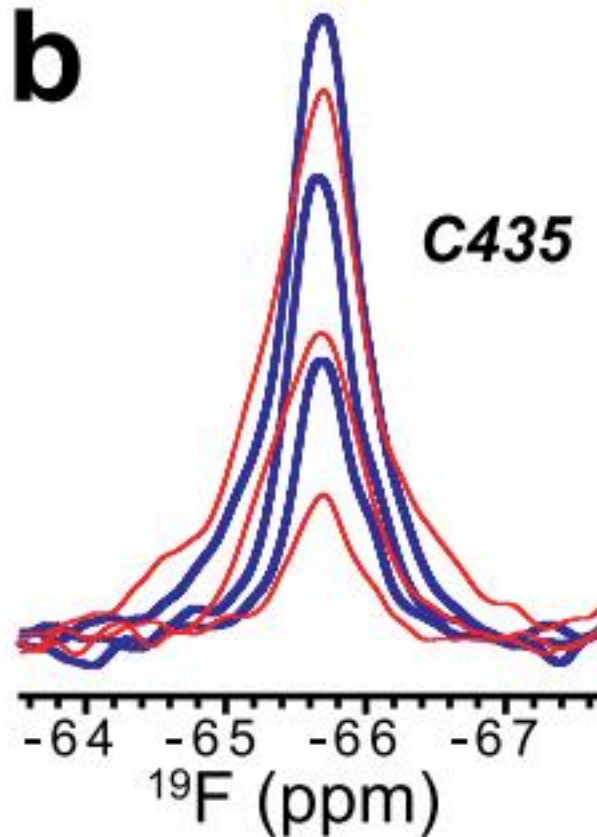
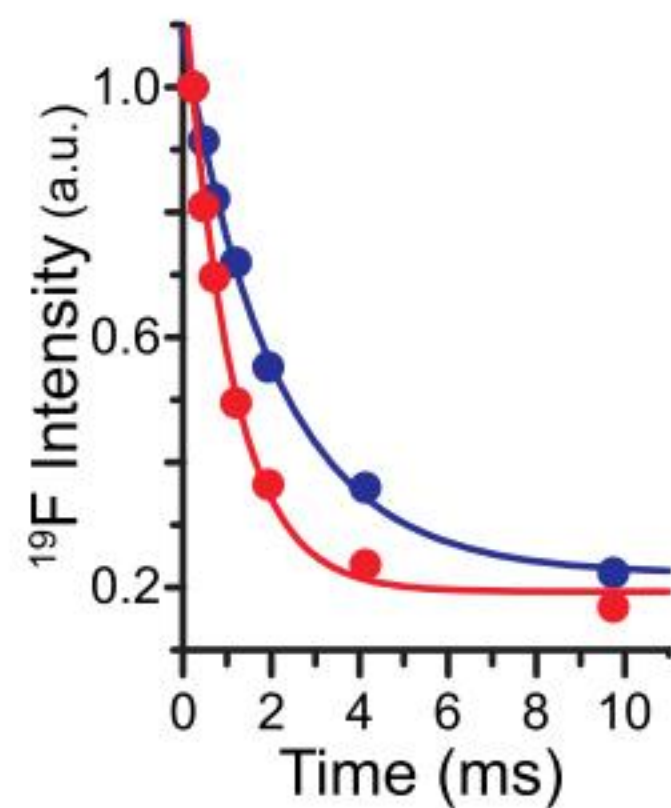
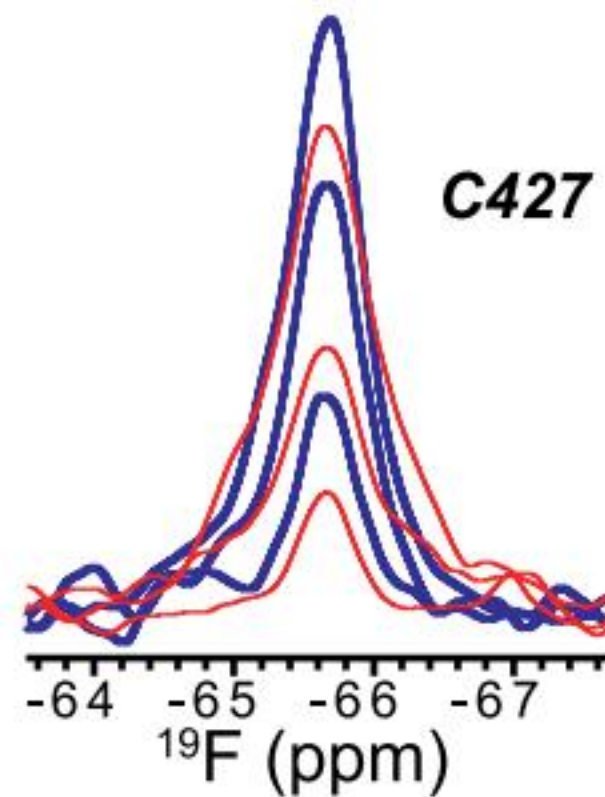
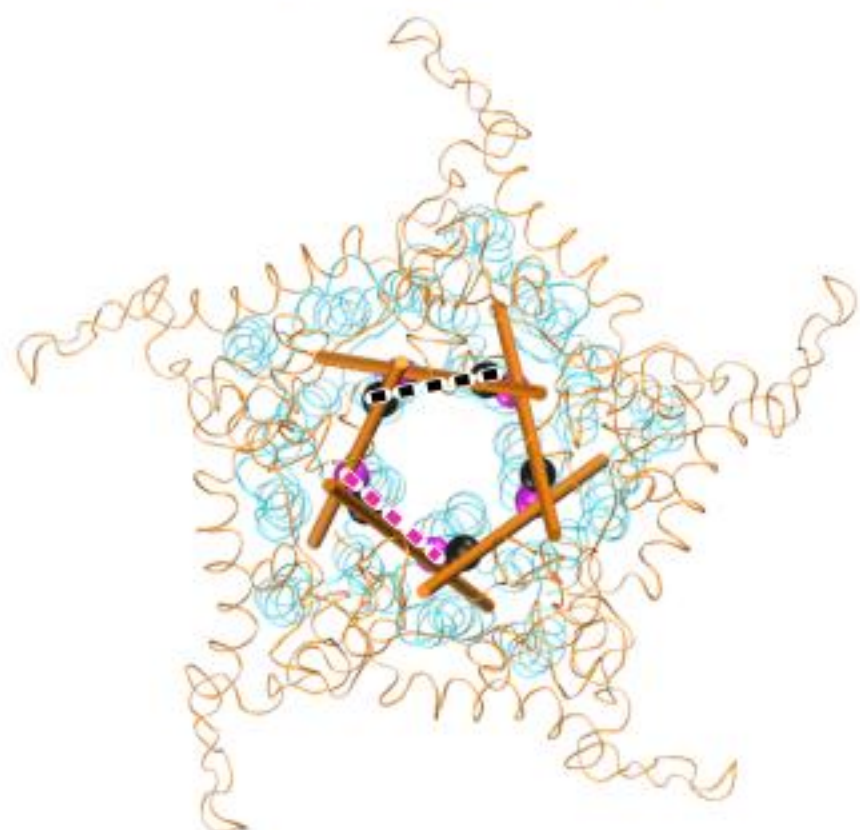
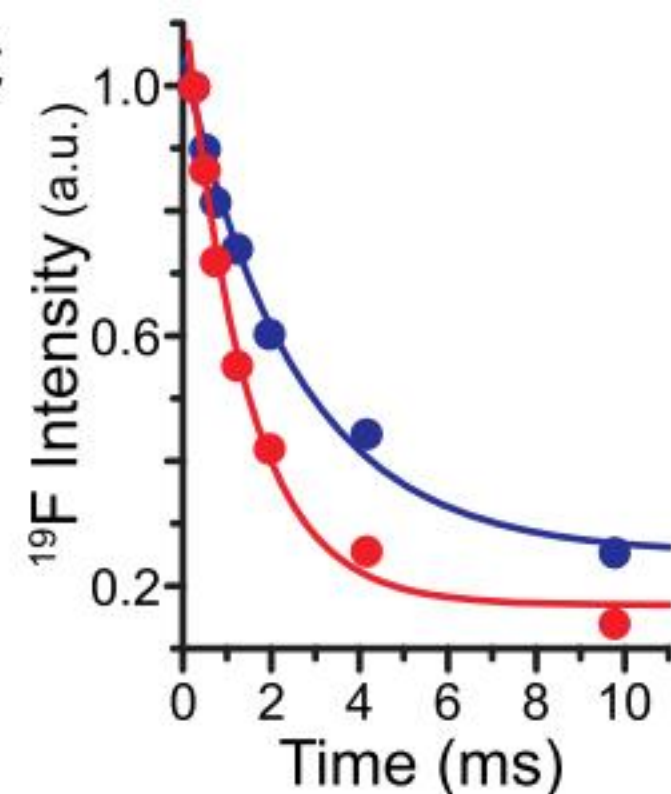
29.7

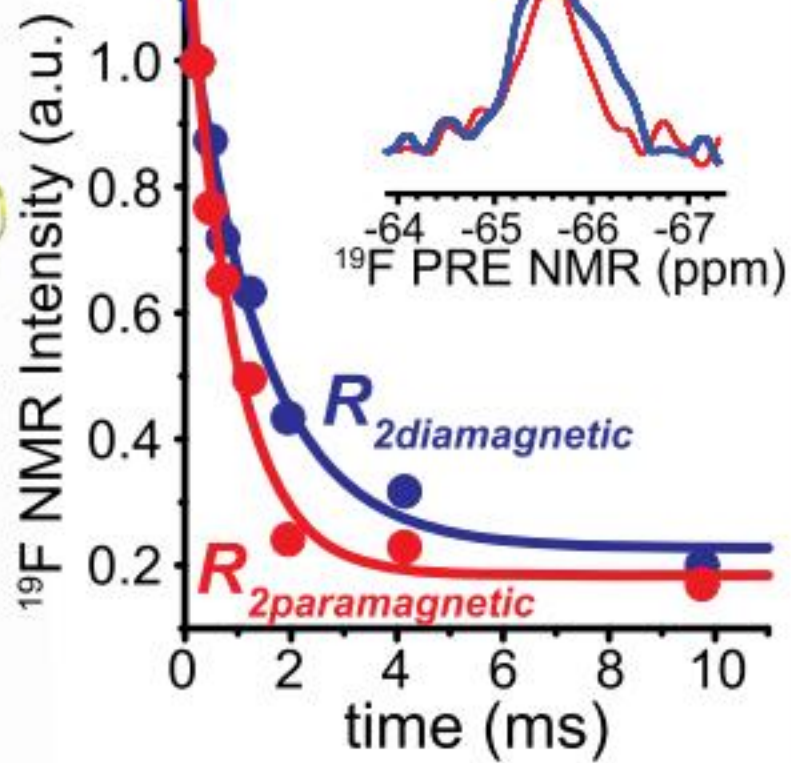
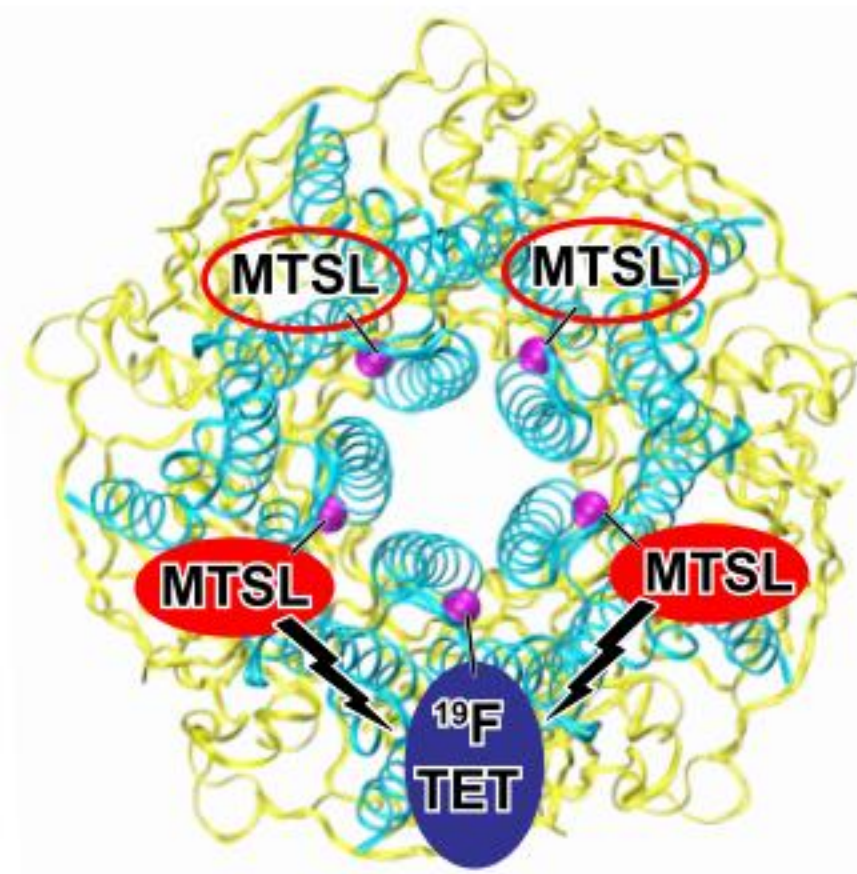
(c)

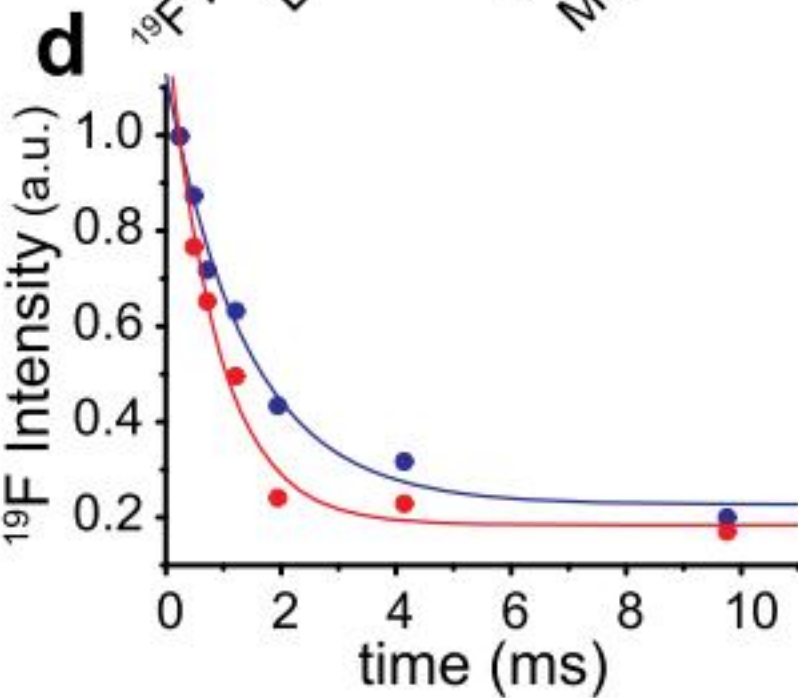
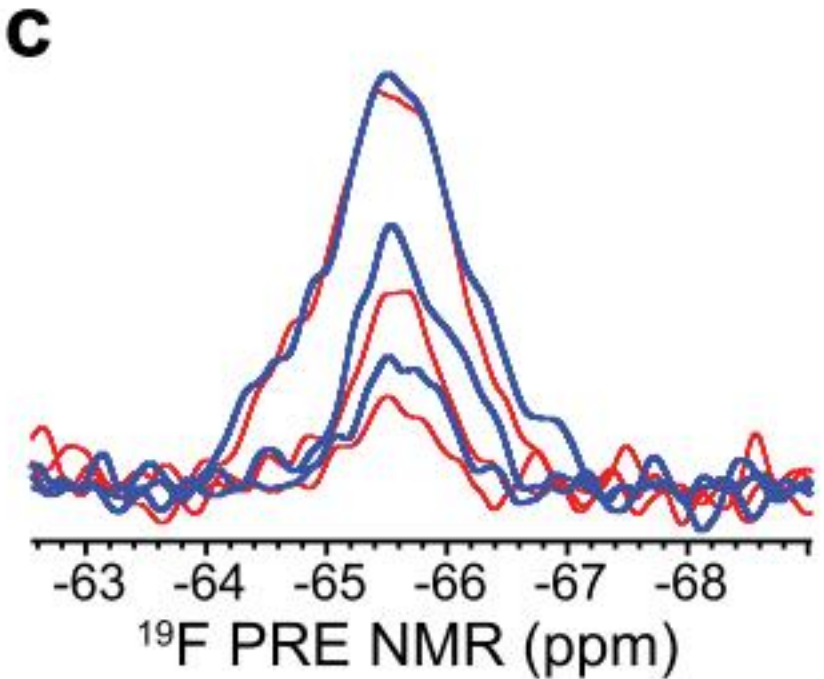
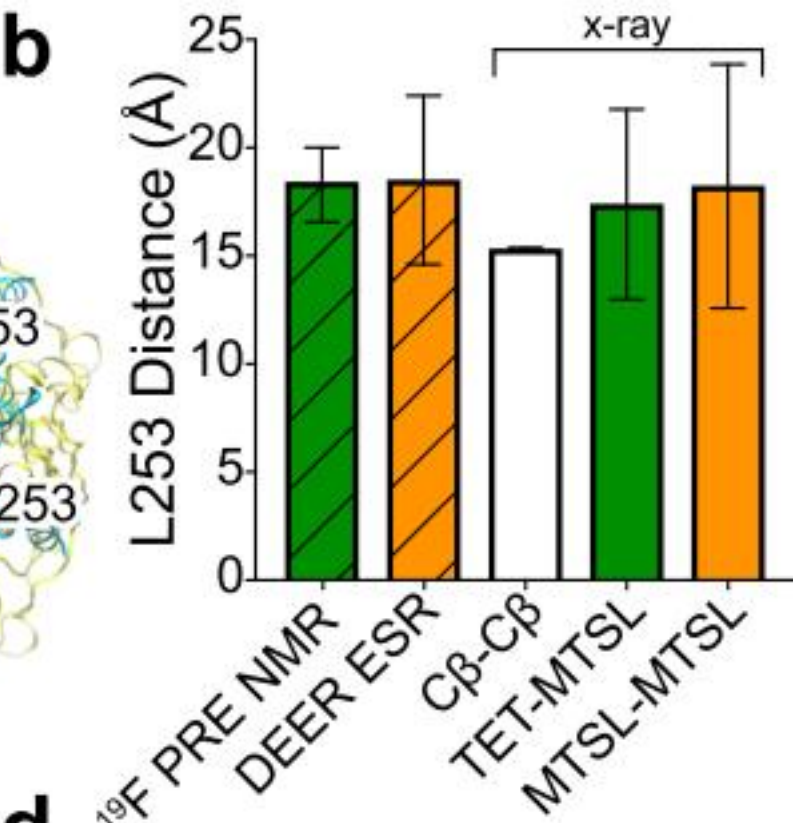
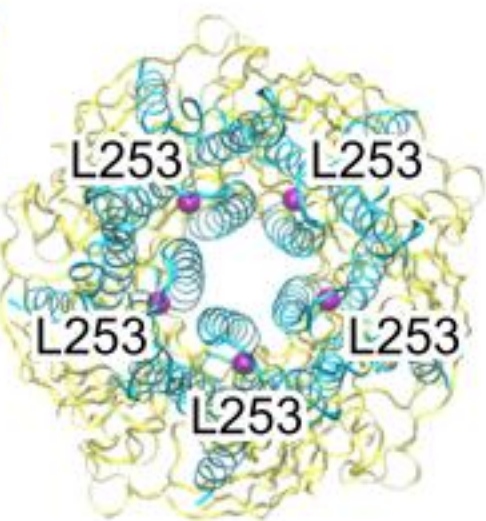
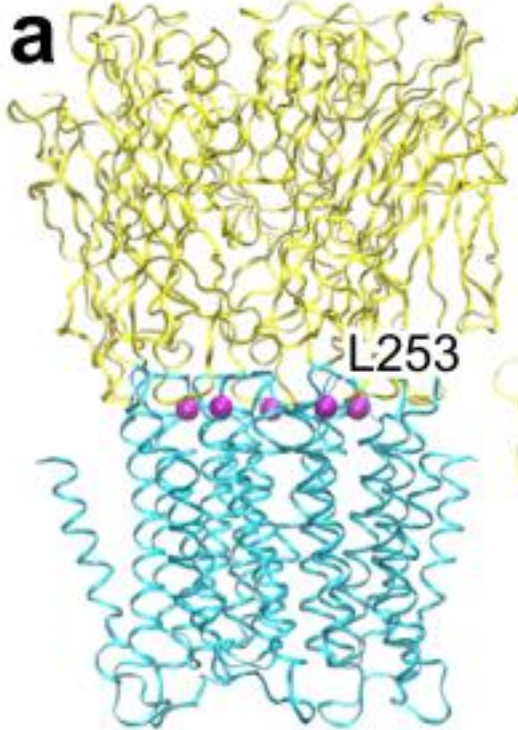
31.9



ACS
chemical
biology

a**b****c**

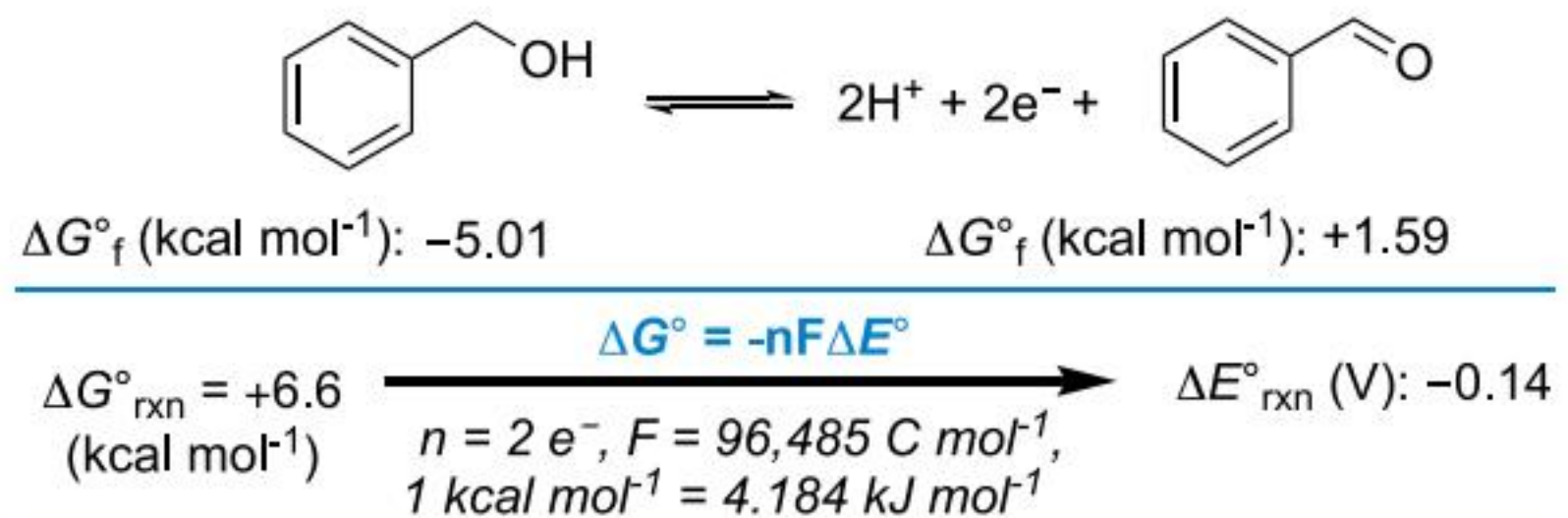








(A) From Free Energy to Potential



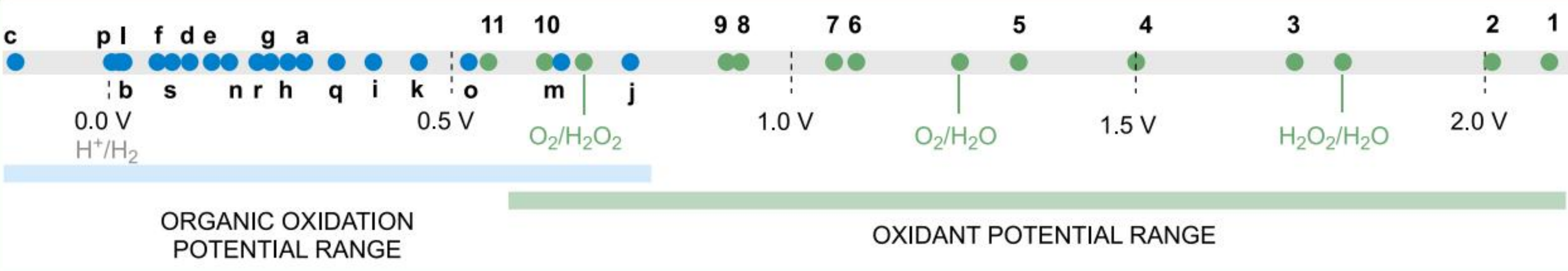
(C) Synthetically Relevant Oxidants ΔE° (V vs SHE)

	SHE:	$2 \text{ H}^+ + 2 \text{ e}^- \rightleftharpoons \text{H}_2$	0.00
1.	$\text{O}_2 + 4 \text{ H}^+ + 4 \text{ e}^- \rightleftharpoons 2 \text{ H}_2\text{O}$	1.23	
2.	$\text{O}_2 + 2 \text{ H}^+ + 2 \text{ e}^- \rightleftharpoons \text{H}_2\text{O}_2$	0.68	
3.	$\text{H}_2\text{O}_2 + 2 \text{ H}^+ + 2 \text{ e}^- \rightleftharpoons 2 \text{ H}_2\text{O}$	1.78	
4.	$\text{O}_3 + 2 \text{ H}^+ + 2 \text{ e}^- \rightleftharpoons \text{O}_2 + \text{H}_2\text{O}$	2.08	
5.	$\text{S}_2\text{O}_8^{2-} + 2 \text{ e}^- \rightleftharpoons 2 \text{ SO}_4^{2-}$	2.01	
6.	$\text{TBHP} + 2 \text{ e}^- + 2 \text{ H}^+ \rightleftharpoons {^t}\text{BuOH} + \text{H}_2\text{O}$	~1.7	
7.	$\text{MnO}_4^- + 8 \text{ H}^+ + 5 \text{ e}^- \rightleftharpoons \text{Mn}^{2+} + 4 \text{ H}_2\text{O}$	1.51	
8.	$\text{Cr}_2\text{O}_7^{2-} + 14 \text{ H}^+ + 6 \text{ e}^- \rightleftharpoons 2 \text{ Cr}^{3+} + 7 \text{ H}_2\text{O}$	1.36	
9.	$\text{Br}_{2(\text{aq})} + 2 \text{ e}^- \rightleftharpoons 2 \text{ Br}^-_{(\text{aq})}$	1.09	
10.	$\text{NO}_2 + 2 \text{ H}^+ + 2 \text{ e}^- \rightleftharpoons \text{NO} + \text{H}_2\text{O}$	1.05	
11.	$\text{TEMPO}^+ + 2 \text{ e}^- + 2 \text{ H}^+ \rightleftharpoons \text{TEMPOH}_2^+$	0.91 ^a	
12.	$\text{DDQ} + 2 \text{ e}^- + 2 \text{ H}^+ \rightleftharpoons \text{DDH}_2\text{Q}$	0.89 ^a	
13.	$\text{BQ} + 2 \text{ H}^+ + 2 \text{ e}^- \rightleftharpoons \text{H}_2\text{Q}$	0.64 ^a	
14.	$\text{I}_{2(\text{aq})} + 2 \text{ e}^- \rightleftharpoons 2 \text{ I}^-_{(\text{aq})}$	0.54	

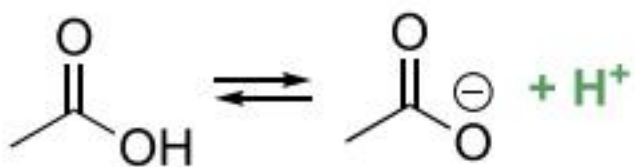
(B) Organic Reaction Redox Potentials $-\Delta E^\circ$ (V vs SHE)

Alcohol Oxidation		
a.	$\text{EtOH} \rightleftharpoons \text{acetaldehyde} + 2 \text{ H}^+ + 2 \text{ e}^-$	0.28
b.	$\text{EtOH} + \text{H}_2\text{O} \rightleftharpoons \text{acetic acid} + 4 \text{ H}^+ + 4 \text{ e}^-$	0.06
c.	$\text{acetaldehyde} + \text{H}_2\text{O} \rightleftharpoons \text{acetic acid} + 2 \text{ H}^+ + 2 \text{ e}^-$	-0.16
d.	$\text{iPrOH} \rightleftharpoons \text{acetone} + 2 \text{ H}^+ + 2 \text{ e}^-$	0.12
e.	$\text{BnOH} \rightleftharpoons \text{PhCHO} + 2 \text{ H}^+ + 2 \text{ e}^-$	0.14
Alkene Oxidation		
f.	$\text{propene} + \text{H}_2\text{O} \rightleftharpoons \text{acetone} + 2 \text{ H}^+ + 2 \text{ e}^-$	0.09
g.	$\text{propene} + \text{H}_2\text{O} \rightleftharpoons \text{propanal} + 2 \text{ H}^+ + 2 \text{ e}^-$	0.23
h.	$\text{ethylene} + \text{H}_2\text{O} \rightleftharpoons \text{acetaldehyde} + 2 \text{ H}^+ + 2 \text{ e}^-$	0.26
i.	$\text{ethylene} + 2 \text{ H}_2\text{O} \rightleftharpoons \text{ethylene glycol} + 2 \text{ H}^+ + 2 \text{ e}^-$	0.40
j.	$\text{propene} + \text{H}_2\text{O} \rightleftharpoons \text{propylene oxide} + 2 \text{ H}^+ + 2 \text{ e}^-$	0.76
<i>sp</i> ³ C–H Oxidation		
k.	$\text{propane} \rightleftharpoons \text{propene} + 2 \text{ H}^+ + 2 \text{ e}^-$	0.45
l.	$\text{pyrrolidine} + \text{H}_2\text{O} \rightleftharpoons \gamma\text{-lactam} + 4 \text{ H}^+ + 4 \text{ e}^-$	0.02
m.	$\text{CH}_4 + \text{H}_2\text{O} \rightleftharpoons \text{methanol} + 2 \text{ H}^+ + 2 \text{ e}^-$	0.63
n.	$\text{CH}_4 + 2 \text{ H}_2\text{O} \rightleftharpoons \text{CO}_2 + 8 \text{ H}^+ + 8 \text{ e}^-$	0.17
o.	$\text{toluene} + \text{H}_2\text{O} \rightleftharpoons \text{BnOH} + 2 \text{ H}^+ + 2 \text{ e}^-$	0.53
Arene C–H Oxidation		
p.	$2 \text{ benzene} \rightleftharpoons \text{biphenyl} + 2 \text{ H}^+ + 2 \text{ e}^-$	0.01
q.	$\text{benzene} + \text{H}_2\text{O} \rightleftharpoons \text{phenol} + 2 \text{ H}^+ + 2 \text{ e}^-$	0.32
r.	$\text{benzene} + \text{NH}_3 \rightleftharpoons \text{aniline} + 2 \text{ H}^+ + 2 \text{ e}^-$	0.21
s.	$\text{benzene} + \text{acetamide} \rightleftharpoons \text{acetanilide} + 2 \text{ H}^+ + 2 \text{ e}^-$	0.10

(D) Potentials for Organic Oxidations and Oxidants



Free Energy, pH, pK_a , Redox Potentials, and Equilibria

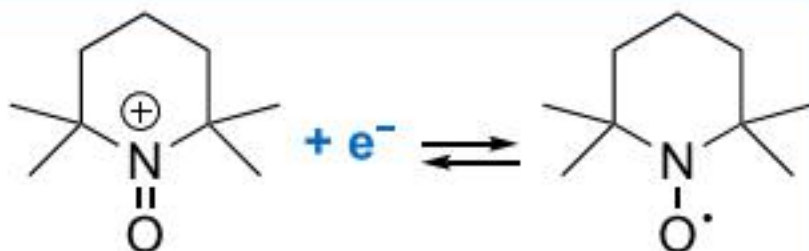
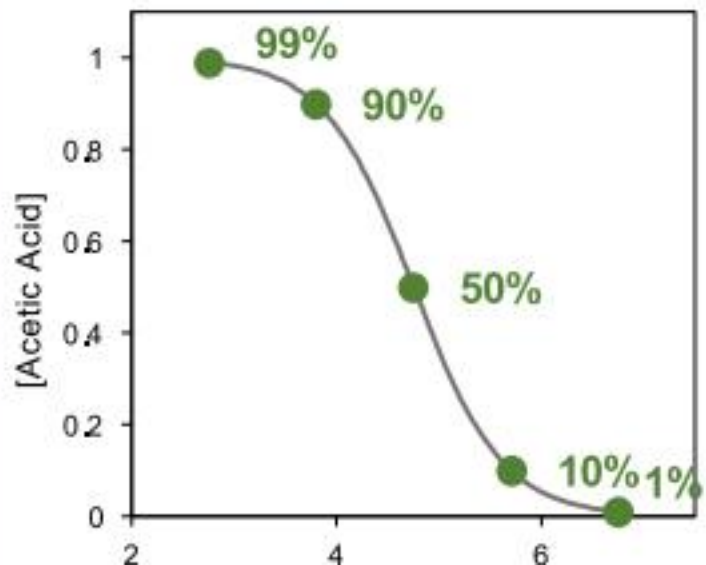


$$\text{pH} = \text{p}K_a + \log_{10}([\text{A}^-]/[\text{HA}])$$

For $[\text{AcO}^-]/[\text{AcOH}] = 10$

$$\Delta G = \Delta G^\circ + 2.3 \text{ RT} \log_{10}(10)$$

$$\Delta G = \Delta G^\circ + 1.36 \text{ kcal mol}^{-1}$$

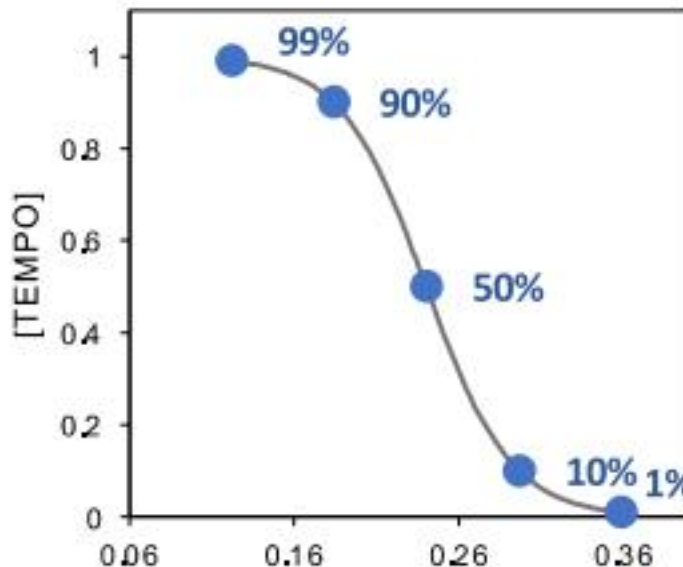


$$\Delta E = \Delta E^\circ - (\text{RT}/\text{nF}) \ln([\text{T}]/[\text{T}^+])$$

for $[\text{T}]/[\text{T}^+] = 10$

$$\Delta E = \Delta E^\circ - (2.3 \text{ RT}/\text{nF}) \log_{10}(10)$$

$$\Delta E = \Delta E^\circ - 59 \text{ mV/n}$$







Read online

needed to initiate single-electron transfer (SET), but these values are very different from the thermodynamic potentials for net two-electron redox reactions of interest to organic chemists.



ACCESS |



Metrics & More



Article Recommendations



Supporting Information

ABSTRACT: Redox reactions are ubiquitous in organic synthesis and



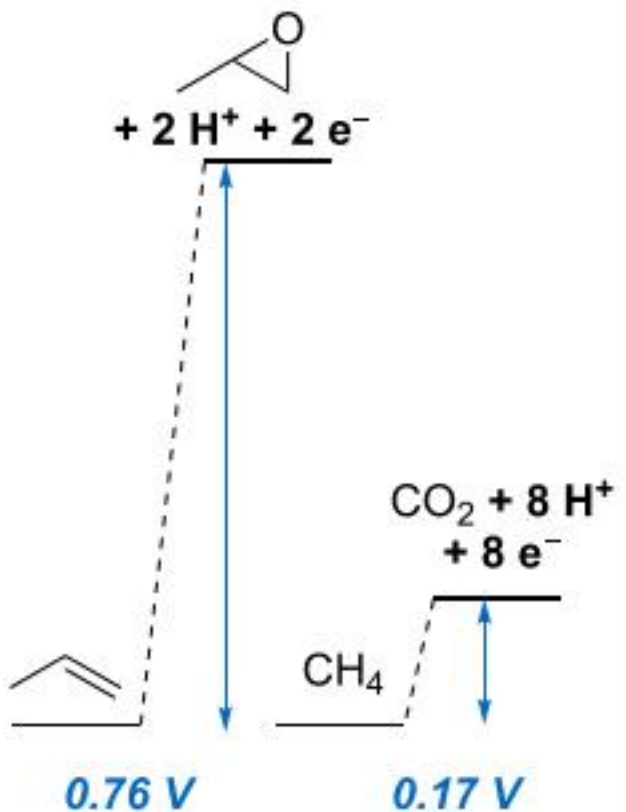
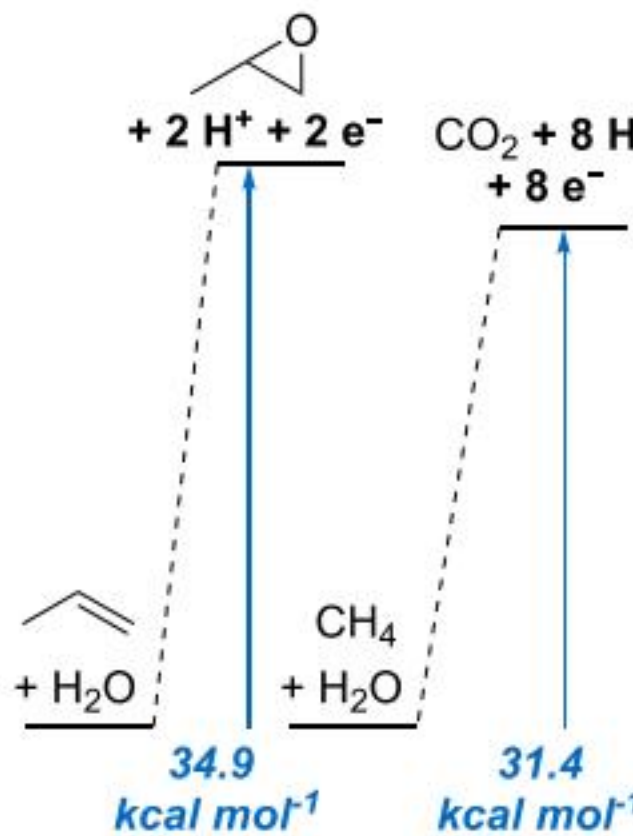
joc

The Journal of Open Chemistry

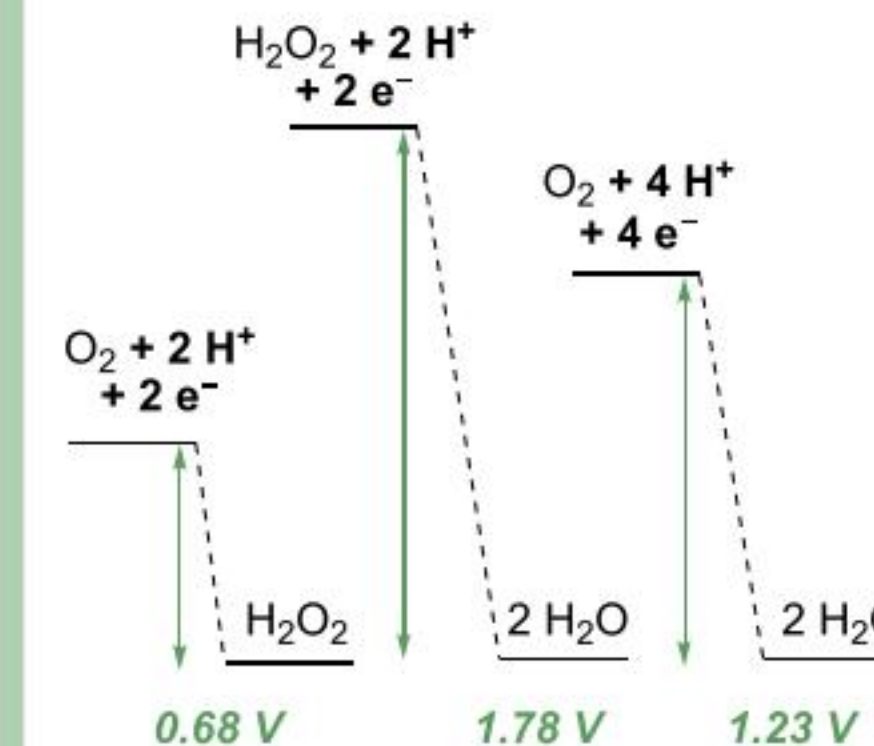
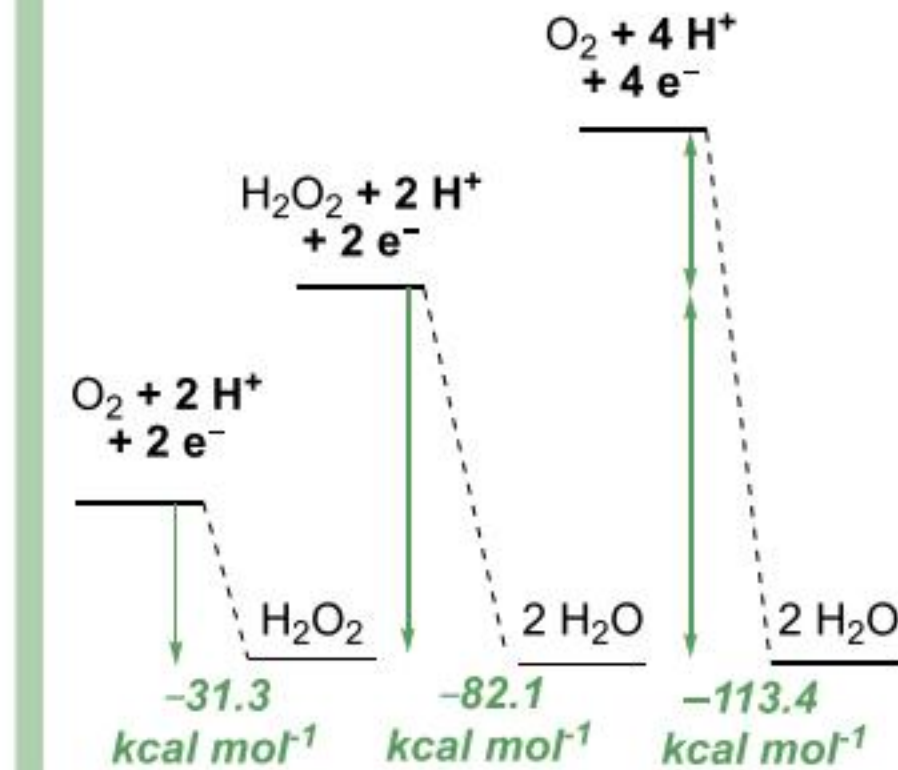


(A) Propylene Epoxidation vs. Methane Oxidation

	ΔG° (kcal mol ⁻¹)	$-\Delta E^\circ$ (V vs. SHE)
$\text{CH}_2 = \text{CH}_2 + \text{H}_2\text{O} \rightleftharpoons \text{CH}_2 = \text{CH}-\text{O}-\text{CH}_3 + 2 \text{H}^+ + 2 \text{e}^-$	34.9	0.76
$\text{CH}_4 + 2 \text{H}_2\text{O} \rightleftharpoons \text{CO}_2 + 8 \text{H}^+ + 8 \text{e}^-$	31.4	0.17

Standard Potential ΔE° Free Energy ΔG° **(B) O₂ and H₂O₂ Reduction**

	ΔG° (kcal mol ⁻¹)	$-\Delta E^\circ$ (V vs. SHE)
$\text{O}_2 + 2 \text{H}^+ + 2 \text{e}^- \rightleftharpoons \text{H}_2\text{O}_2$	-31.3	0.68
$\text{H}_2\text{O}_2 + 2 \text{H}^+ + 2 \text{e}^- \rightleftharpoons 2 \text{H}_2\text{O}$	-82.1	1.78
$\text{O}_2 + 4 \text{H}^+ + 4 \text{e}^- \rightleftharpoons 2 \text{H}_2\text{O}$	-113.4	1.23

Standard Potential ΔE° Free Energy ΔG° 

(A) Overpotential in Chemical Redox Reactions

Thermochemistry of Some Alcohol Oxidations



$$\Delta E^\circ: 0.0 - 0.14 = -0.14 \text{ V}$$

$$\Delta G^\circ: +6.6 \text{ kcal mol}^{-1}$$

$$K_{\text{eq}}: 1.5 \times 10^{-5}$$



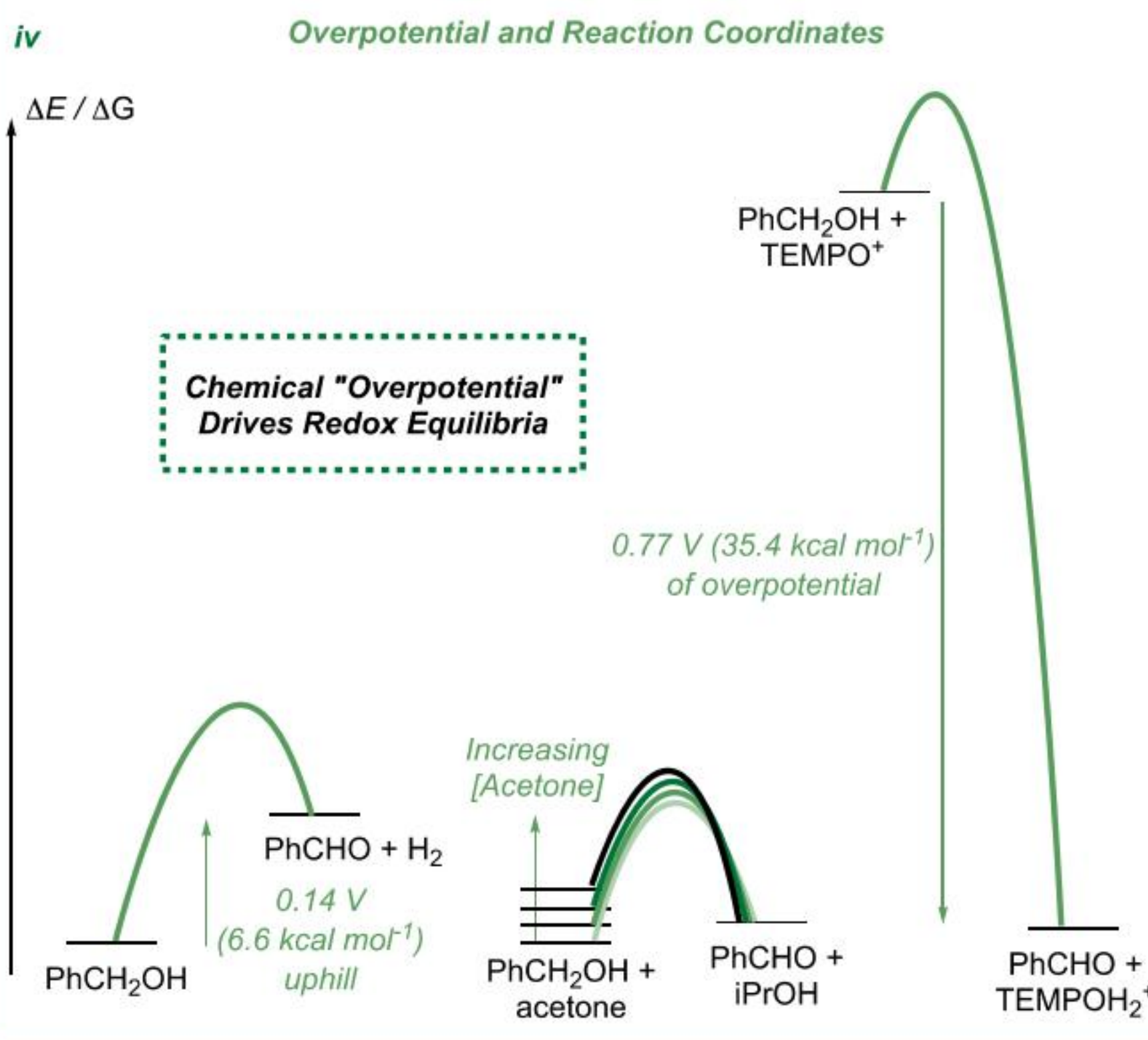
[BnOH] : [Acetone]	$RT/nF^*\ln(Q)$	ΔE (mV)	ΔG (kcal mol ⁻¹)	Yield PhCHO
1:1	0 mV	-25	+1.1	28%
1:2	-9 mV	-16	+0.73	67%
1:10	-30 mV	+5	-0.22	94%
1:100	-59 mV	+34	-1.6	99.3%



$$\Delta E^\circ: 0.91 - 0.14 = 0.77 \text{ V}$$

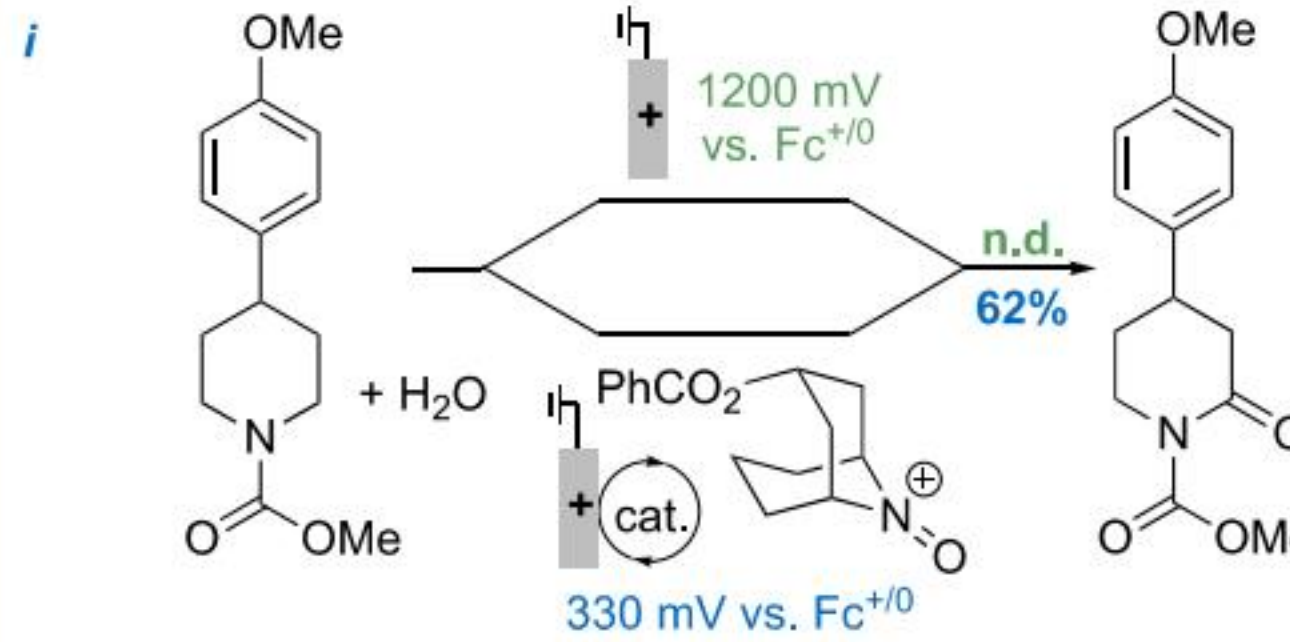
$$\Delta G^\circ: -35.4 \text{ kcal mol}^{-1}$$

$$K_{\text{eq}}: 9.1 \times 10^{25}$$

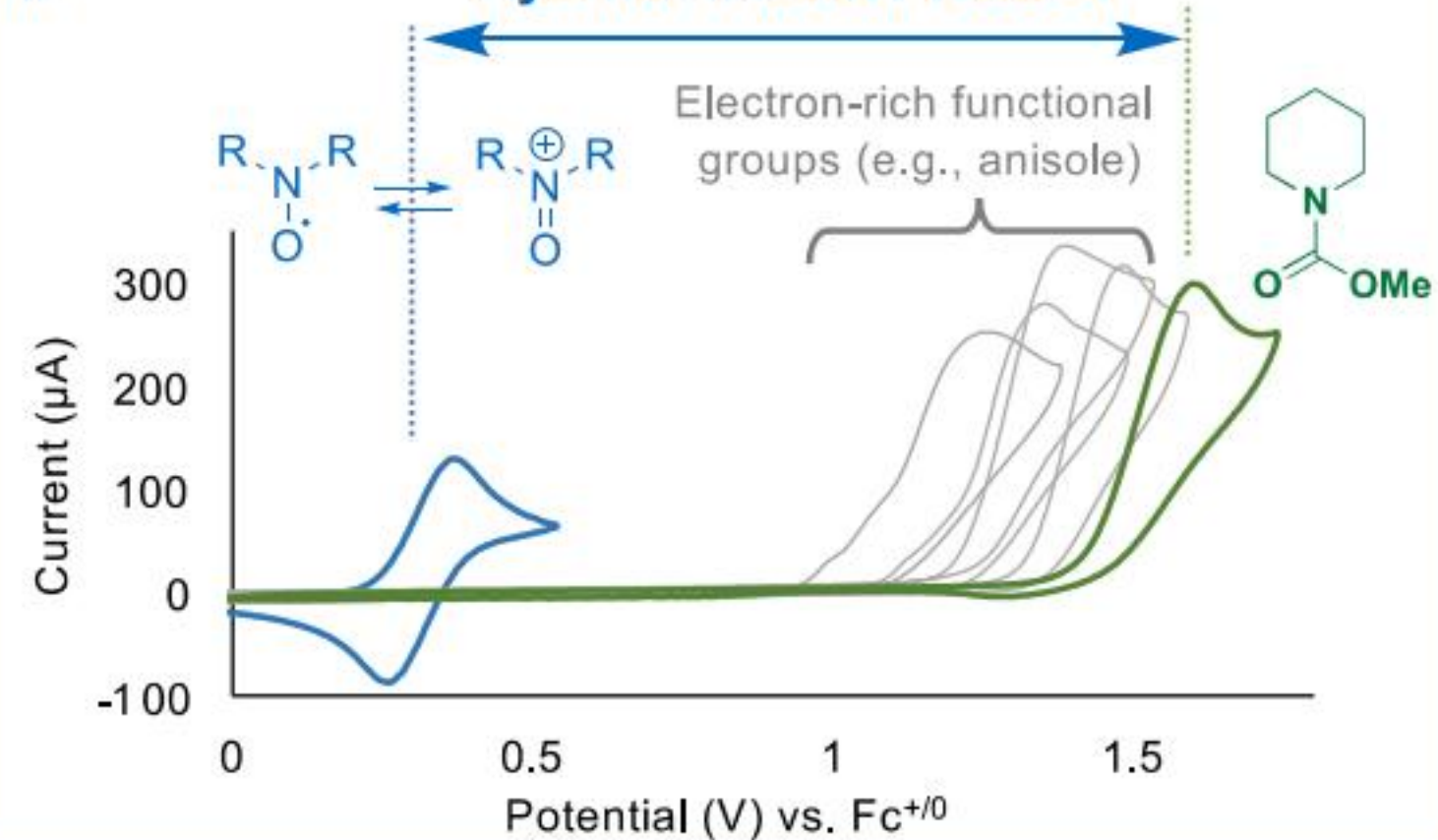


(B) Overpotential in Electrochemical Reactions

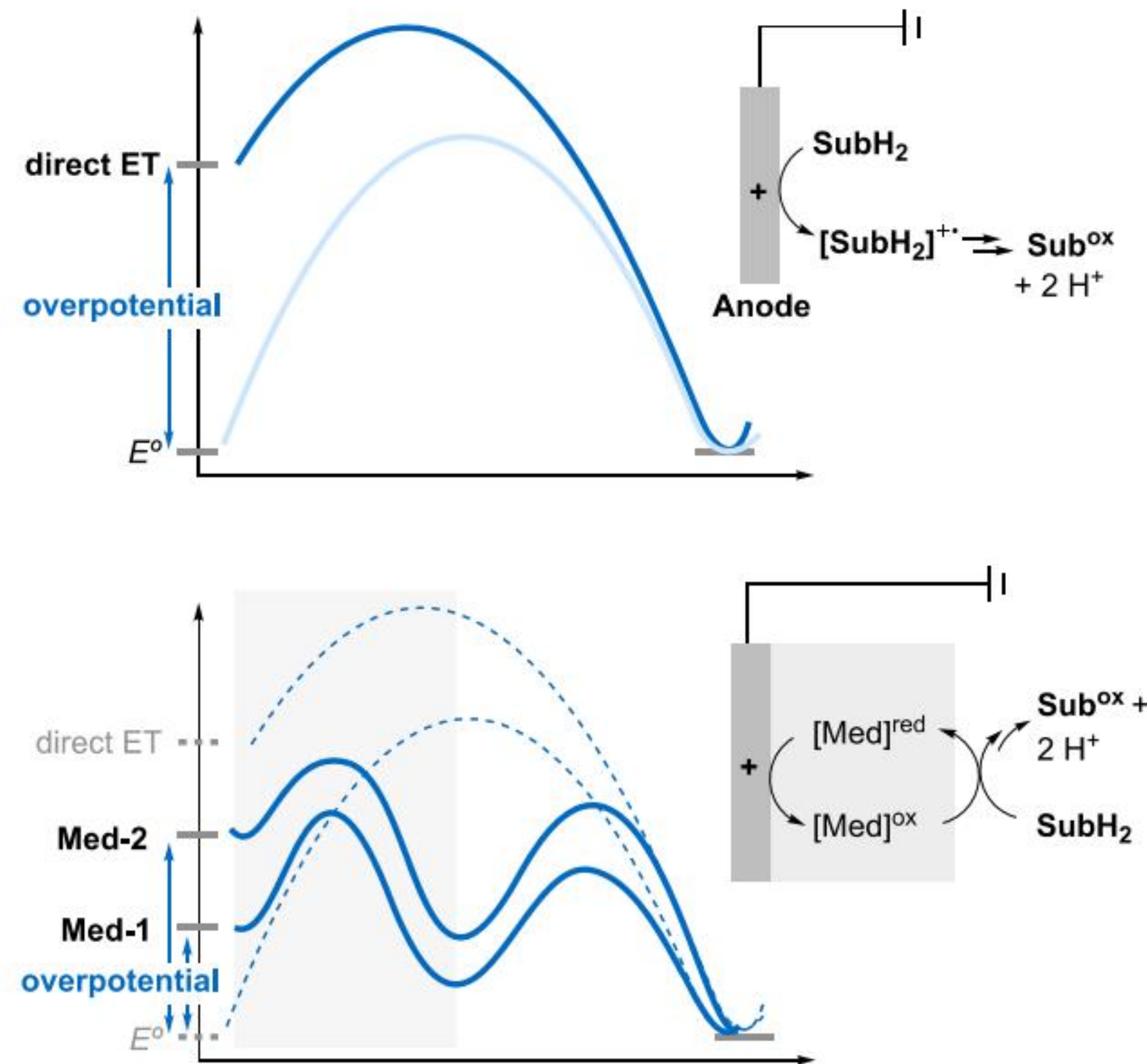
Shono-Type Carbamate Oxidation



Hydride Transfer vs. SET

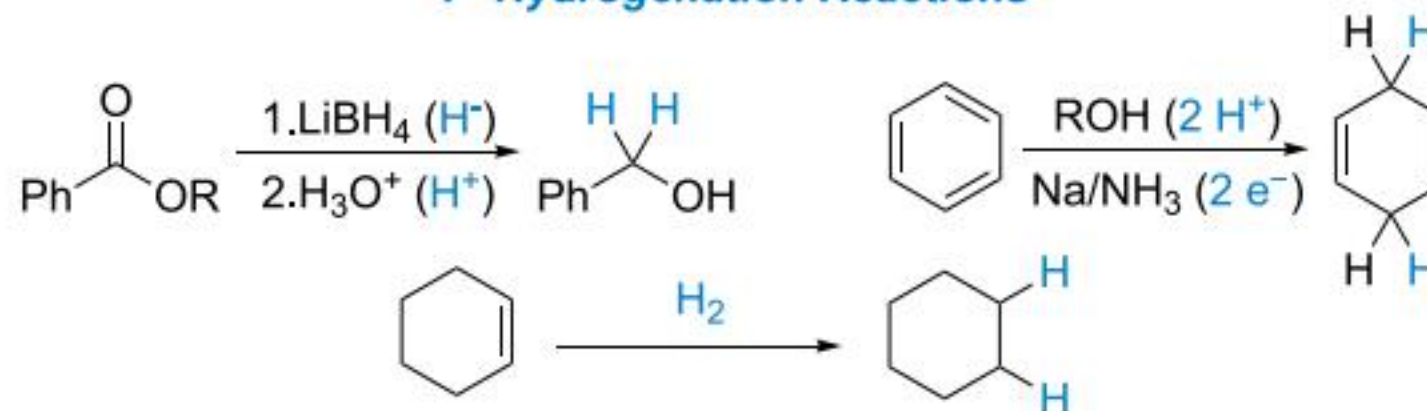


Reaction Coordinates for Electrochemical Redox Reactions

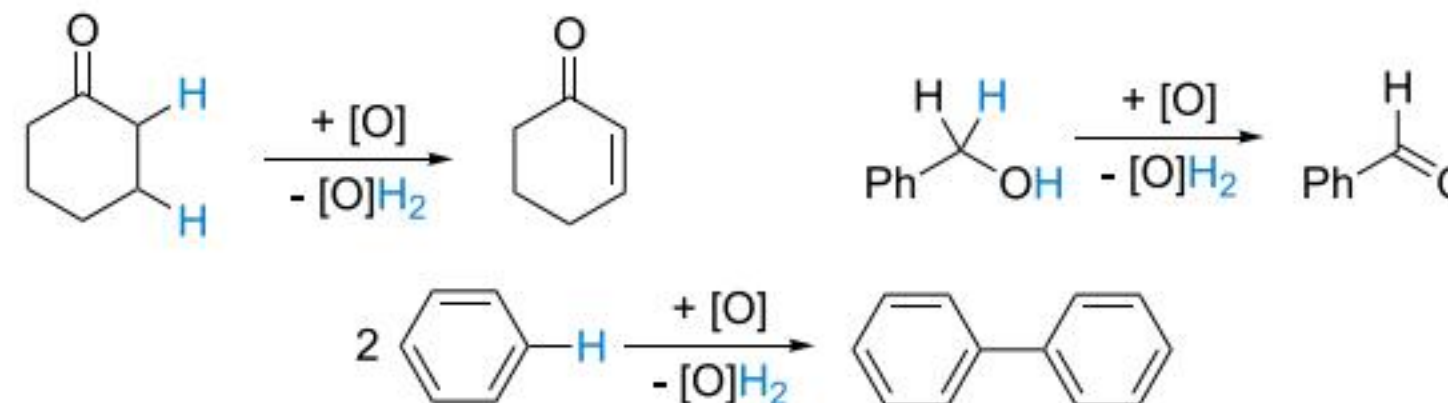


(A) Redox Reactions in Organic Chemistry

i - Hydrogenation Reactions

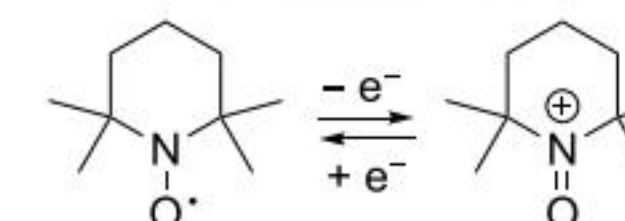


ii - Dehydrogenation Reactions

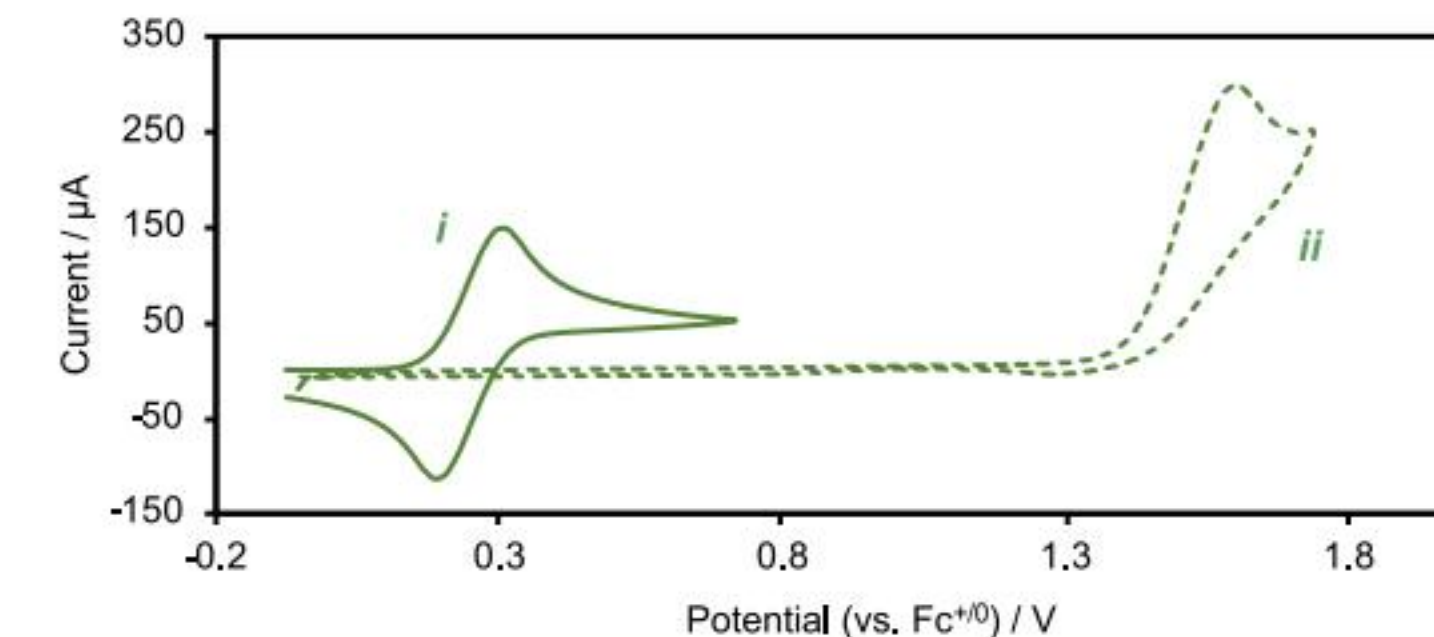
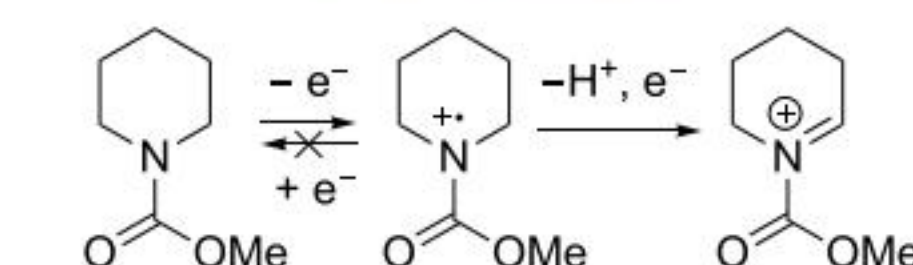


(B) Electron Transfer Reactions and Electrochemical Potentials

i - Reversible ET



ii - Irreversible ET



(C) Potentials Required for ET at an Electrode

Imines

Ketones

Aldehydes

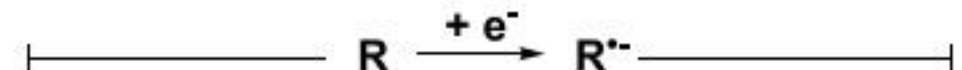
-3.0 V

-2.0 V

-1.0 V

Aryl and Alkyl Halides

Carboxylic Acids,
Esters, Nitriles



Carboxylates

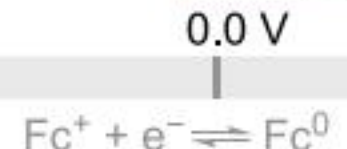
Ethers

Aryl Halides

0.0 V

1.0 V

2.0 V

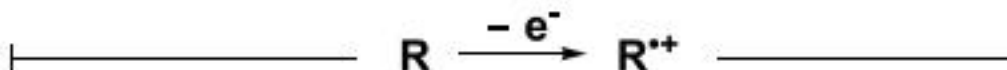


Amines

Alkenes

Phenols

Aromatic Heterocycles



(D) Reference Electrodes

Potential Conversions for Non-aqueous Reference Electrodes

Ag/AgNO₃
(1 mM)

Ag/AgNO₃
(10 mM)

SCE

Fc^{+/-}

87 mV

139 mV

385 mV
in CH₃CN, 25 °C



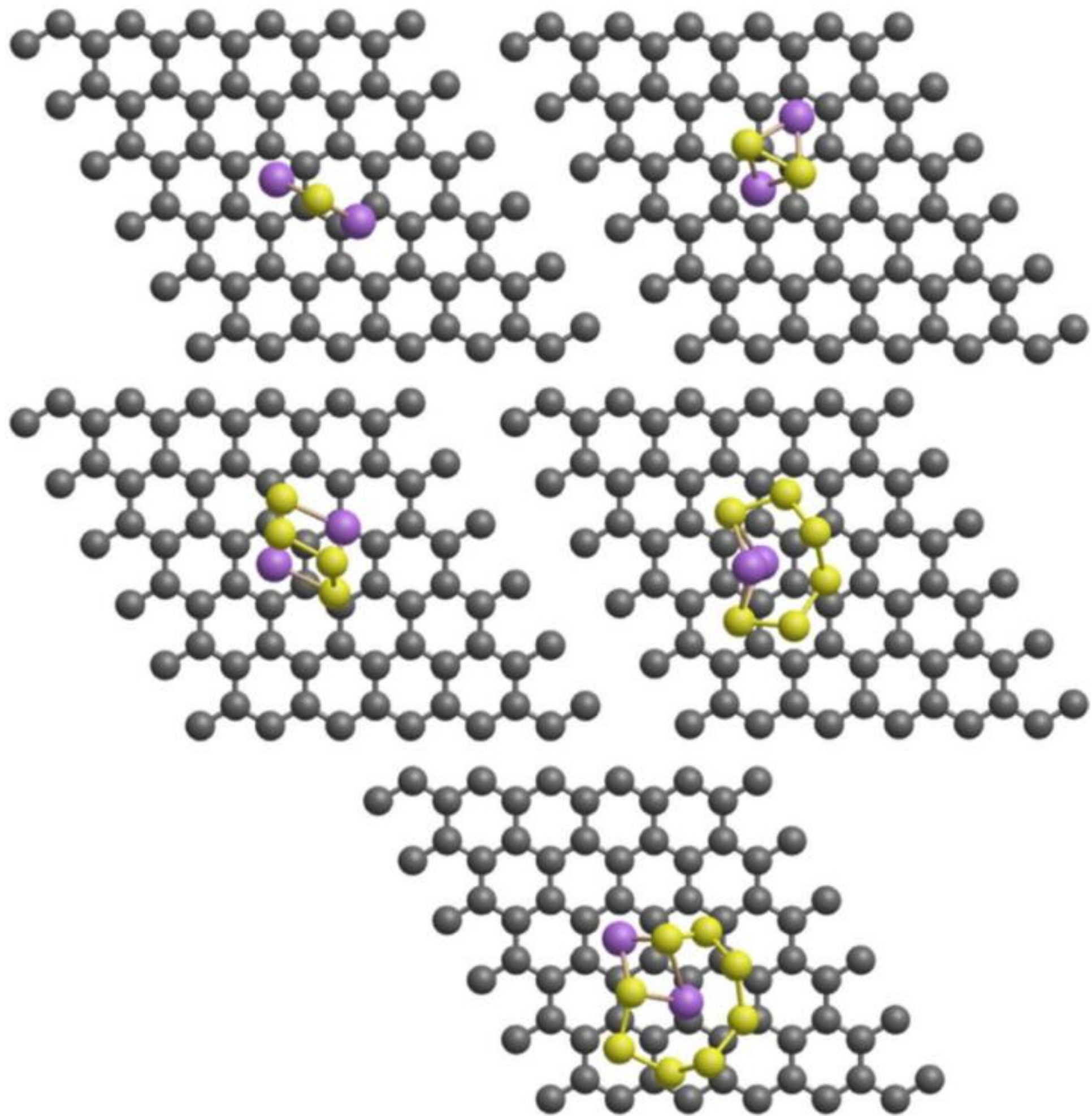


Figure 16. Illustration of atomic configurations for various LiPS species (Li_2S_x , $x = 1, 2, 4, 6, 8$) on a pristine graphene sheet. Grey, yellow and purple spheres represent C, S and Li atoms, respectively.

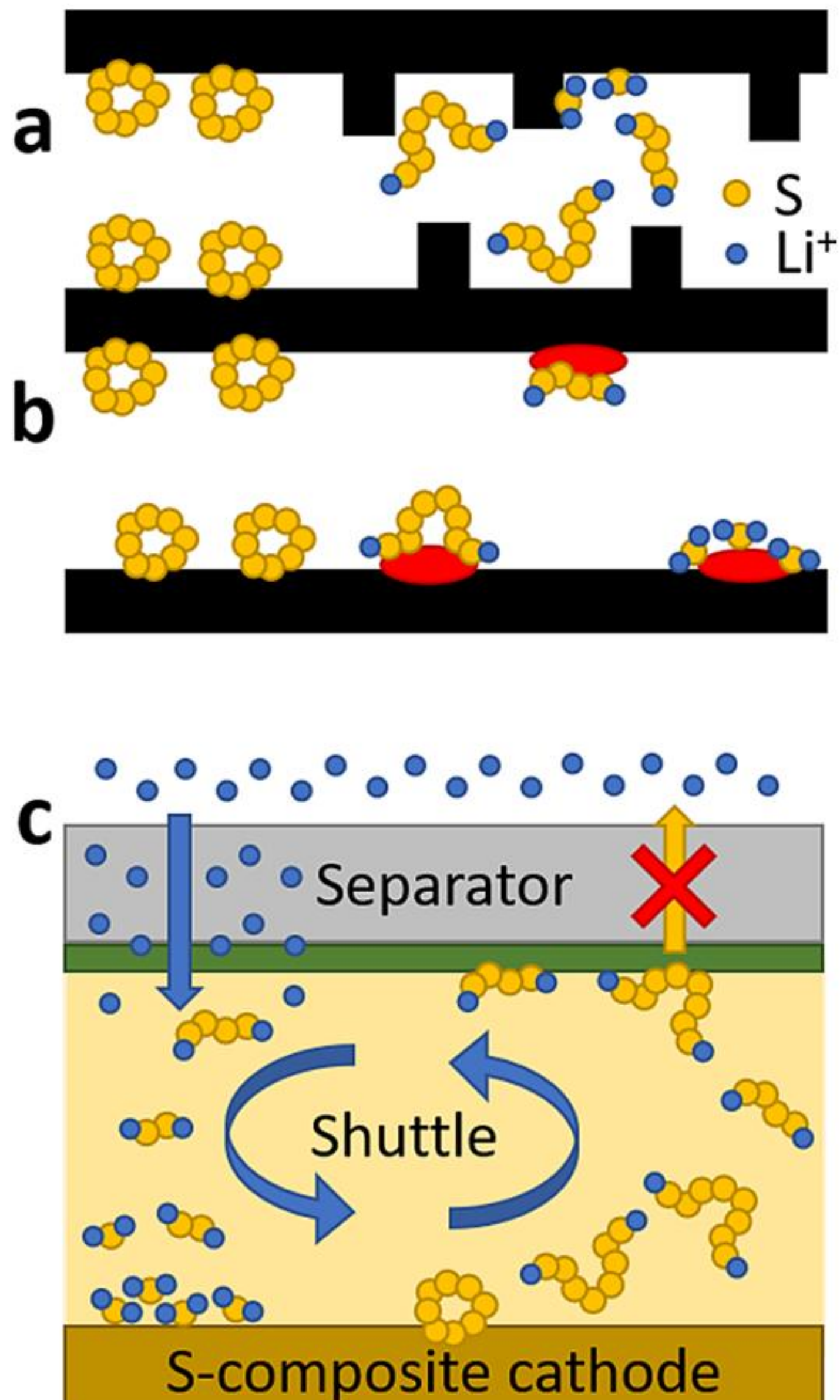
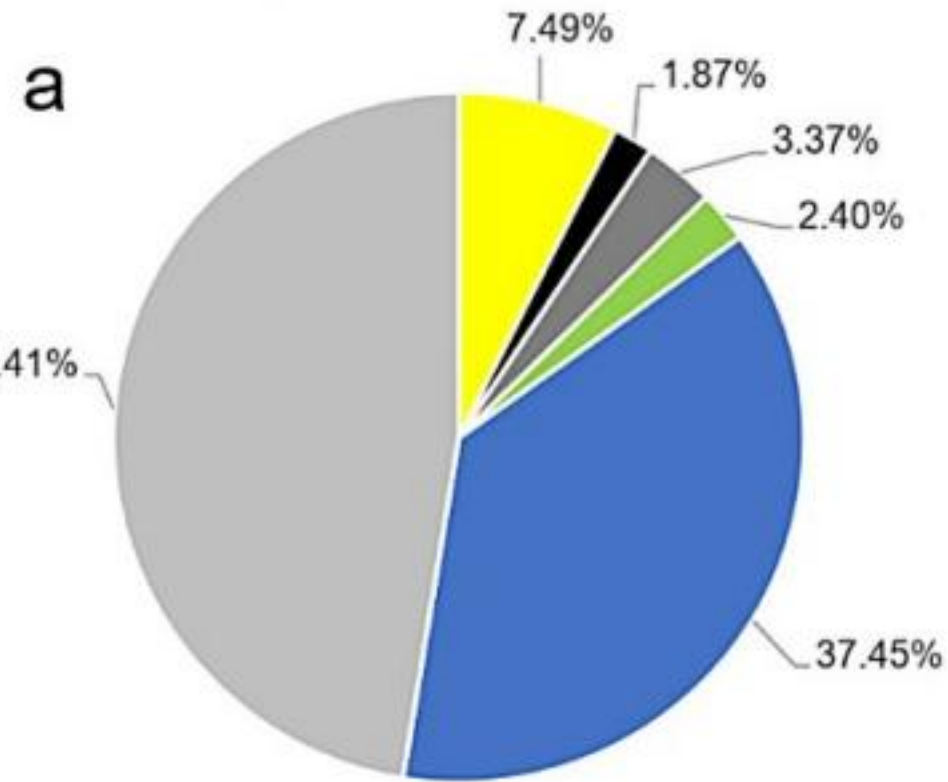
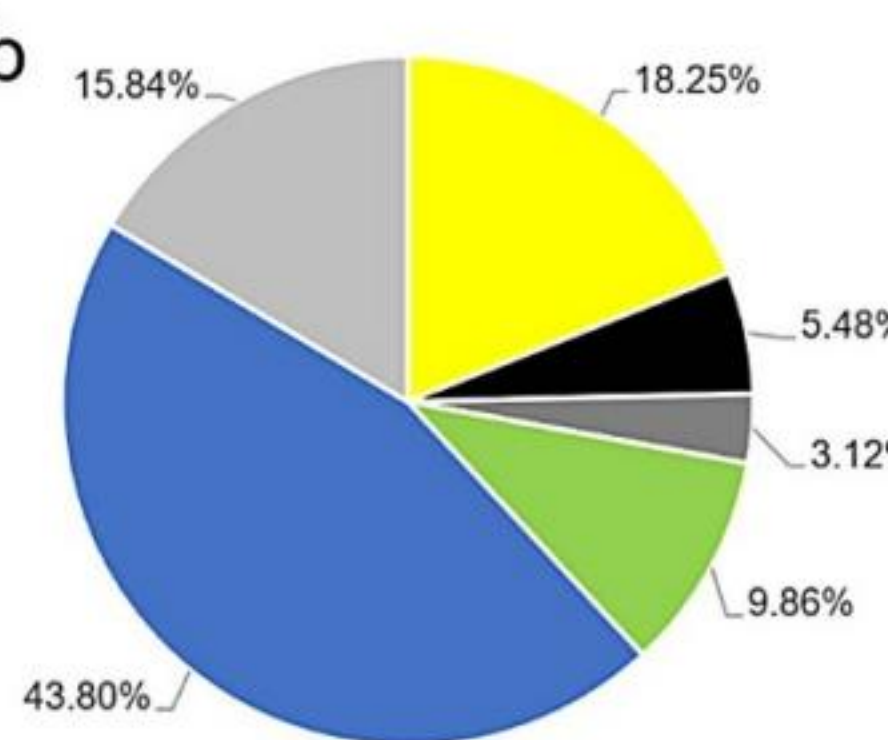


Figure 12. Schematics demonstrating the strategies employed to confine LiPSs. Within the cathode, LiPSs are prevented from diffusing into the bulk electrolyte by tortuous carbon matrices with long diffusion pathways (a), or by the adsorption of LiPSs onto chemical additives (red particles) doped on the C surface (b). (c) Interlayers (green section on separator) use chemical additives to adsorb LiPSs onto their surfaces, restricting the shuttle effect to the cathodic side of the battery, whilst maintaining

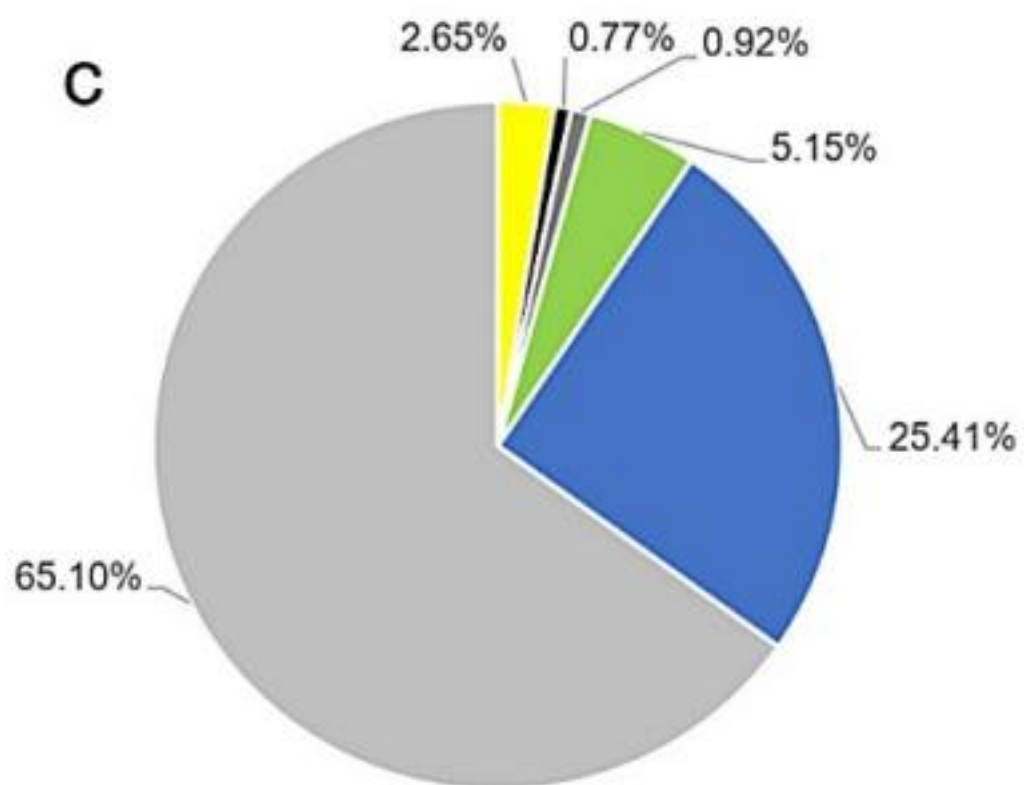
mass distribution in coin cell



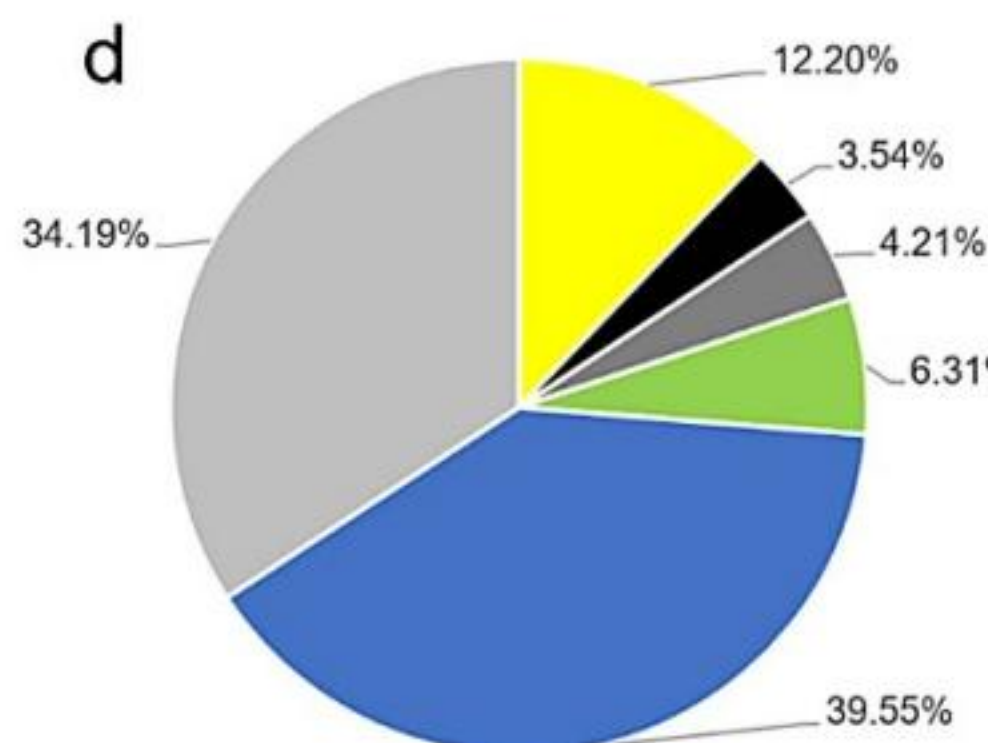
mass distribution in pouch cell



volume distribution in coin cell



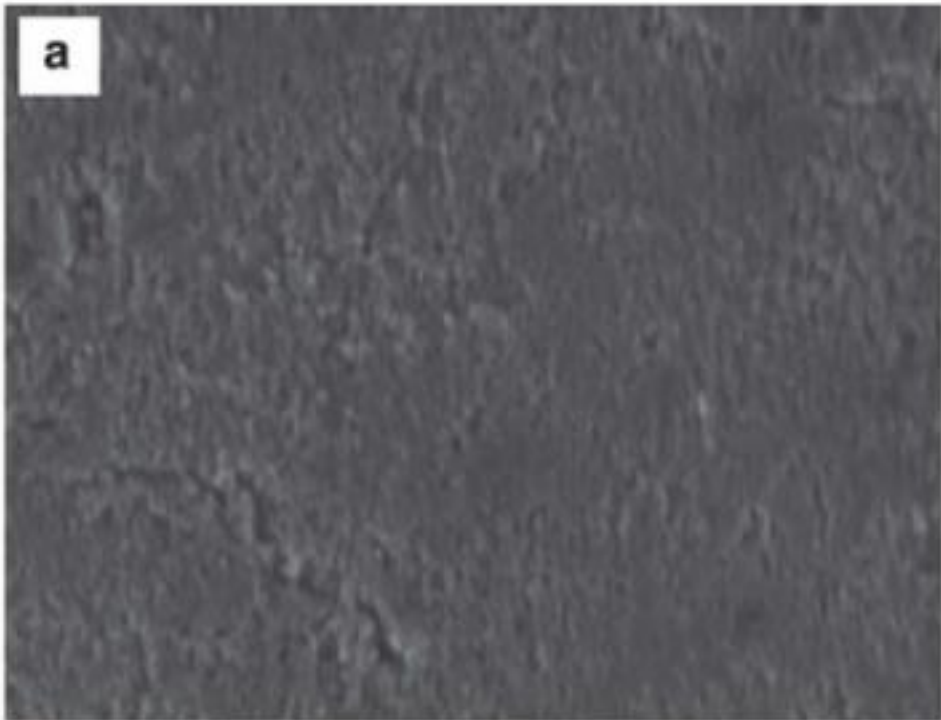
volume distribution in pouch cell



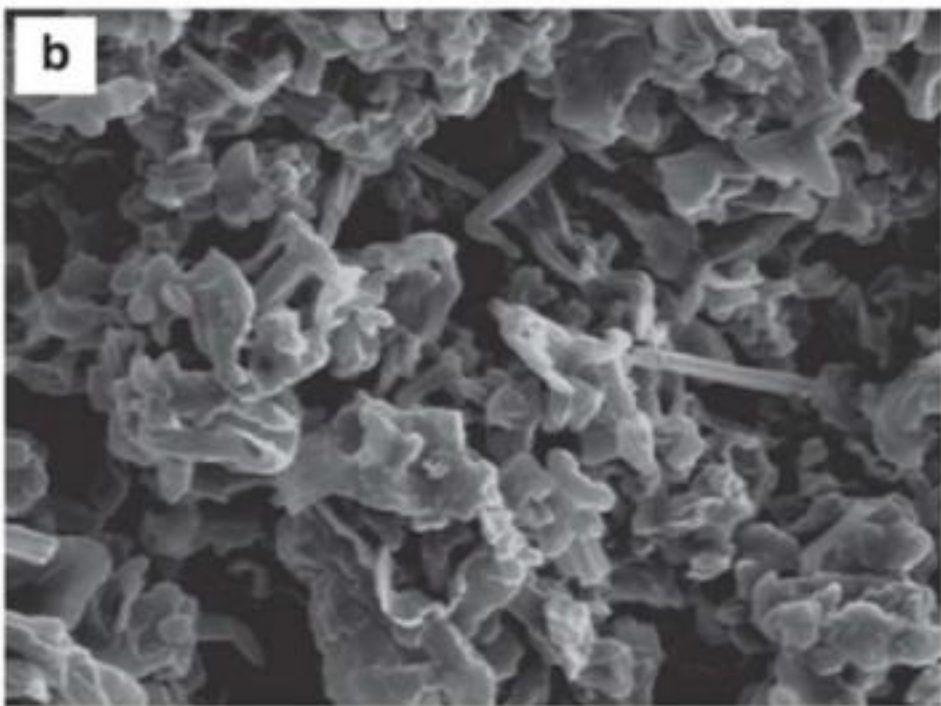
- █ Sulfur cathode
- █ Carbon + binder
- █ Al current collector
- █ Separator
- █ Electrolyte
- █ Lithium anode

Figure 1. Mass distribution in (a) coin and (b) pouch cells. Volume distribution in (c) coin and (d) pouch cells. Calculation parameters for pouch cells: S content = 80%; S loading = 6 mg cm^{-2} ; E/S = $2 \mu\text{l mg}^{-1}$; N/P = 2; PP separator

a



b



10 μm

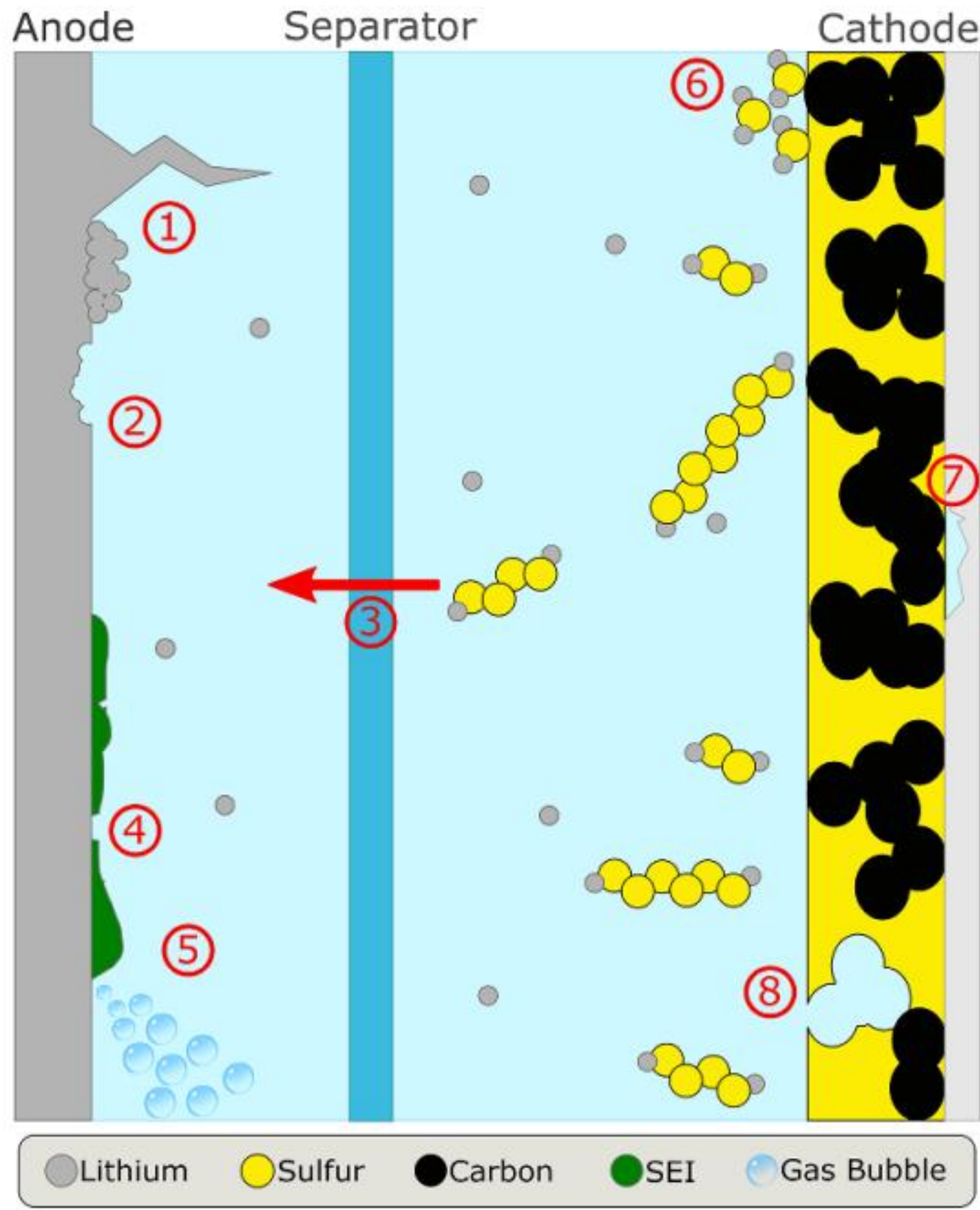


Figure 25. Schematic overview of the degradation processes in Li–S cells, many of which can lead to cell failure and safety issues.

unreacted metallic Li⁰ trapped in SEI. (b) Li deposits with granular size and less tortuosity tend to maintain a good structural connection, in which only small amounts of metallic Li⁰ are stuck in tortuous SEI edges. (c) An ideal Li deposit should have a columnar microstructure with a large granular size, minimum tortuosity and homogeneous distribution of SEI components, facilitating a complete dissolution of metallic Li⁰. Reprinted by permission from Springer Nature Customer Service Centre GmbH: Springer Nature, *Nature* [44]. Quantifying inactive lithium in lithium metal batteries, C. Fang et al. © 2019.

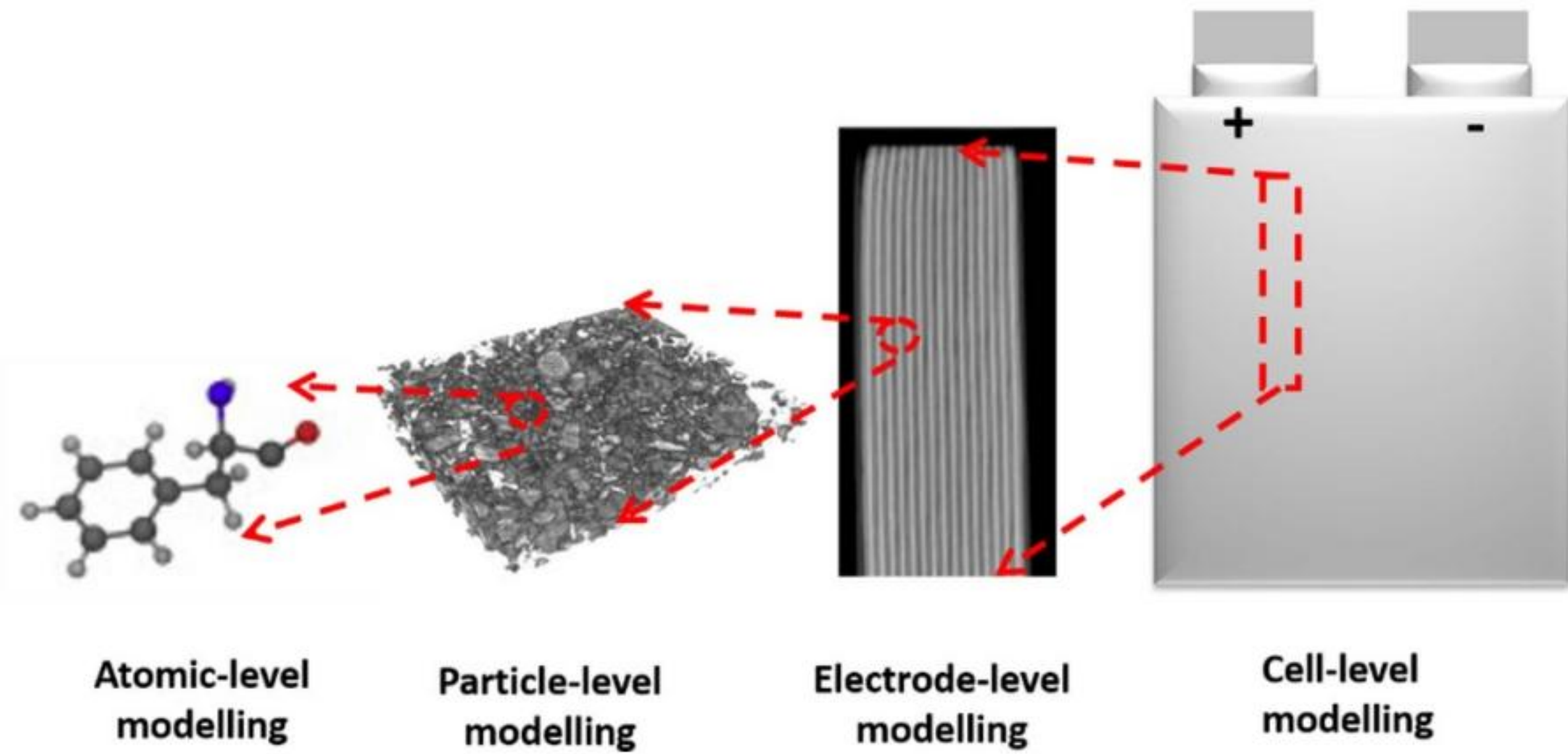
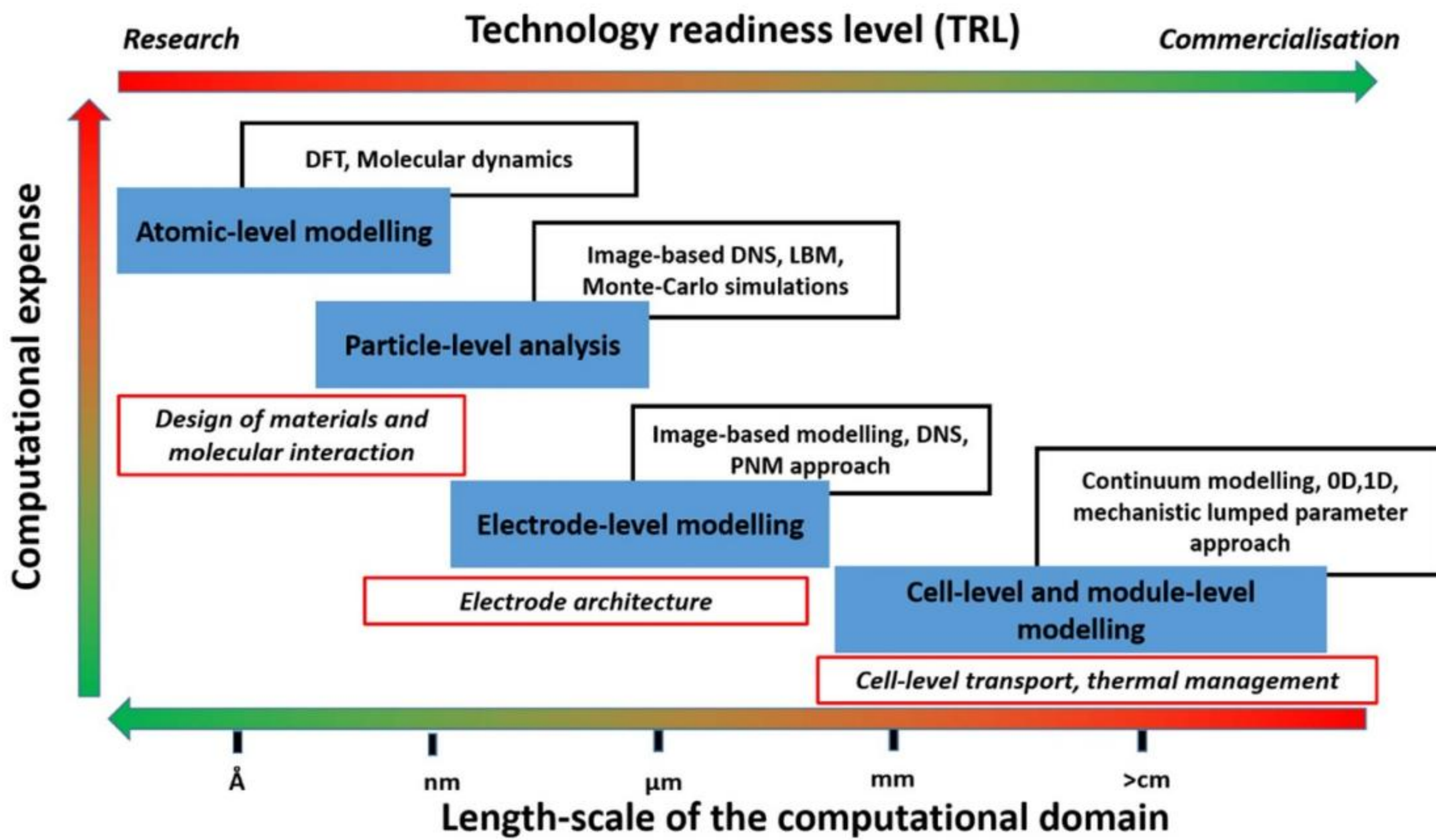


Figure 19. Multiscale modelling platform for LiSB modelling. This provides an overview of the cost and length scales involved in LiSB modelling. The diagram illustrates the need for a multiscale approach to model the complex phenomena occurring in LiSBs.

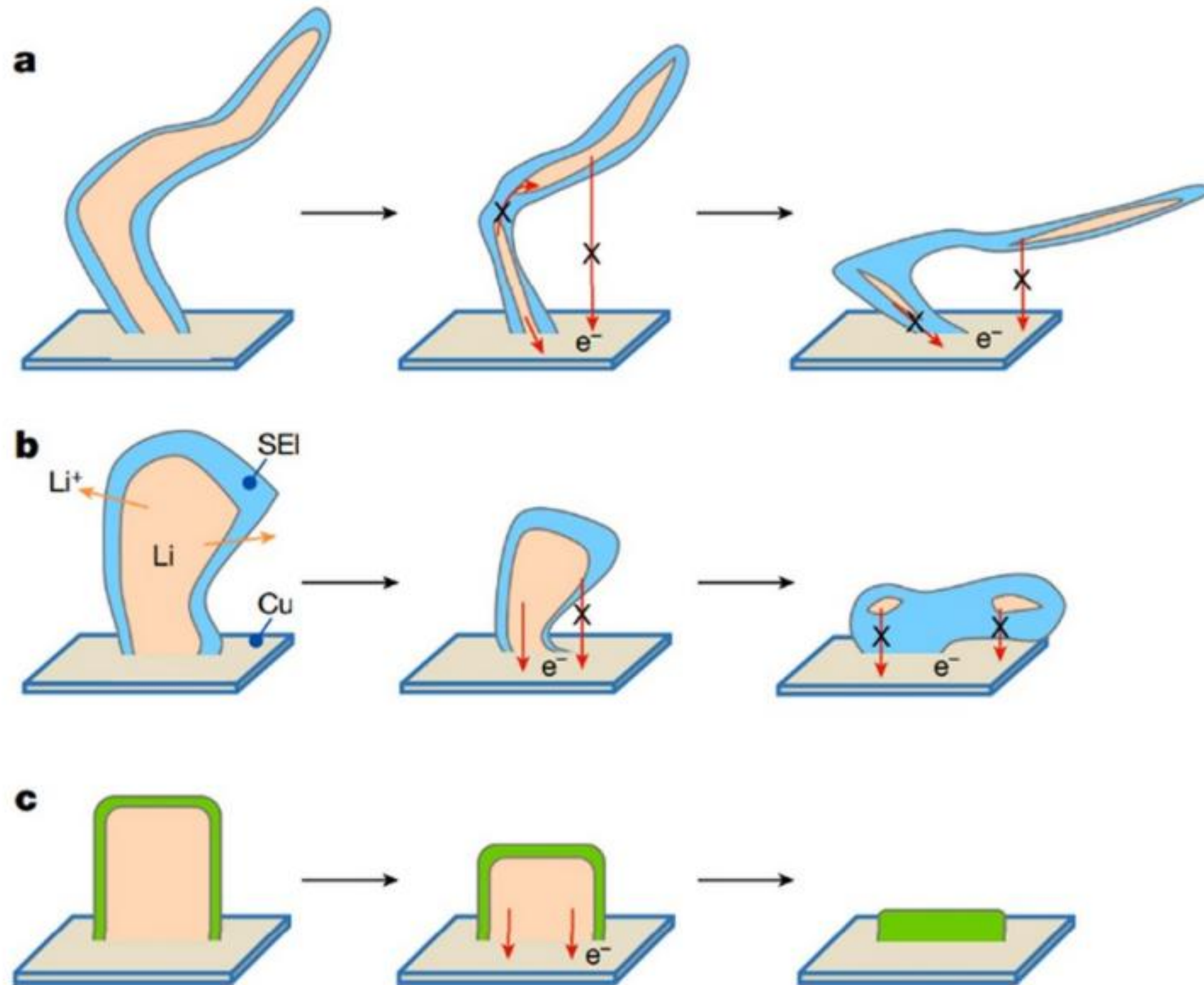
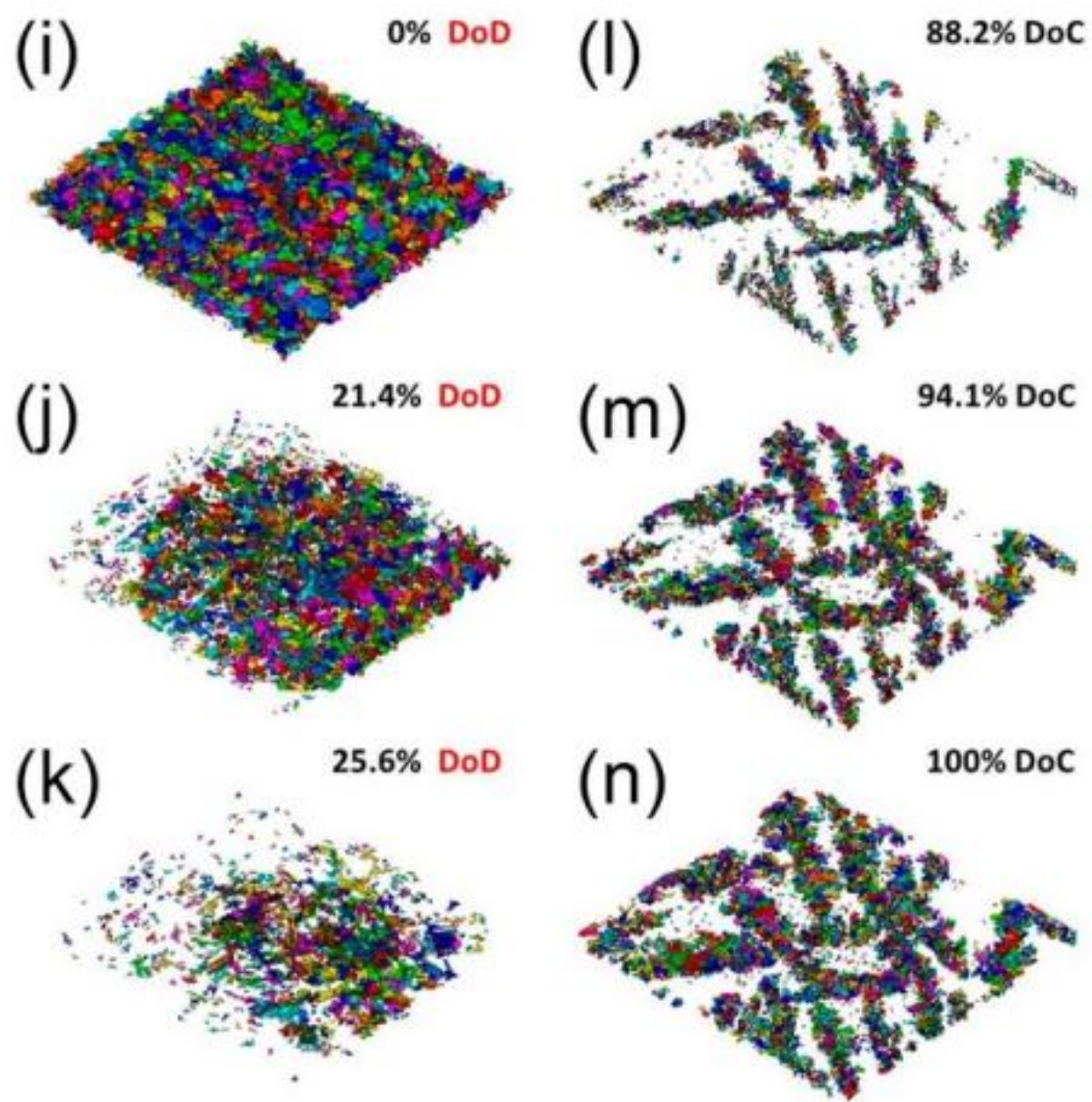
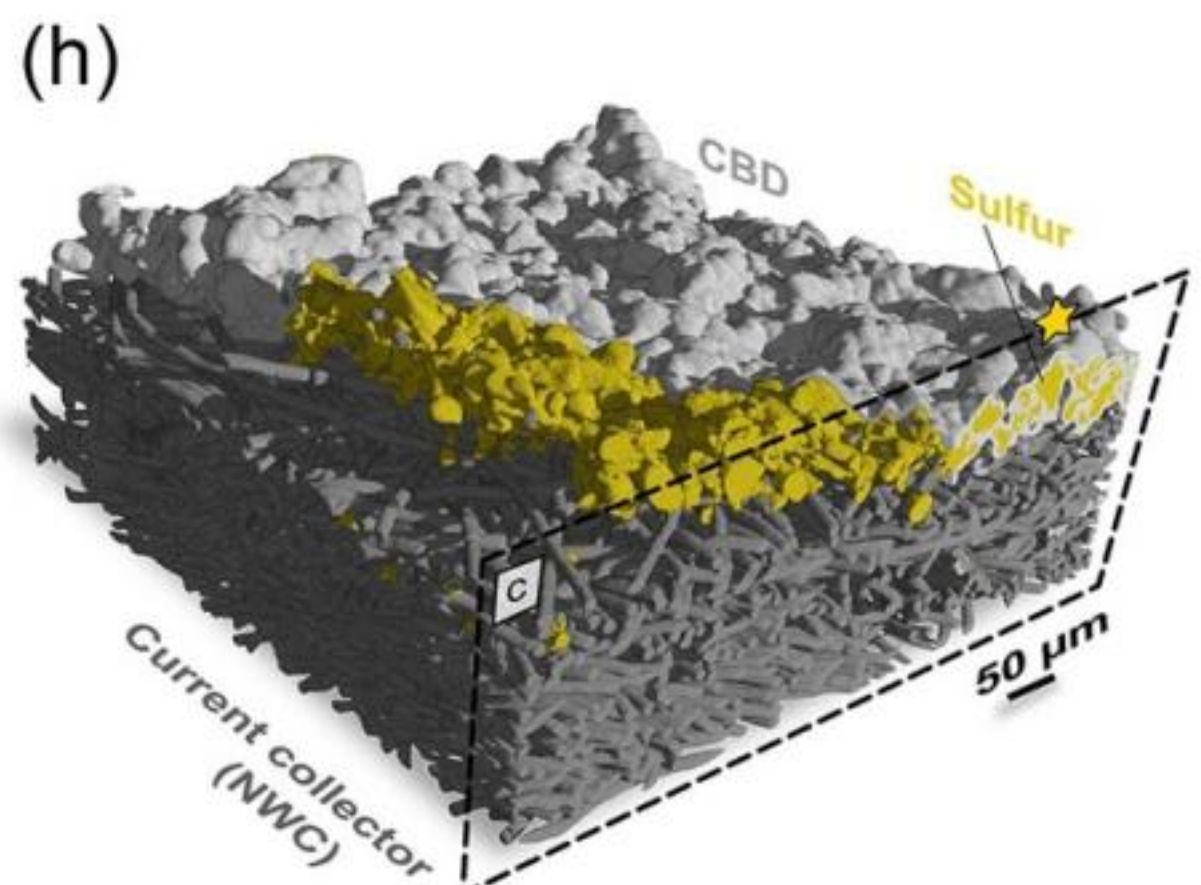
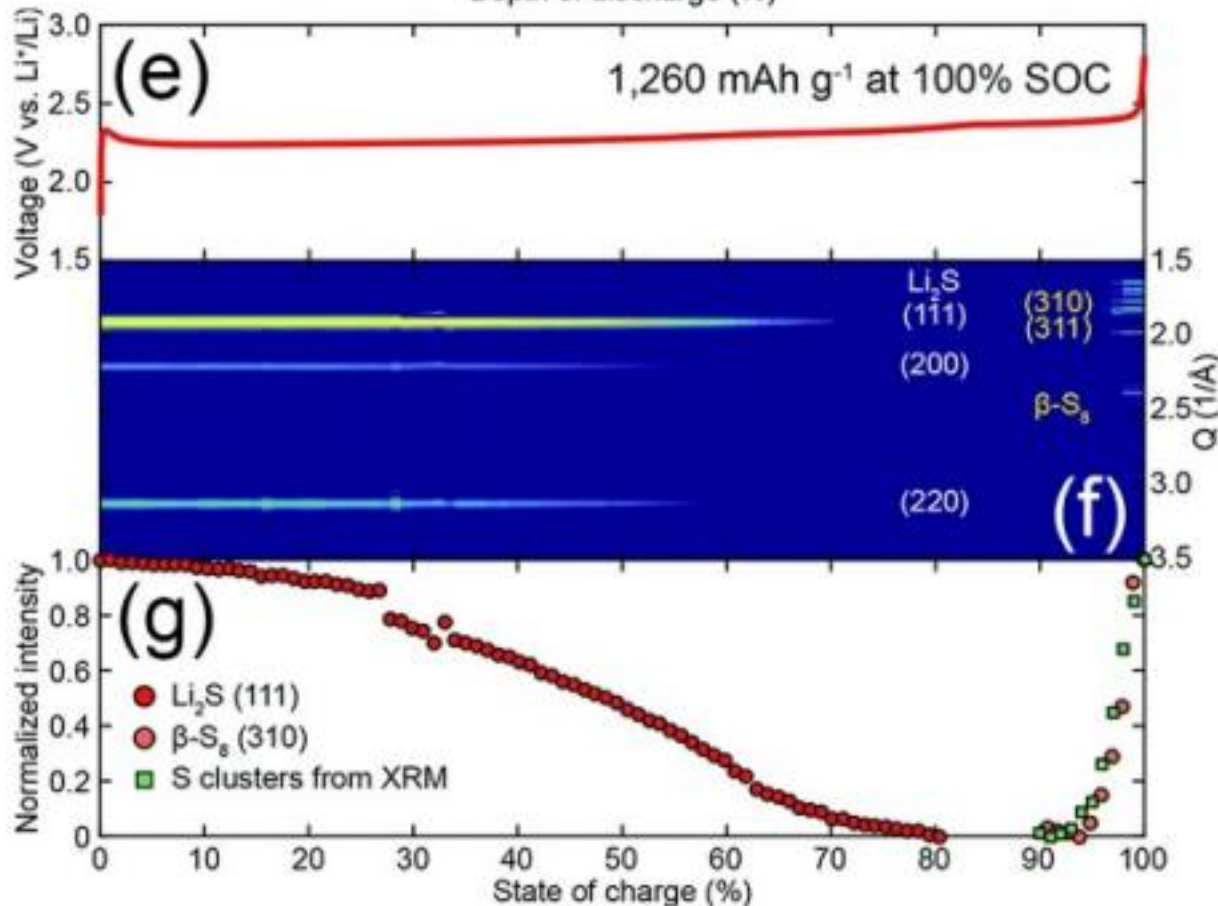
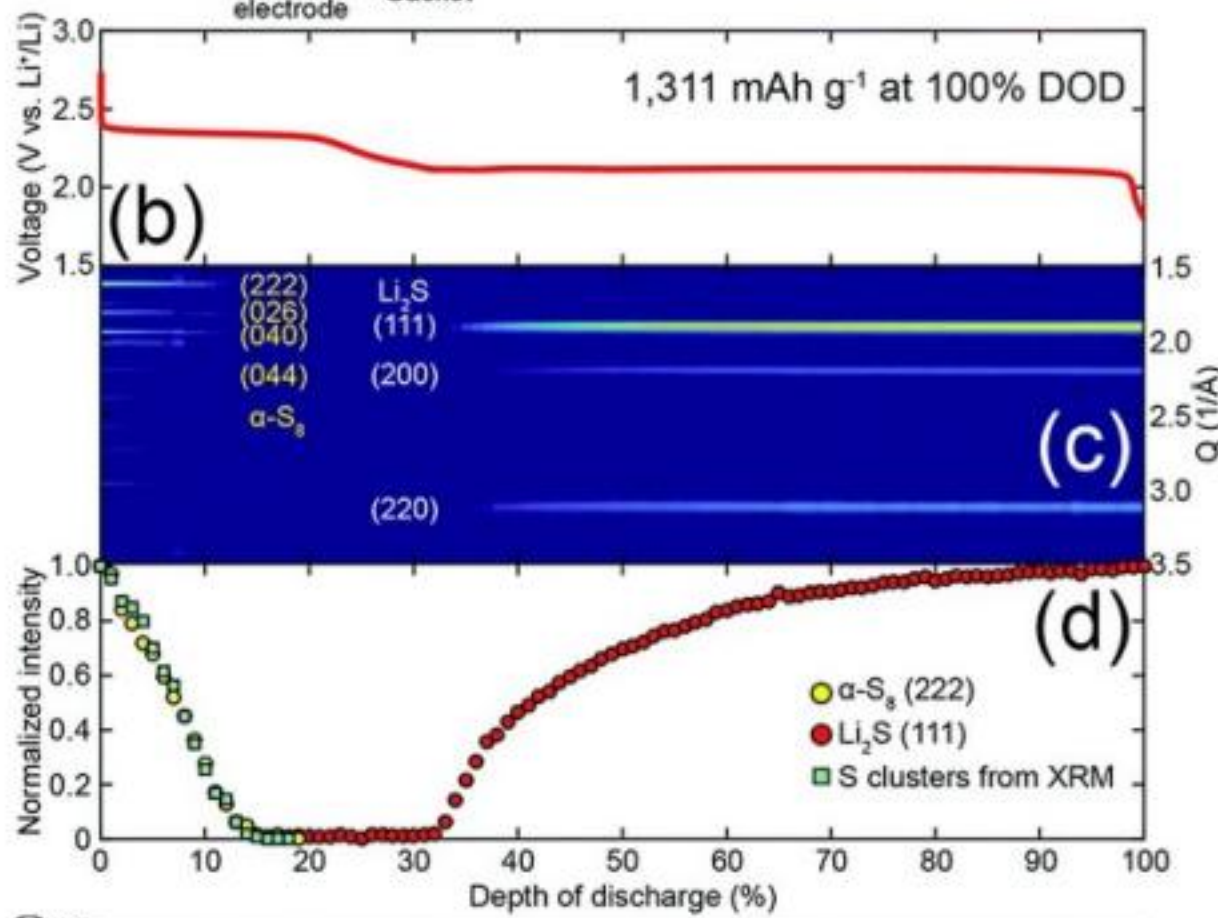
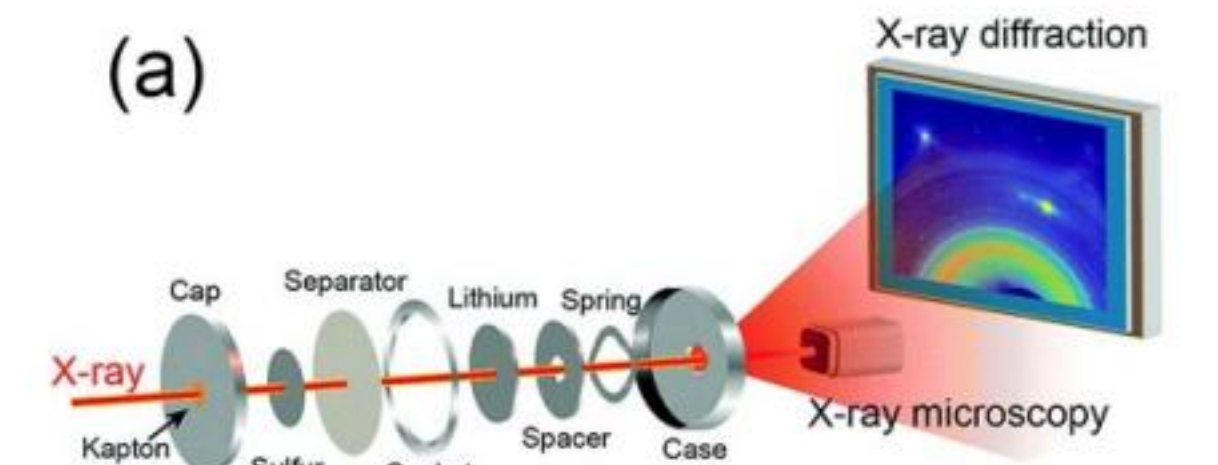
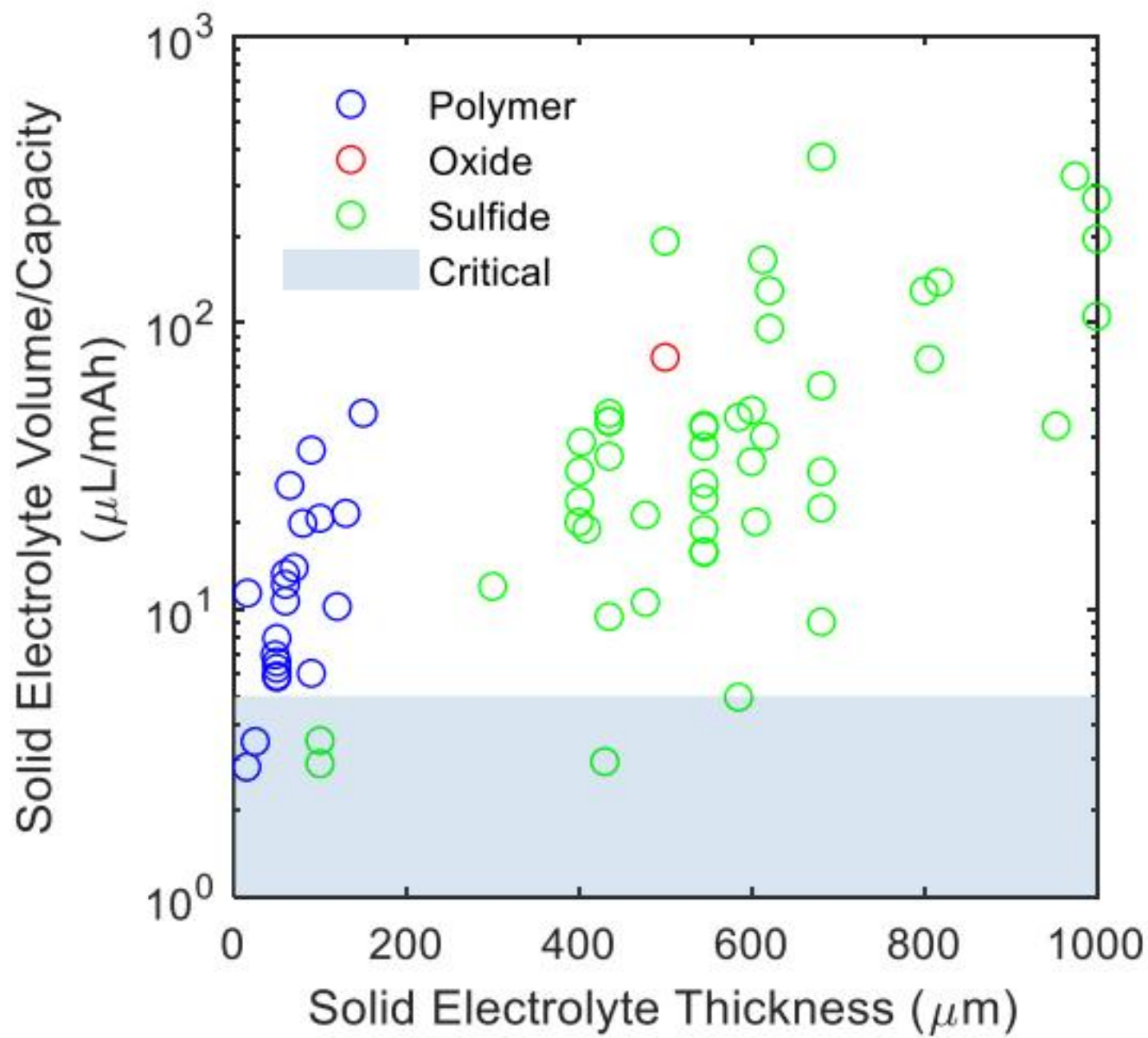


Figure 5. Schematic of inactive Li formation mechanism in different electrolytes. (a) Li deposits with whisker morphology and high tortuosity are more likely to lose electronic connection and maintain poor structural connection, leaving large amounts of unreacted metallic Li^0 trapped in SEI. (b) Li deposits with granular size and less tortuosity tend to maintain a good structural





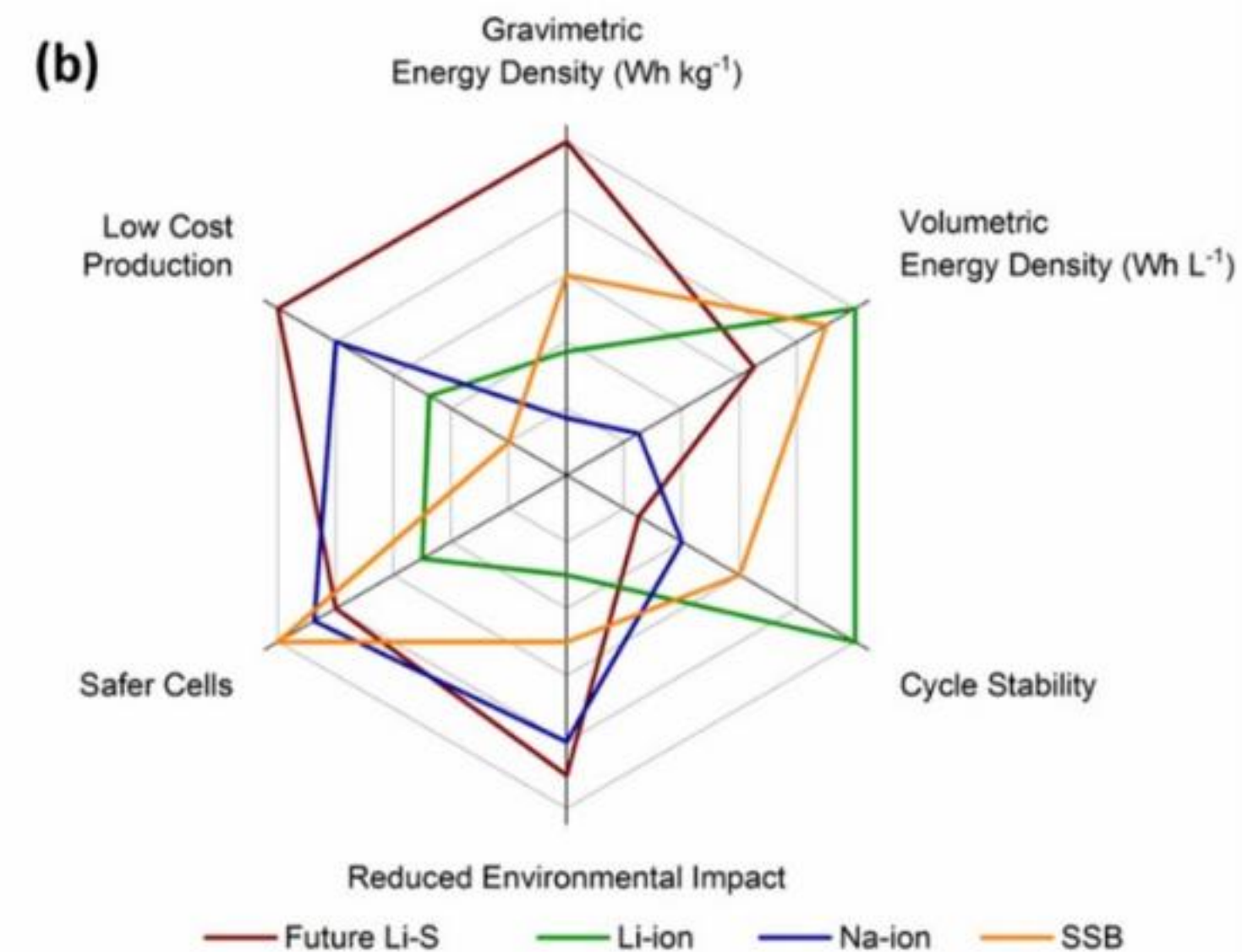
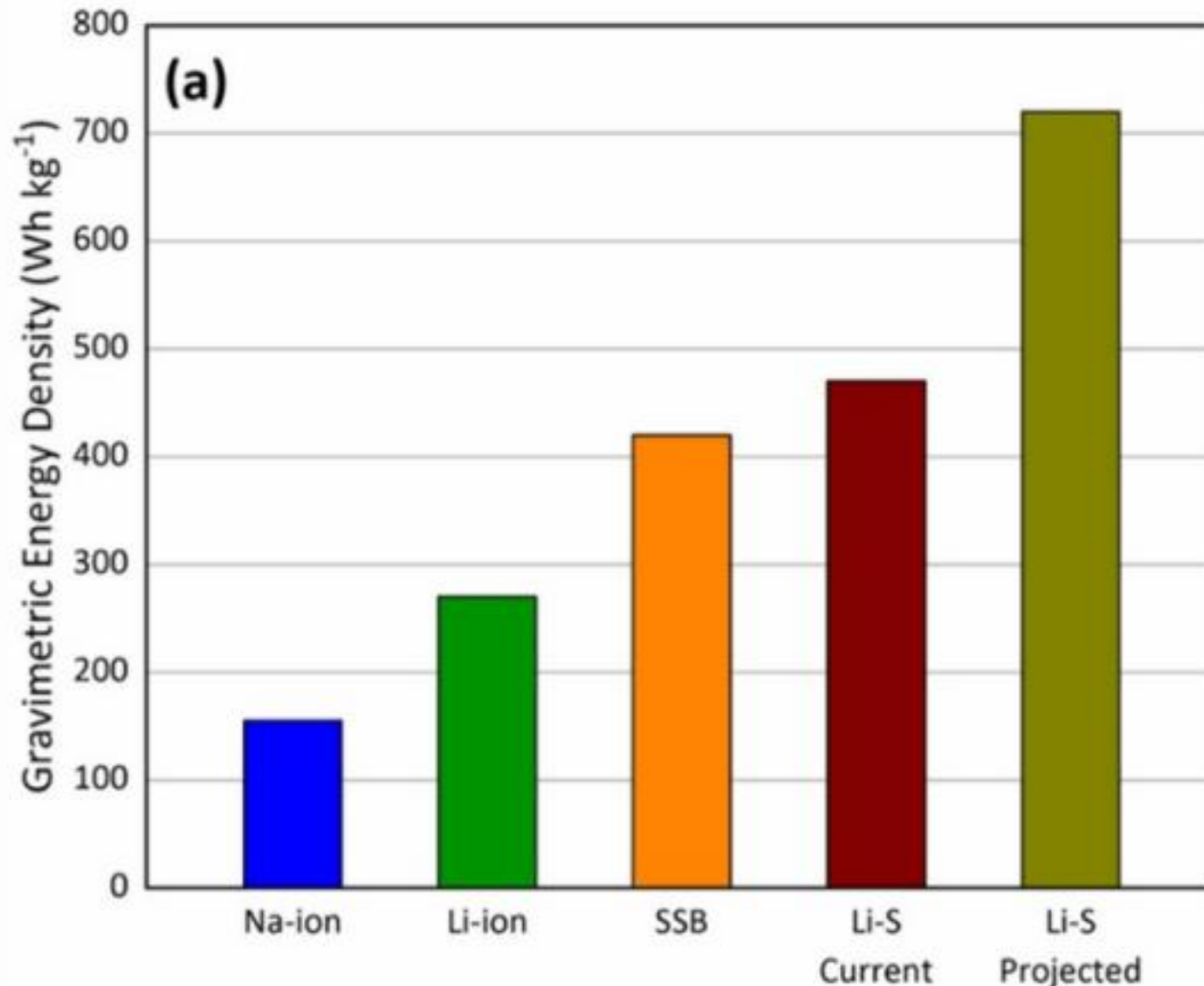


Figure 29. (a) Comparison of the predicted and demonstrated gravimetric energy density of Li–S cells compared to alternative battery technologies and (b) indicative overview of the strengths of a range of commercial or near-commercial battery

Figure 15. Typical example of a LiSB with a coated separator. (a) Cross-sectional SEM image of the interface between the carbon black-coated separator and the cathode (60 wt% S). (b) Li–S cell cycling stability comparison at cycle rate C/5 of different nanomaterial coatings on separators. Reproduced from [101] with permissions of The Royal Society of Chemistry.

Figure 4. Predicted gravimetric energy density based on the total mass of a cathode containing S, carbon matrix, carbon black and carboxymethyl cellulose-styrene-butadiene rubber (CMC-SBR) in the ratio 59:17:18:6; and volumetric energy density based on the comprehensive volume of the cathode. The insets show schematics of the difference between low porosity and high porosity. Unutilised S, carbon matrix, and deposited $\text{Li}_2\text{S}_2/\text{Li}_2\text{S}$ layer are represented as yellow, black, and red, respectively. Reproduced from [31]. CC BY 4.0.

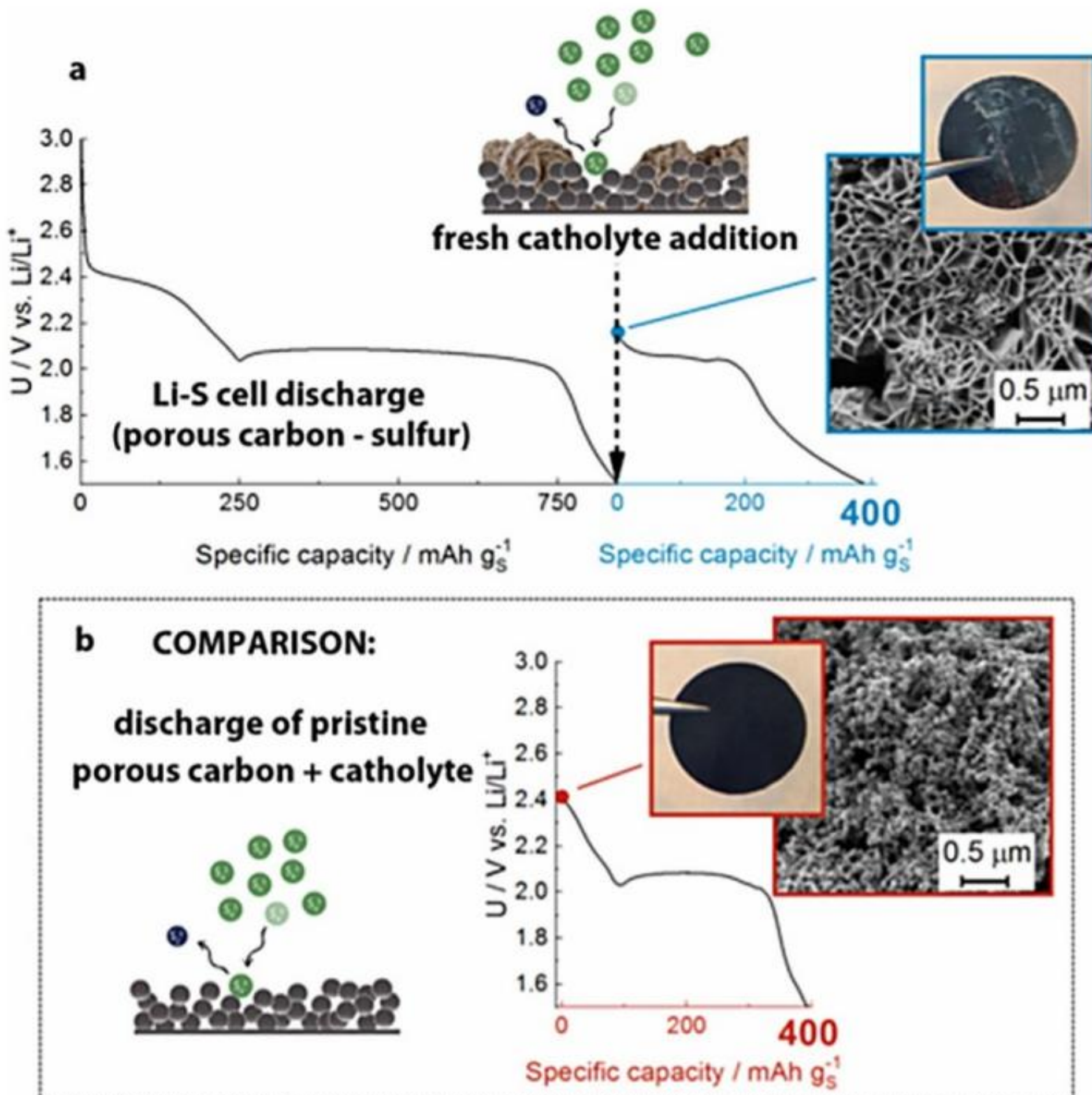
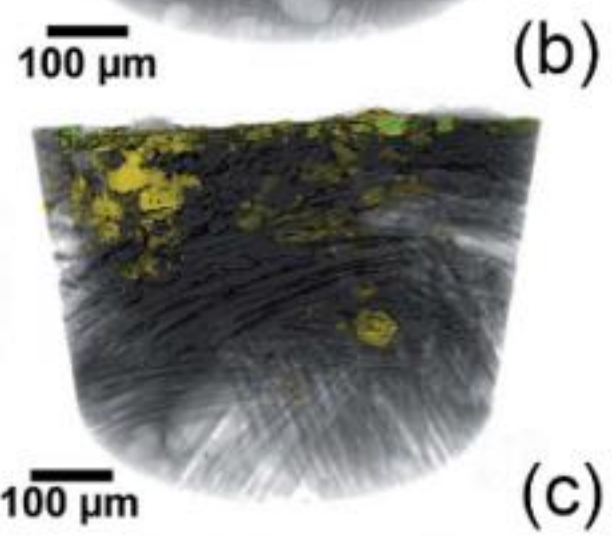
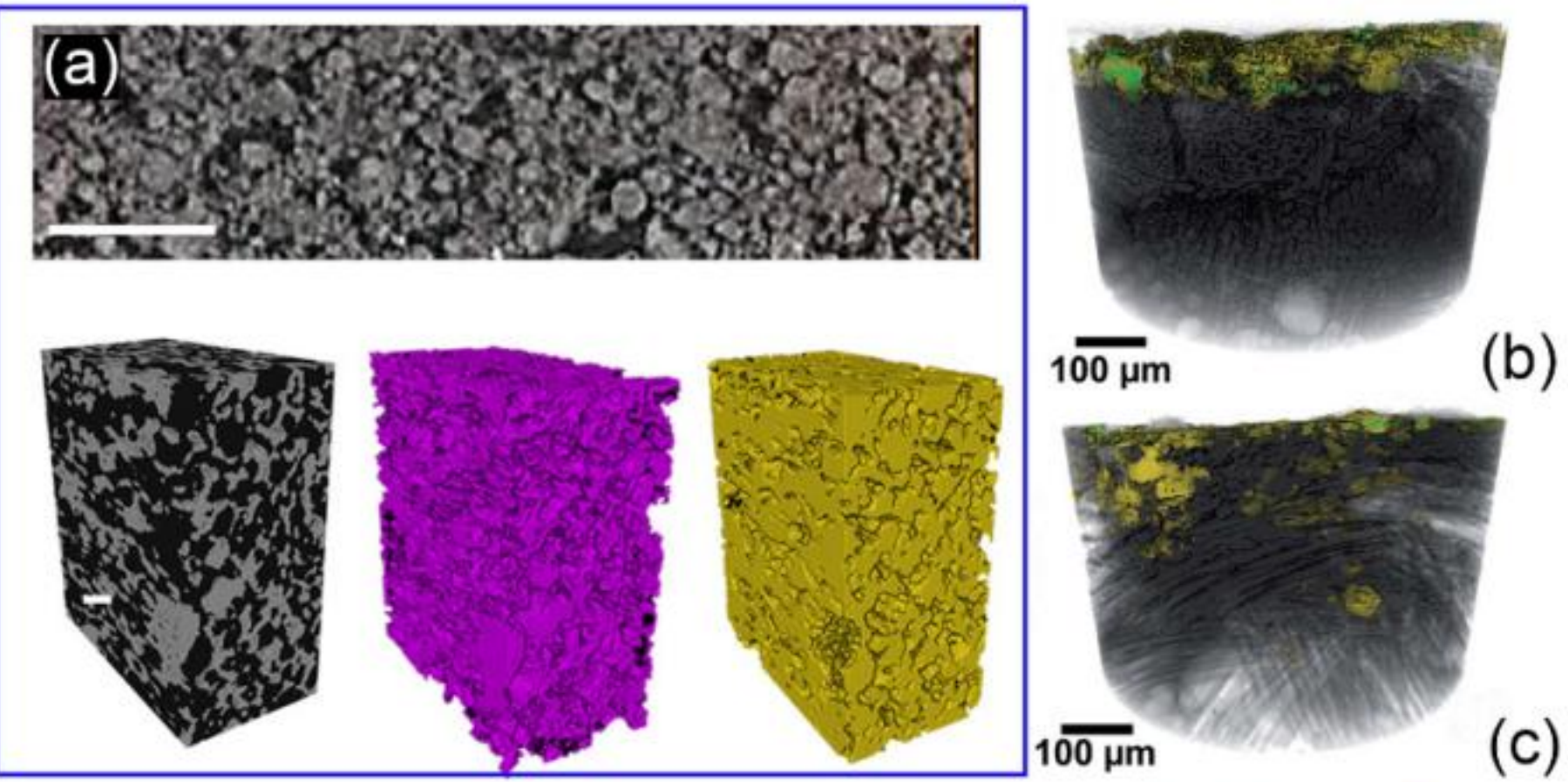


Figure 10. (a) Complete discharge of a typical LiSB followed by the addition of a fresh catholyte solution (0.1 M Li_2S_8) creating an additional discharge capacity and (b) a control experiment looking at the discharge capacity of the added catholyte solution with a porous carbon electrode [68]. Reprinted with permission from [68]. © 2019 American Chemical Society.



(c)

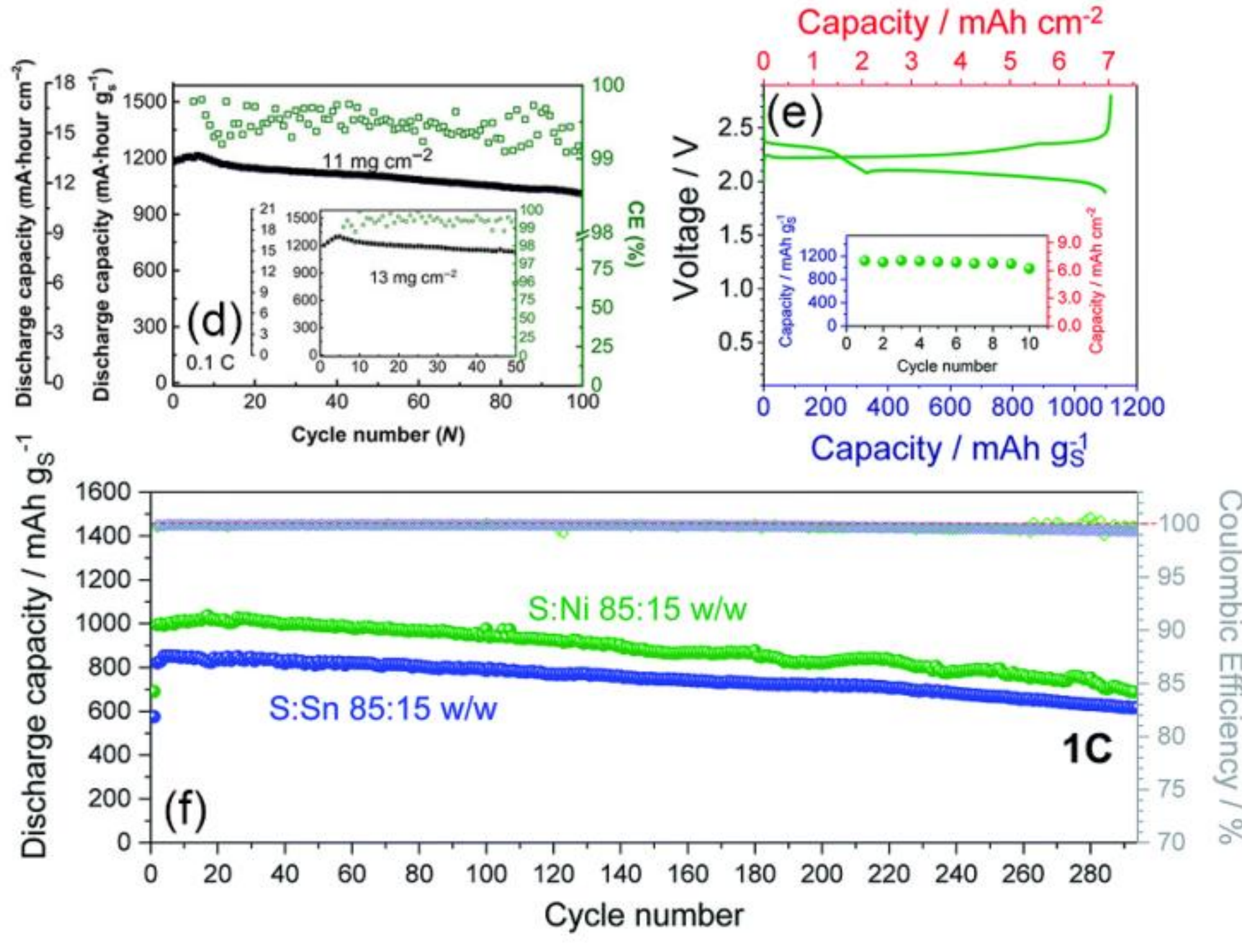


Figure 24. (a) Slice extracted from a tomographic reconstruction of an expansion-tolerant S cathode prepared by controlling the dispersion of the components and using low amounts of a high-modulus binder (top) and related volume renderings of a portion

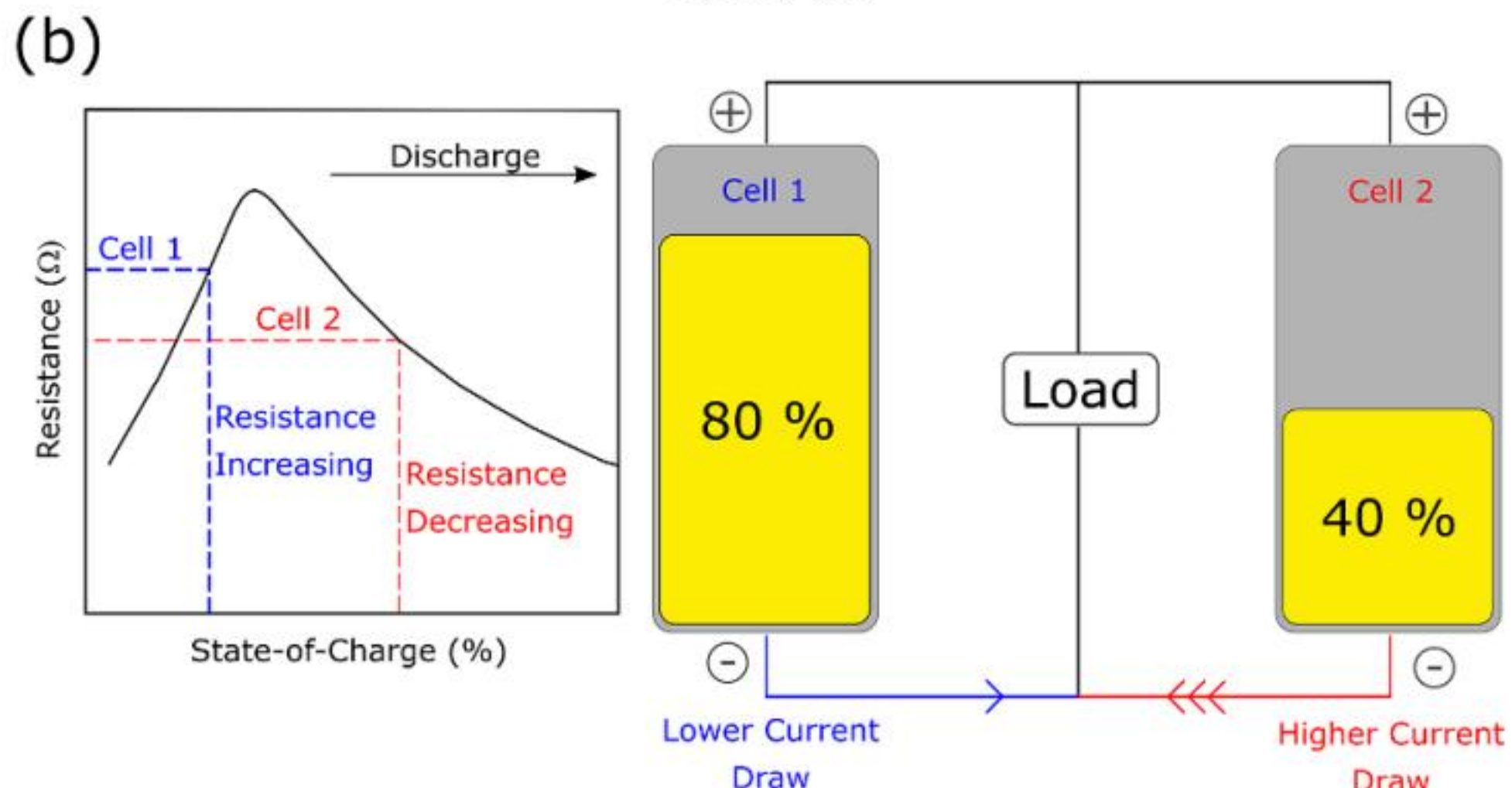
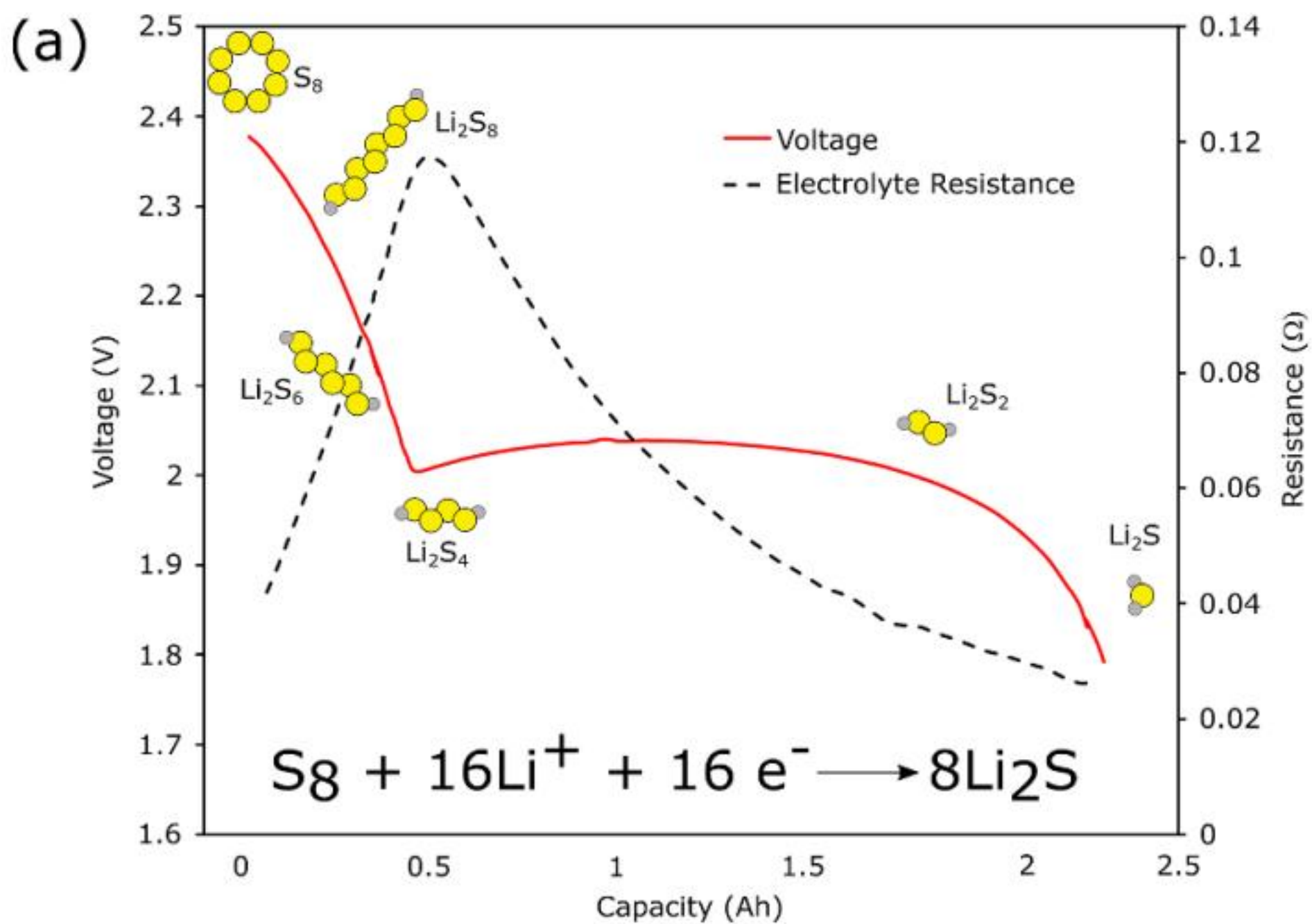
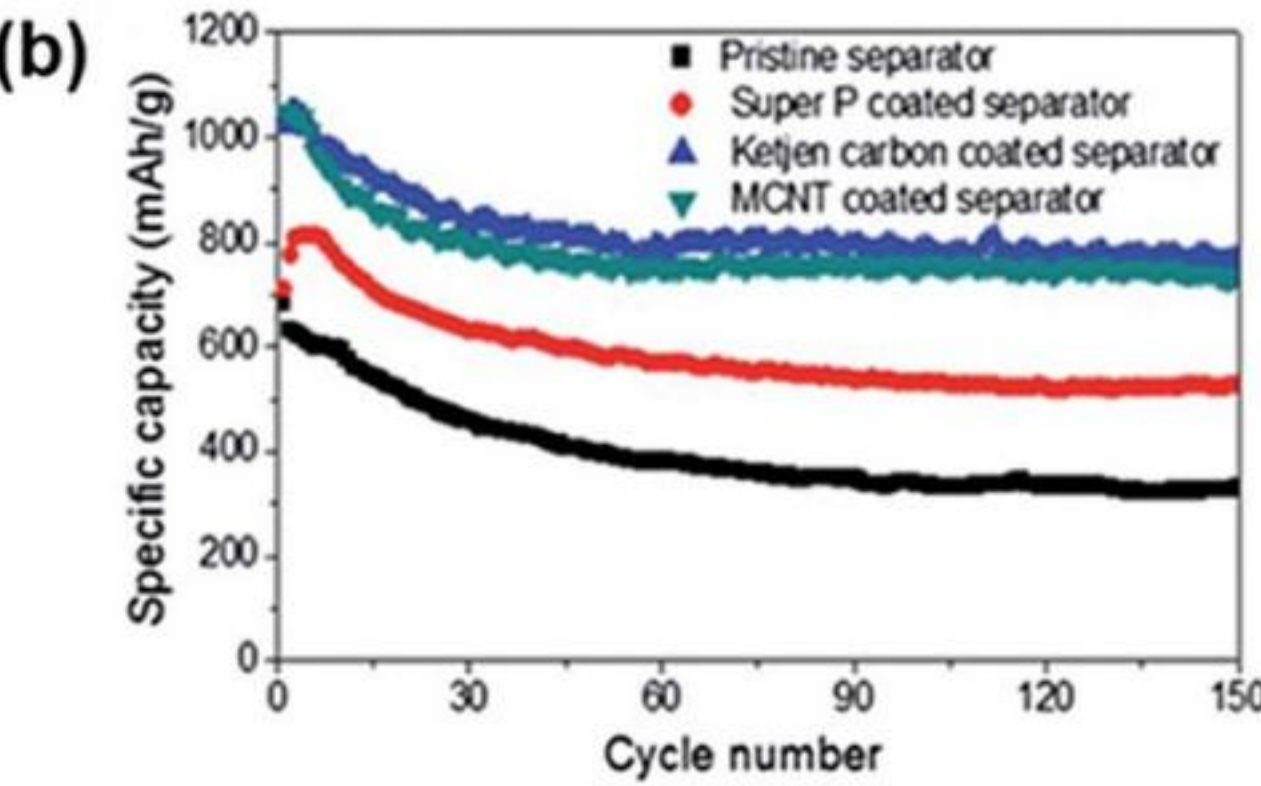
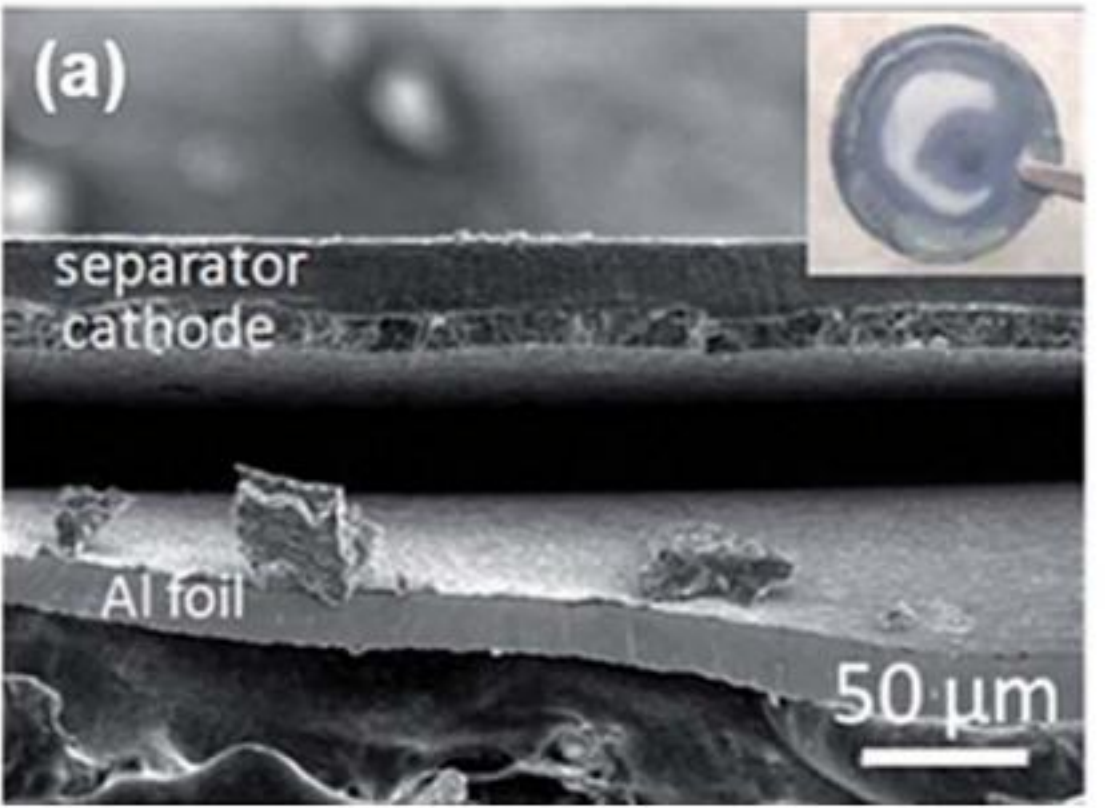
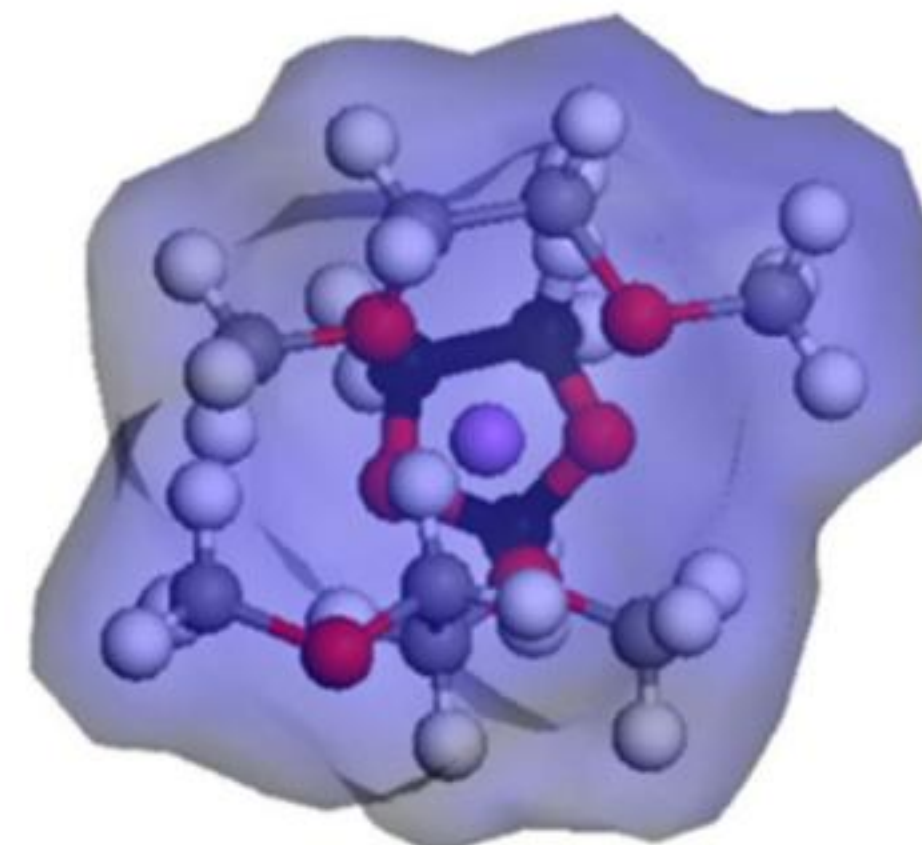
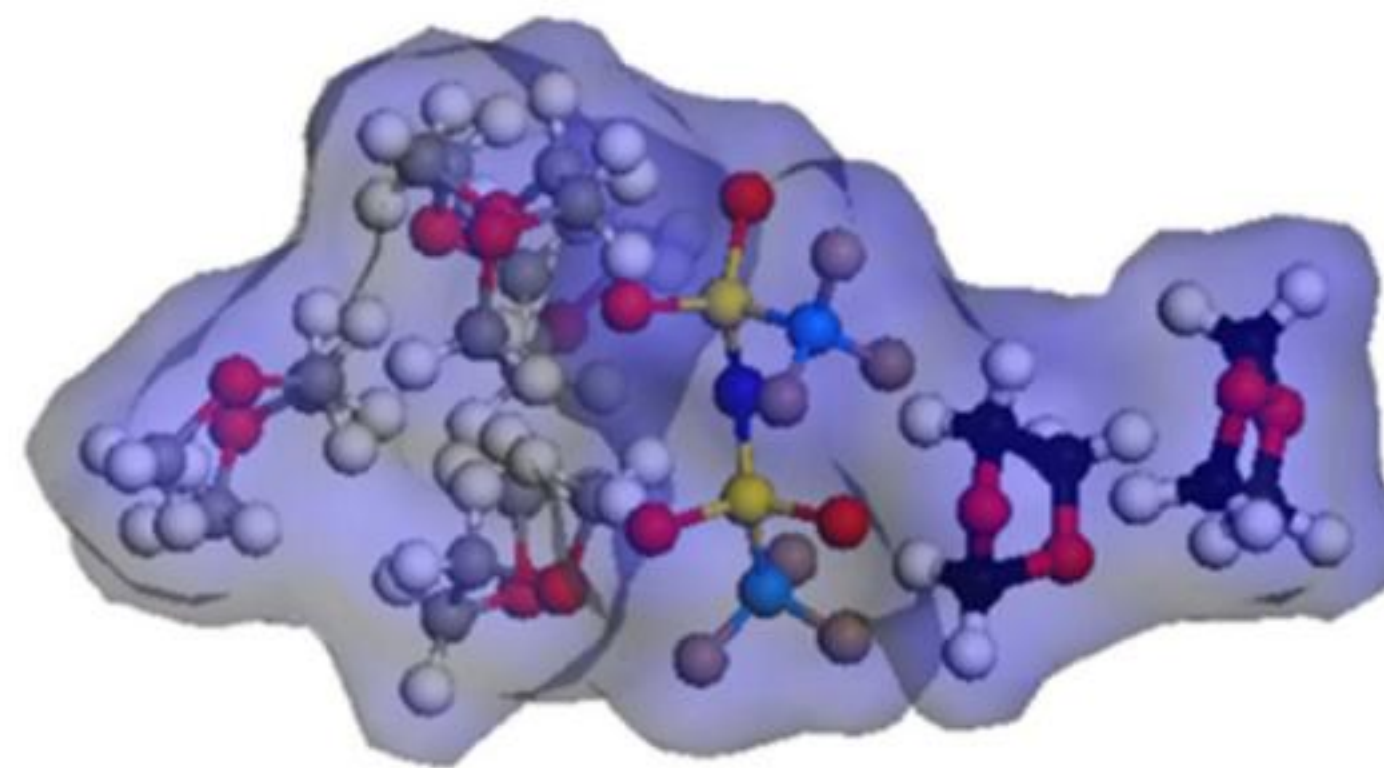


Figure 26. (a) Representation of how voltage and resistance vary in a typical LiSB during discharge. The peak in electrolyte resistance due to PS dissolution results in the observed voltage minimum between plateaus. A relatively flat voltage profile is





$\text{Li}^+/1\text{DOL}:2\text{DME}$



$\text{TFSI}^-/2\text{DOL}:4\text{DME}$

Figure 17. Solvated electrolyte ion structures for electrolyte LiTFSI in DOL:DME with van der Waals surface, derived from MM simulations using Materials Studio v6.1.0 and the compass force field model for the solvated Li^+ ion and the Dreiding force field model for the solvated TFSI^- ion.

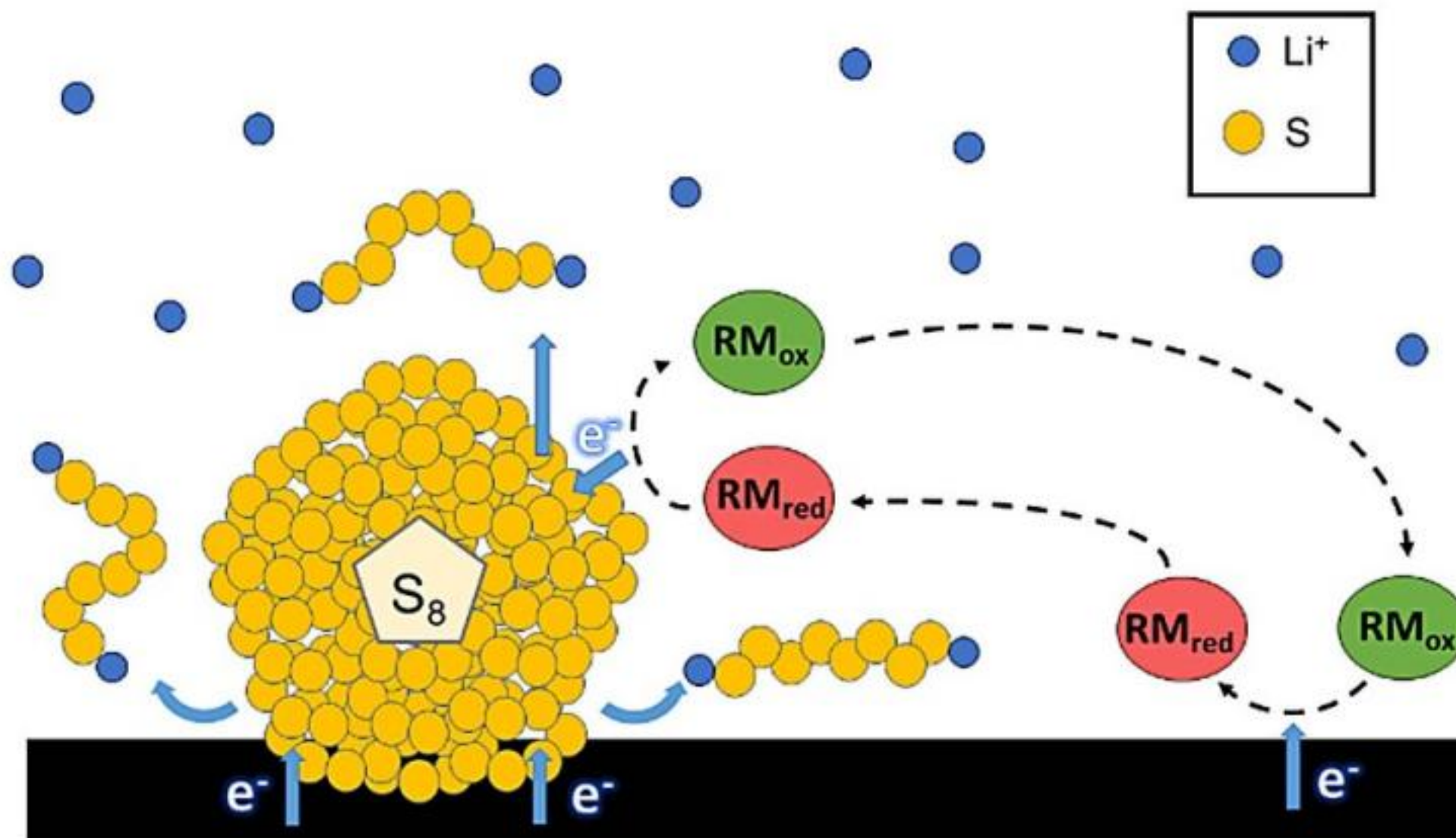
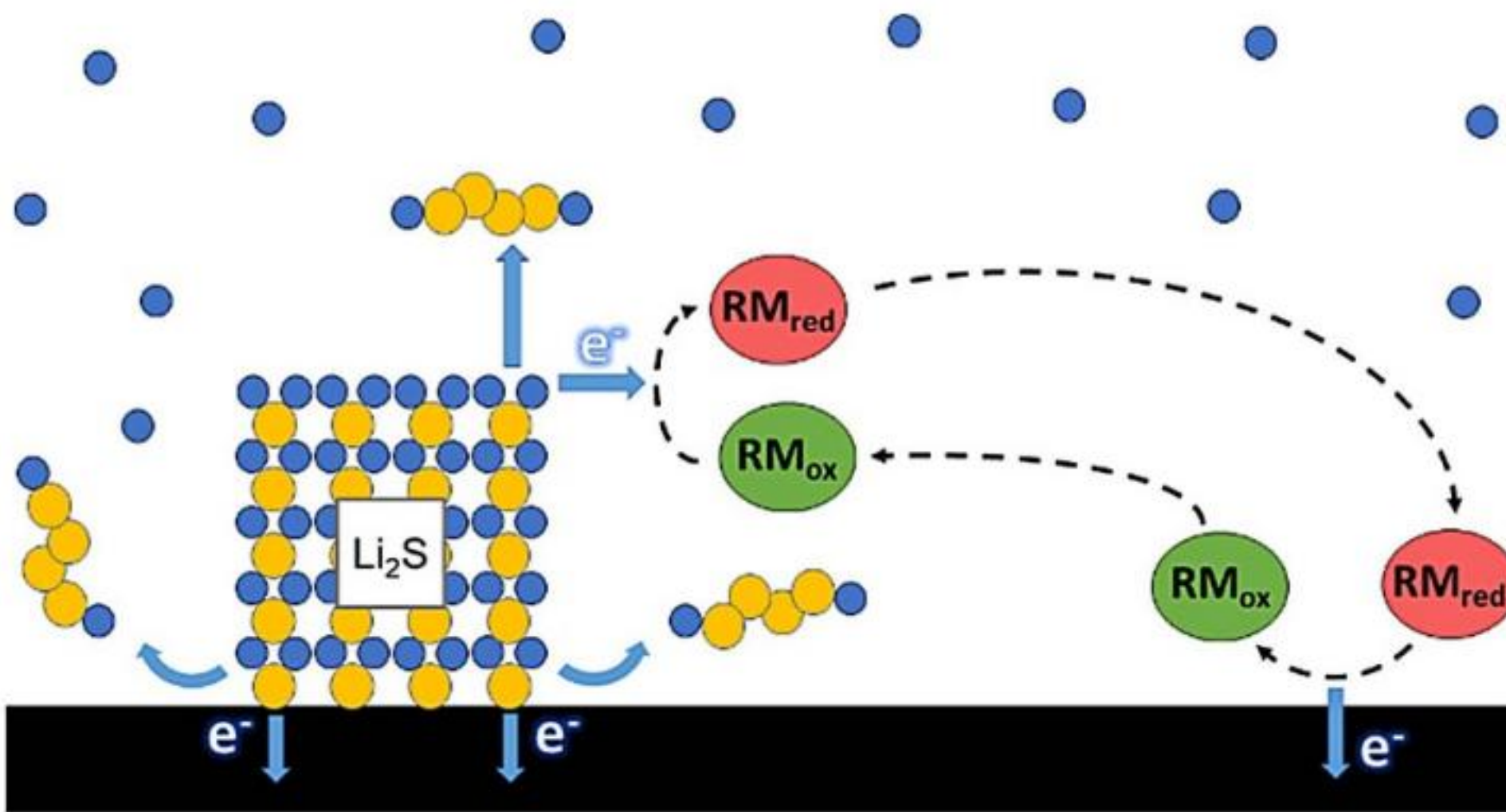


Figure 11. Schematic showing the operating principle behind the use of RMs for (a) the reduction of S_8 to long-chain PSs and (b) the oxidation of Li_2S to short-chain PSs.

Figure 9. Proposed reaction mechanism involving chemical PS reduction (VI.1 to VI.7) in the pathway of S_1^{2-} formation [64]. © 2014 American Chemical Society.

Li-S prototype pouch cells

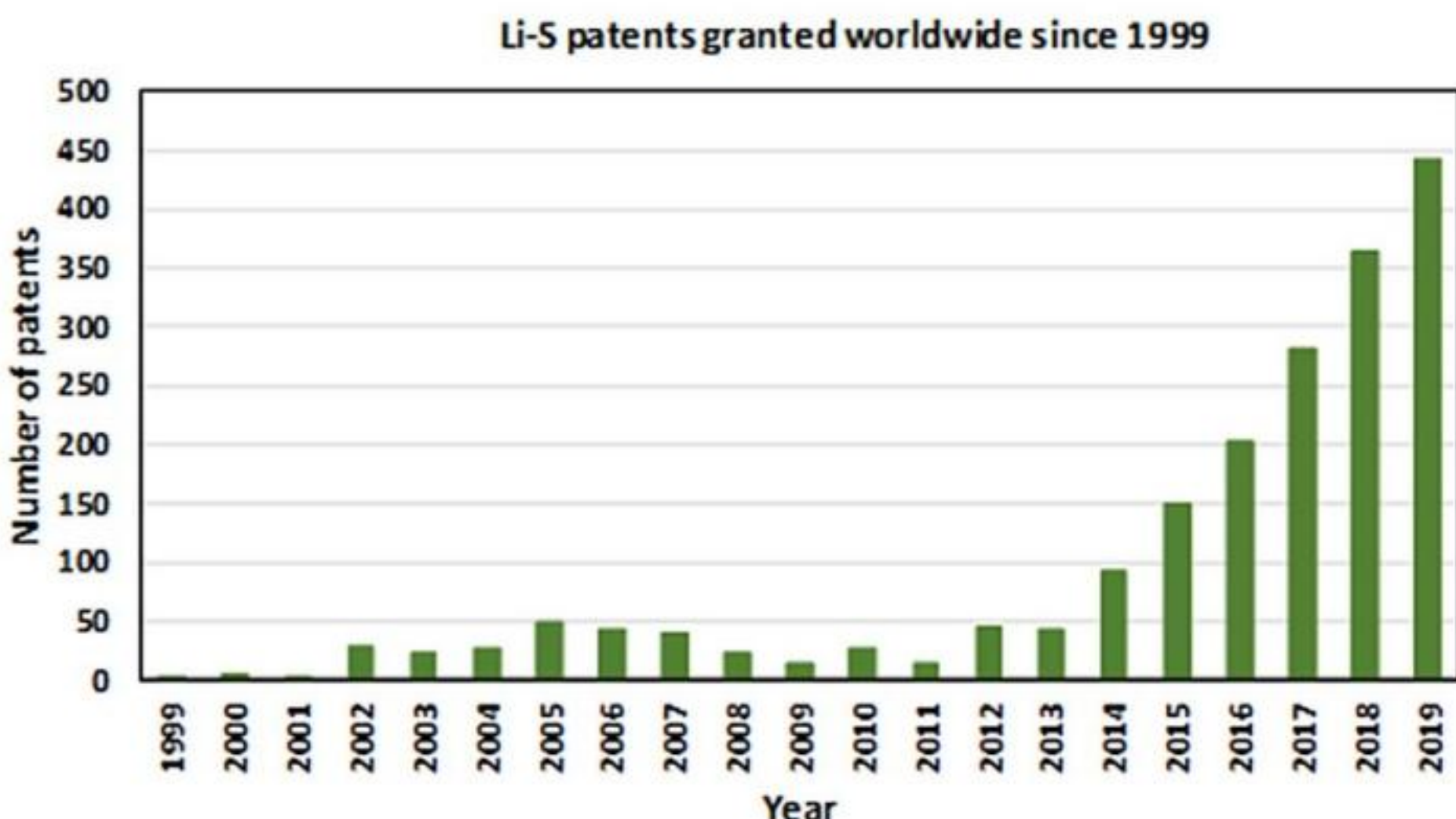


Figure 27. Example of high-capacity Li–S pouch cells from OXIS Energy (top). Worldwide granted patents in the field of Li–S technology (bottom).

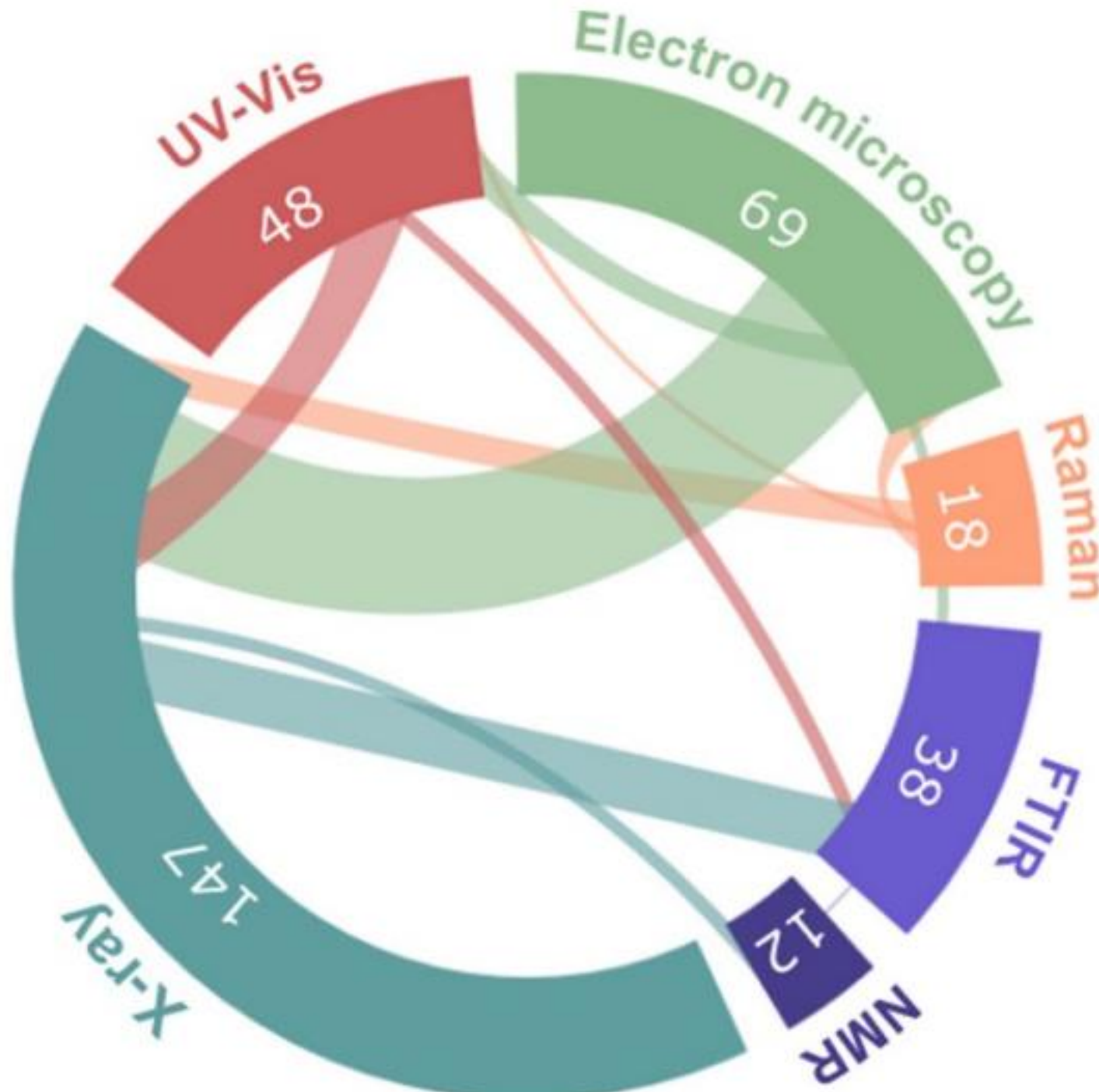


Figure 22. Number of research articles on the Web of Science database as of 2020 with ‘lithium–sulfur’ or ‘Li–S’ in the title and ‘*in situ*’ in the title, abstract or keywords. Links show the number of articles that include both keywords.

Figure 18. Diagram of continuum volume-averaged model for an electrochemical cell including anode, separator and cathode, taking into account the PSD of the cathode, and transport of solvated ions (wrapped by light blue-coloured shell of solvent molecules) or desolvated ions of the electrolyte as described in [122].

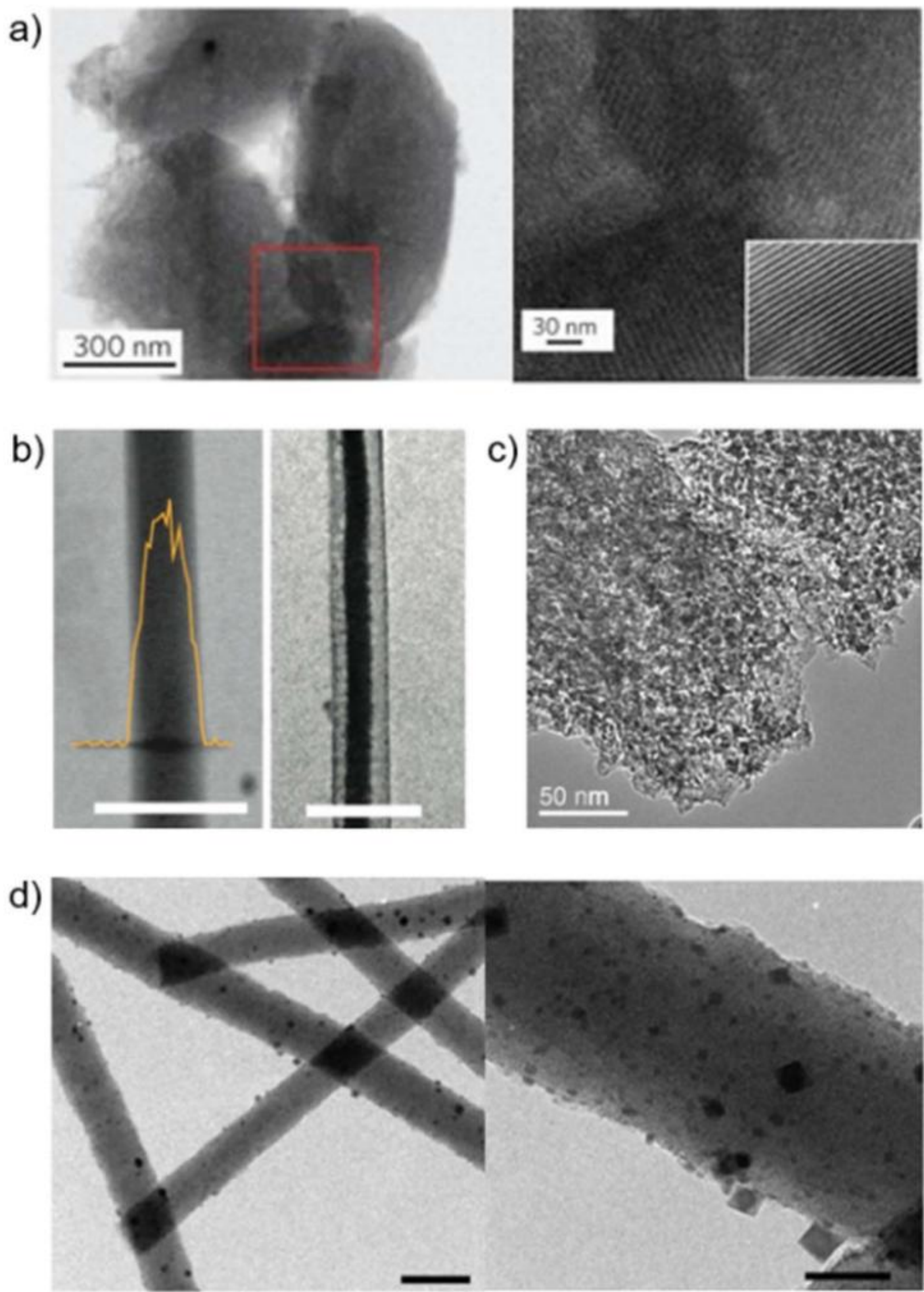


Figure 3. TEM images of different carbon morphologies used for S cathodes. (a) Ordered mesoporous carbon CMK-3/S composite particle (left), and image expansion corresponding to the area outlined by the red square (right) where the inset shows the TEM image for pristine CMK-3 at the same magnification. Reprinted by permission from Springer Nature Customer Centre GmbH: Springer Nature, *Nature Materials* [25]. A highly ordered nanostructured carbon–sulphur cathode for...

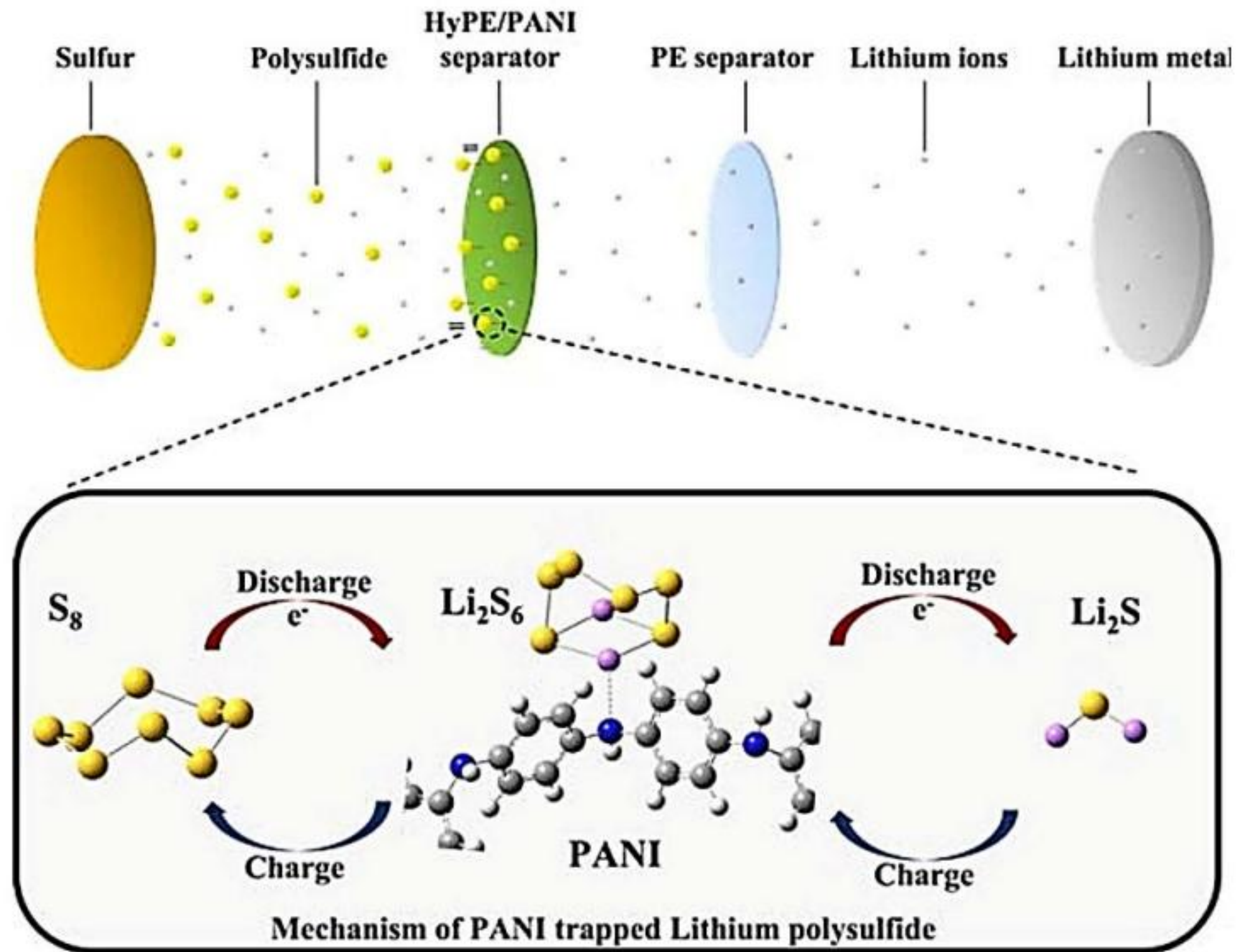
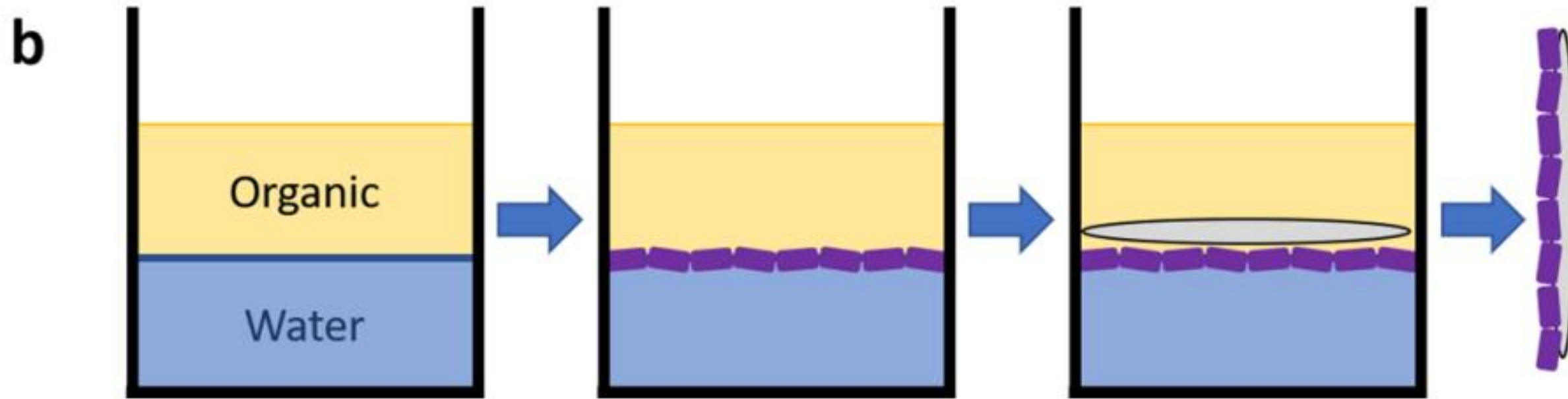
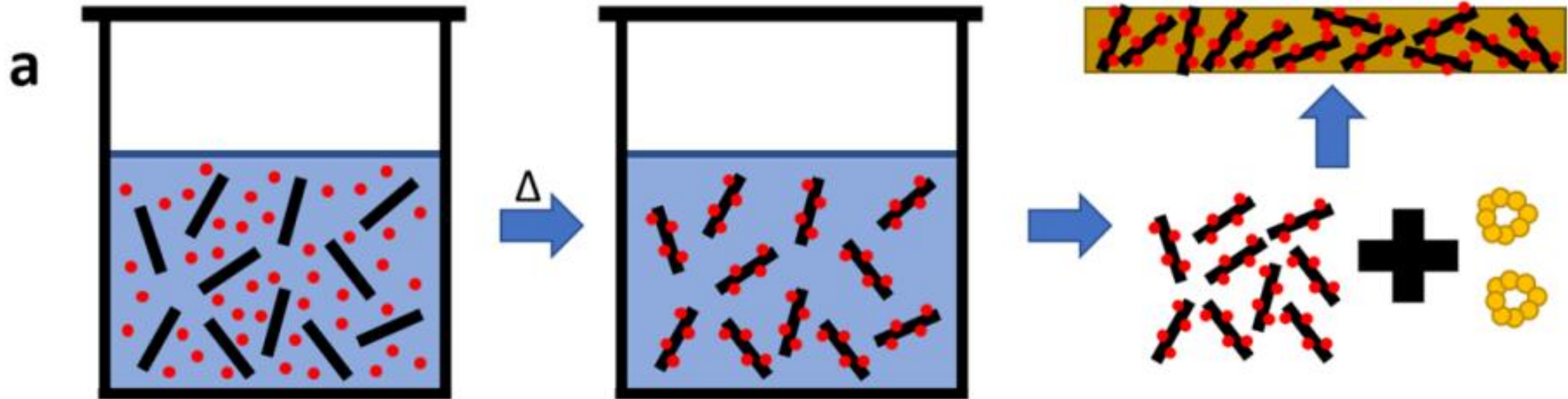


Figure 14. Li–S cell schematic with interlayer composed from hydrolysed PE and PANI. The inset displays the impact of the interlayer on the migration/diffusion of soluble PS intermediates during charge/discharge (shuttle effect). Reprinted with permission from [98]. © 2014 American Chemical Society.



12 Examples of synthesis methods leading to LIPs. (a) In addition to the described routes (13),

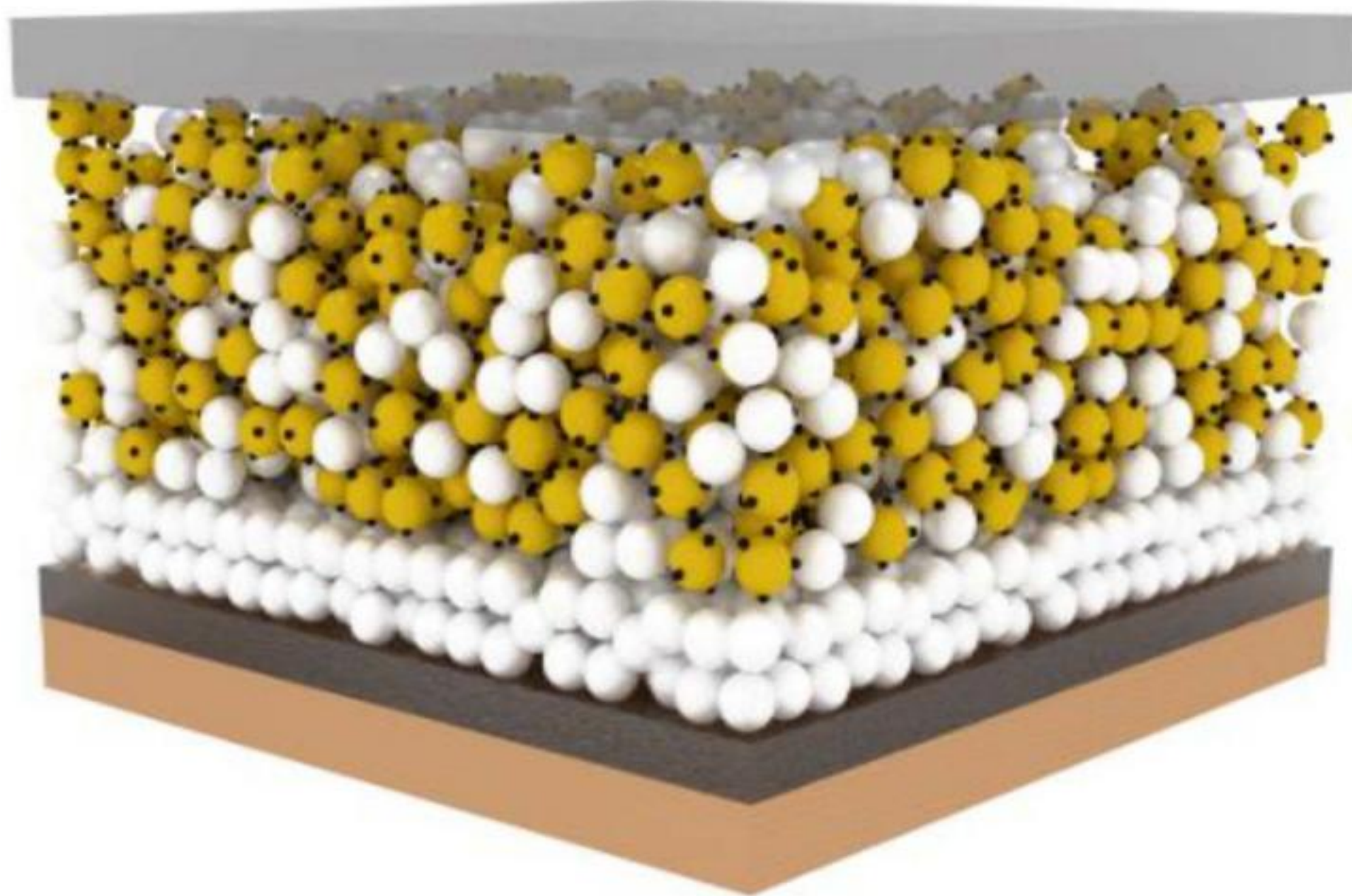
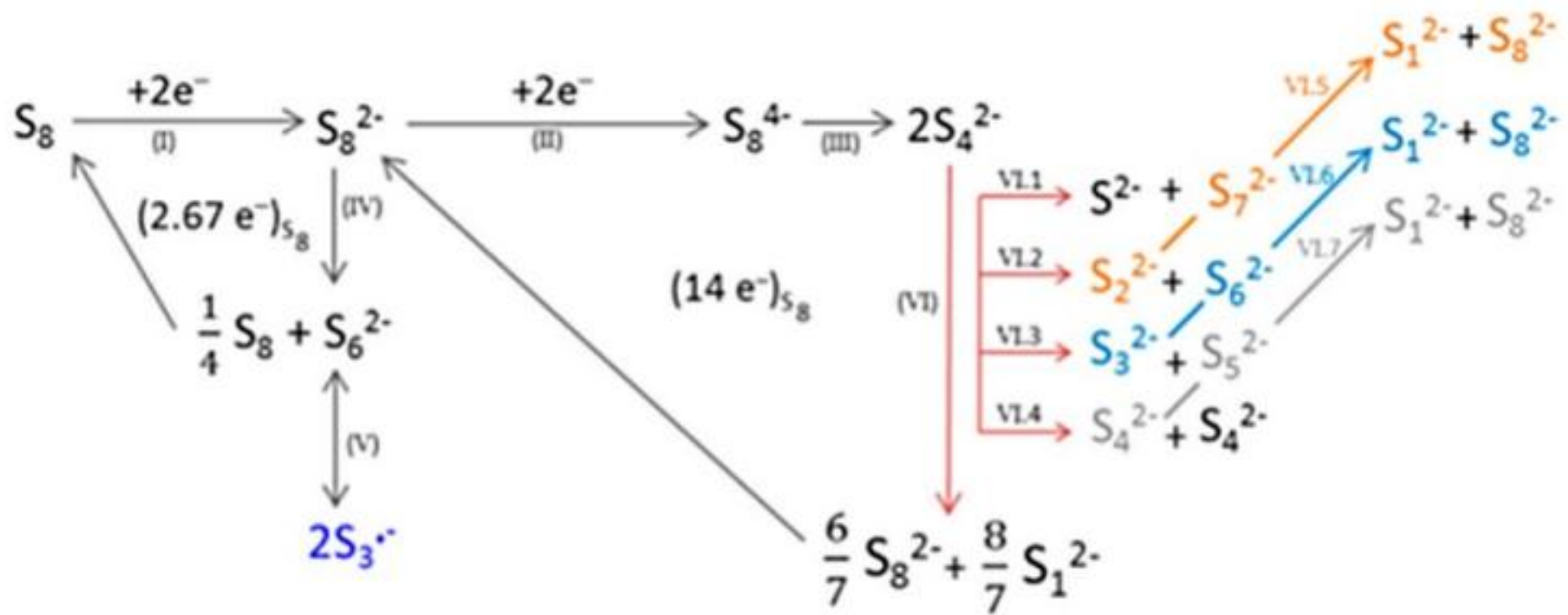
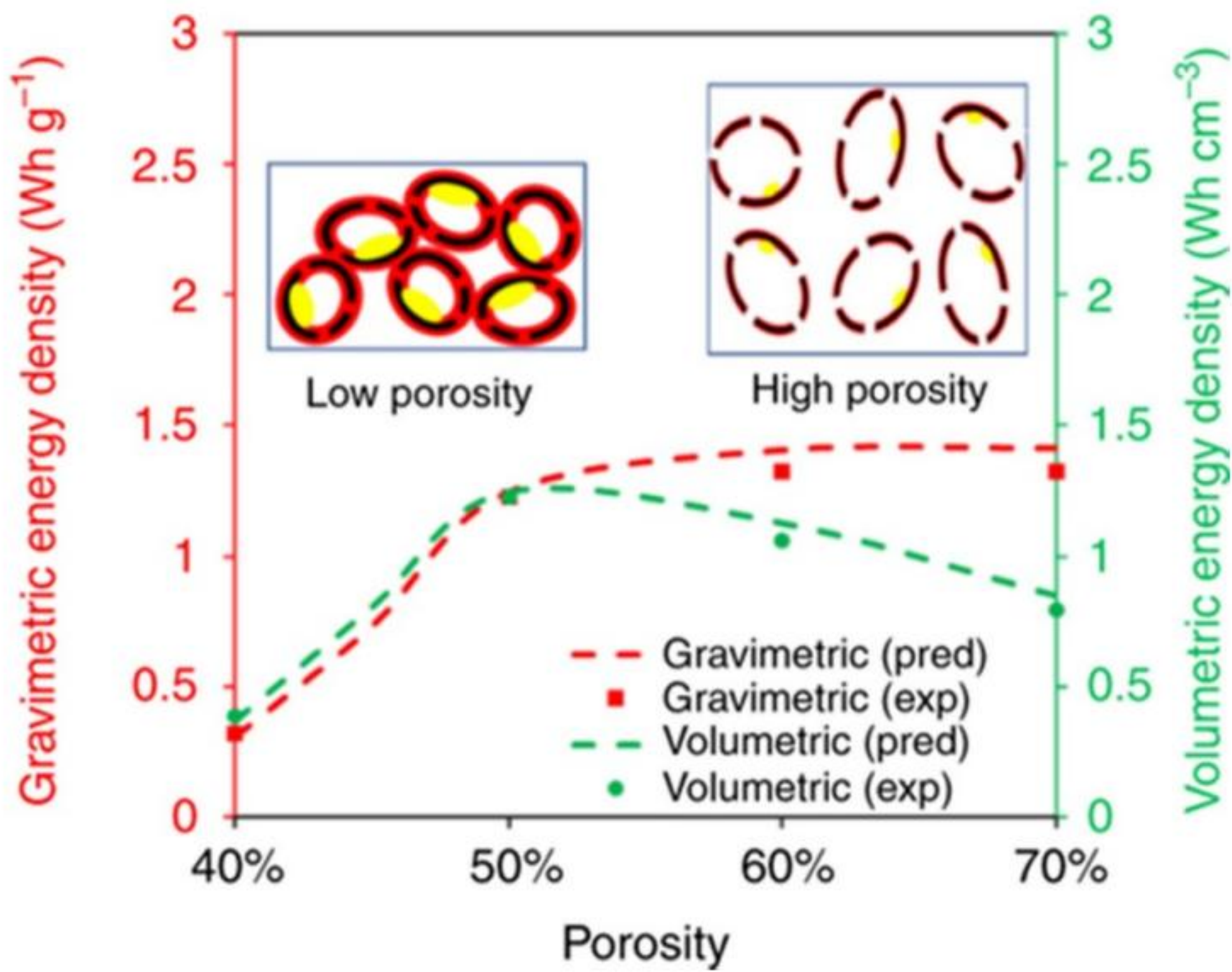


Figure 8. Illustration of an ASSLSB.





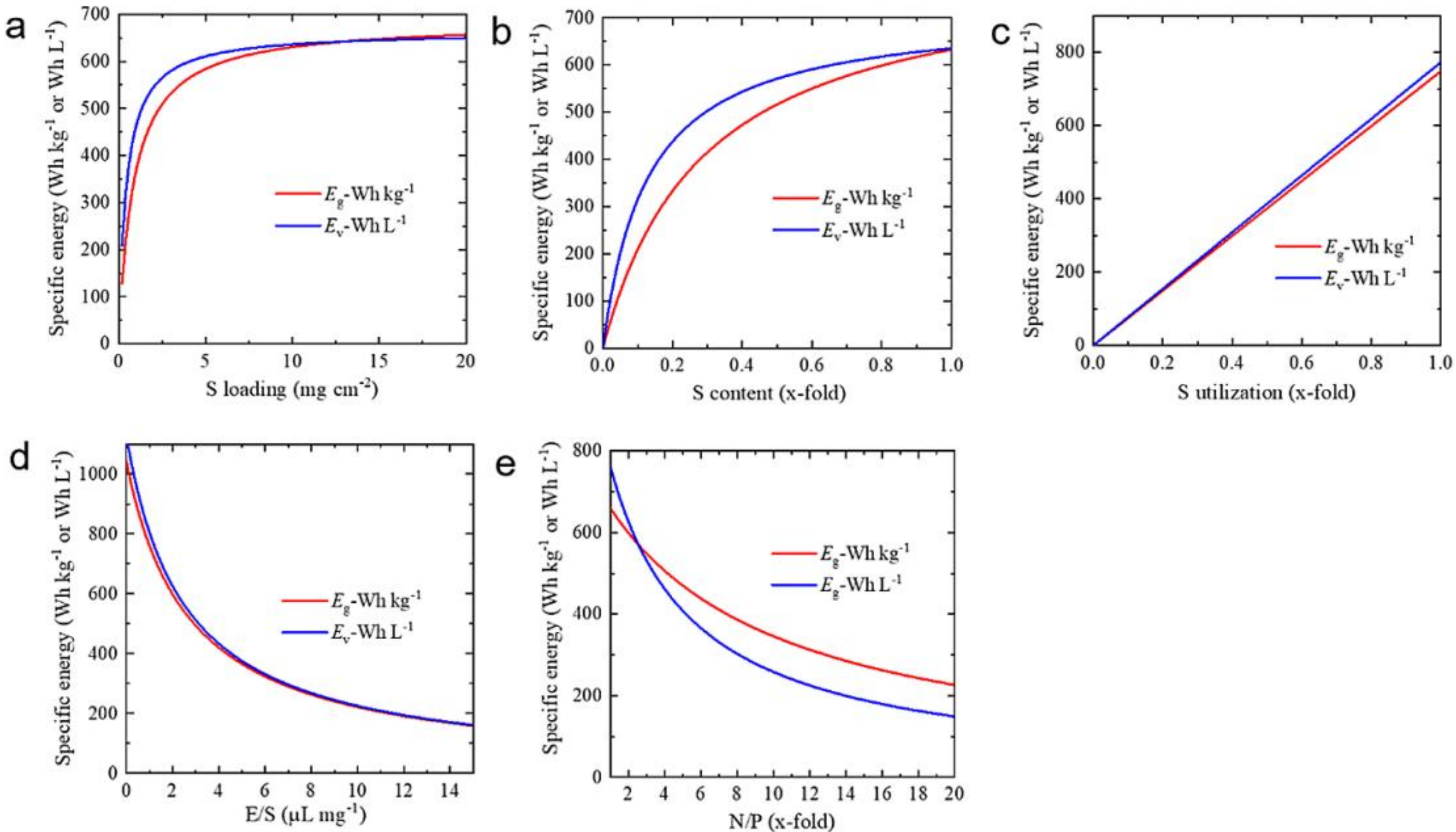


Figure 2. Predicted gravimetric and volumetric energy density from equations (1) and (2). (a) S loading, (b) S content, (c) S utilisation, (d) E/S, (e) N/P. Each graph is plotted as a function of one parameter by fixing the other four parameters. S loading:

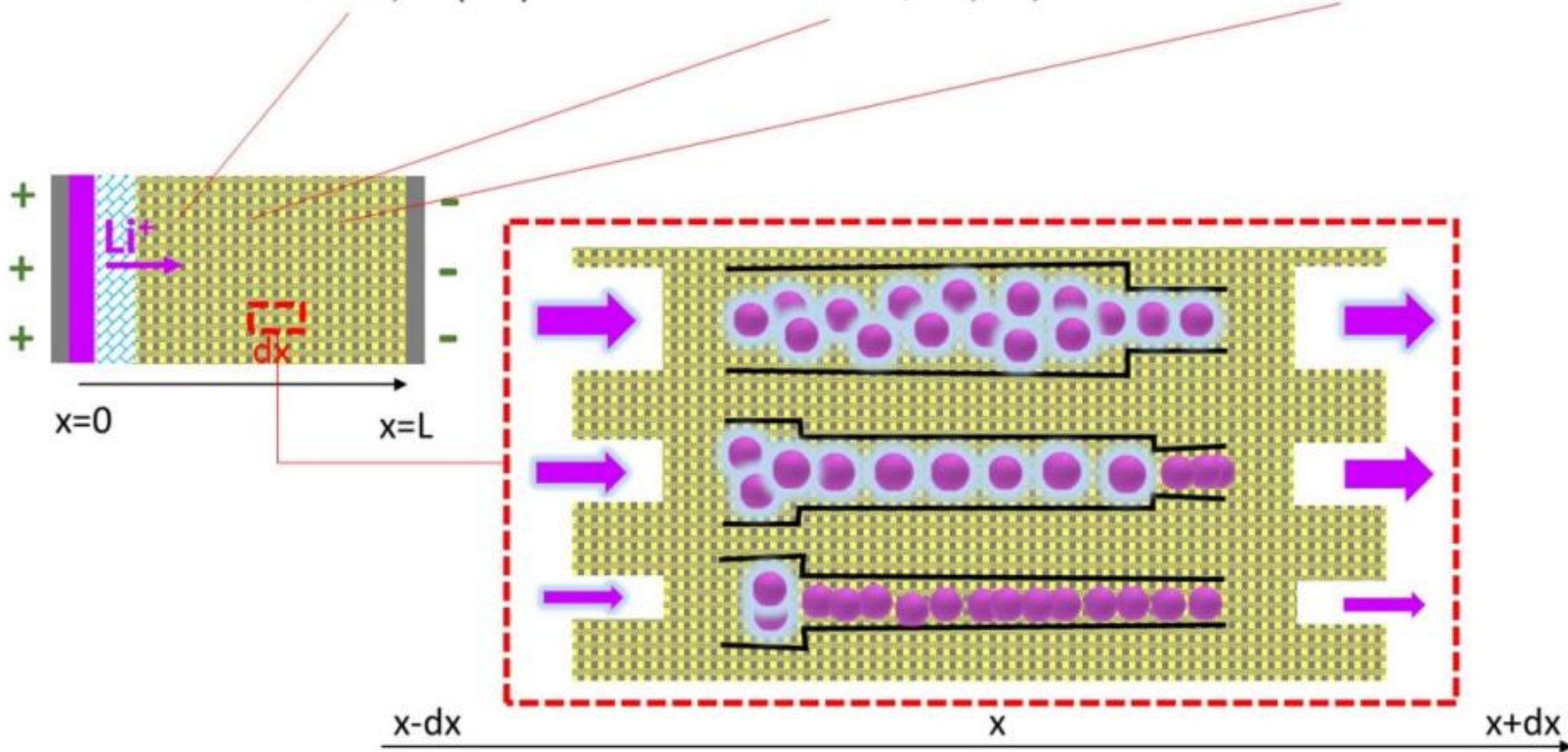
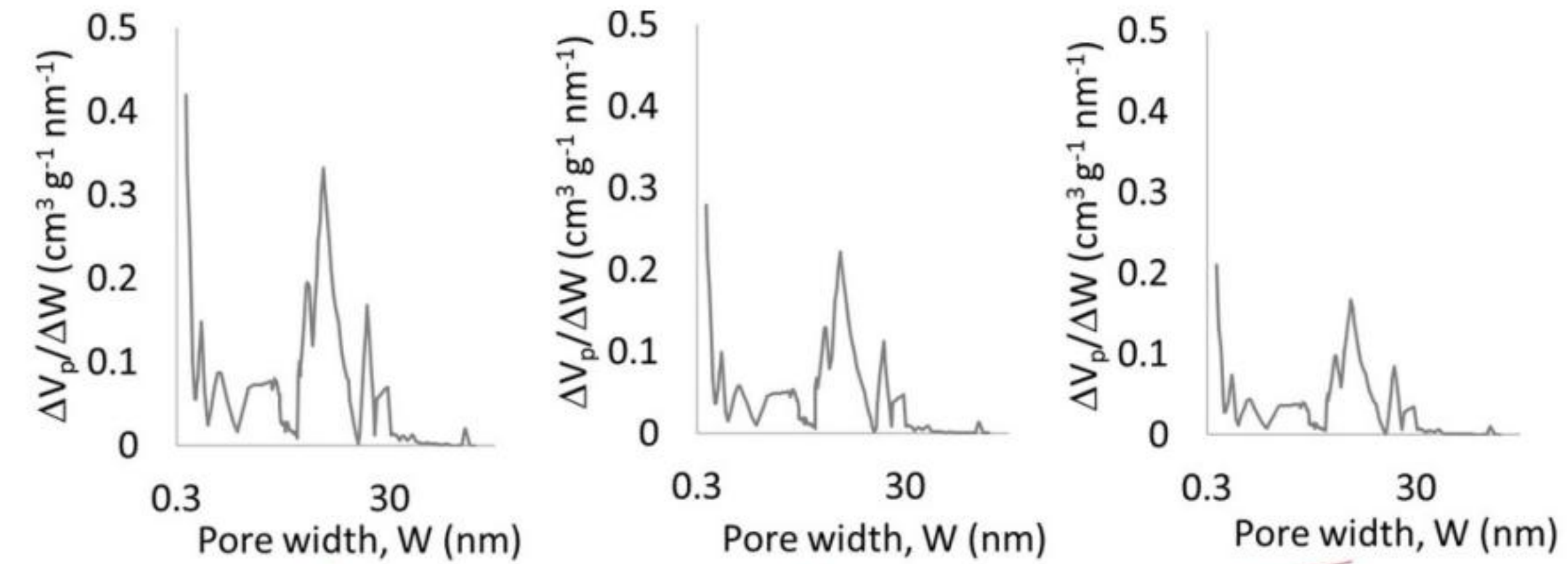


Figure 18. Diagram of continuum volume-averaged model for an electrochemical cell including anode, separator and cathode,

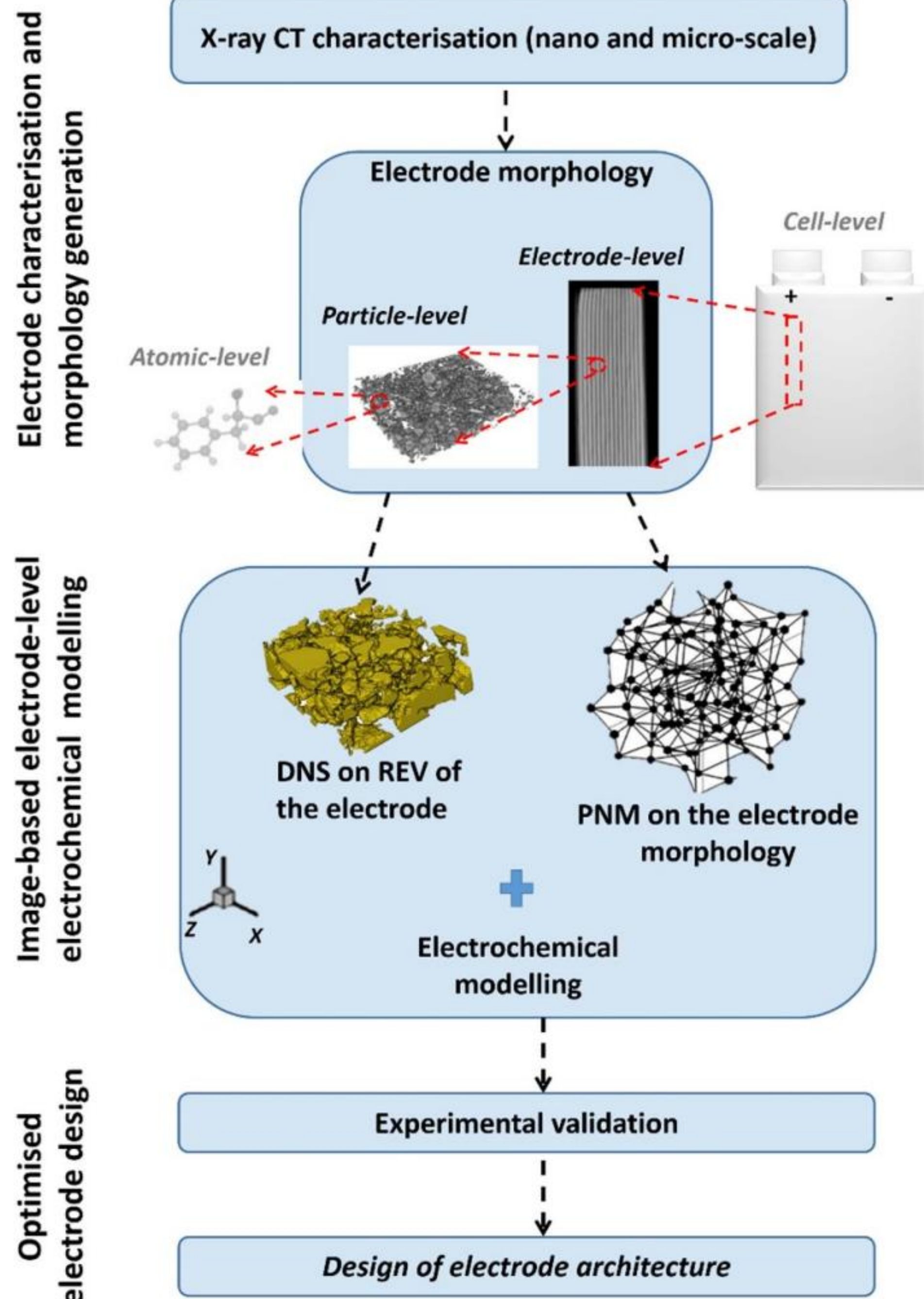
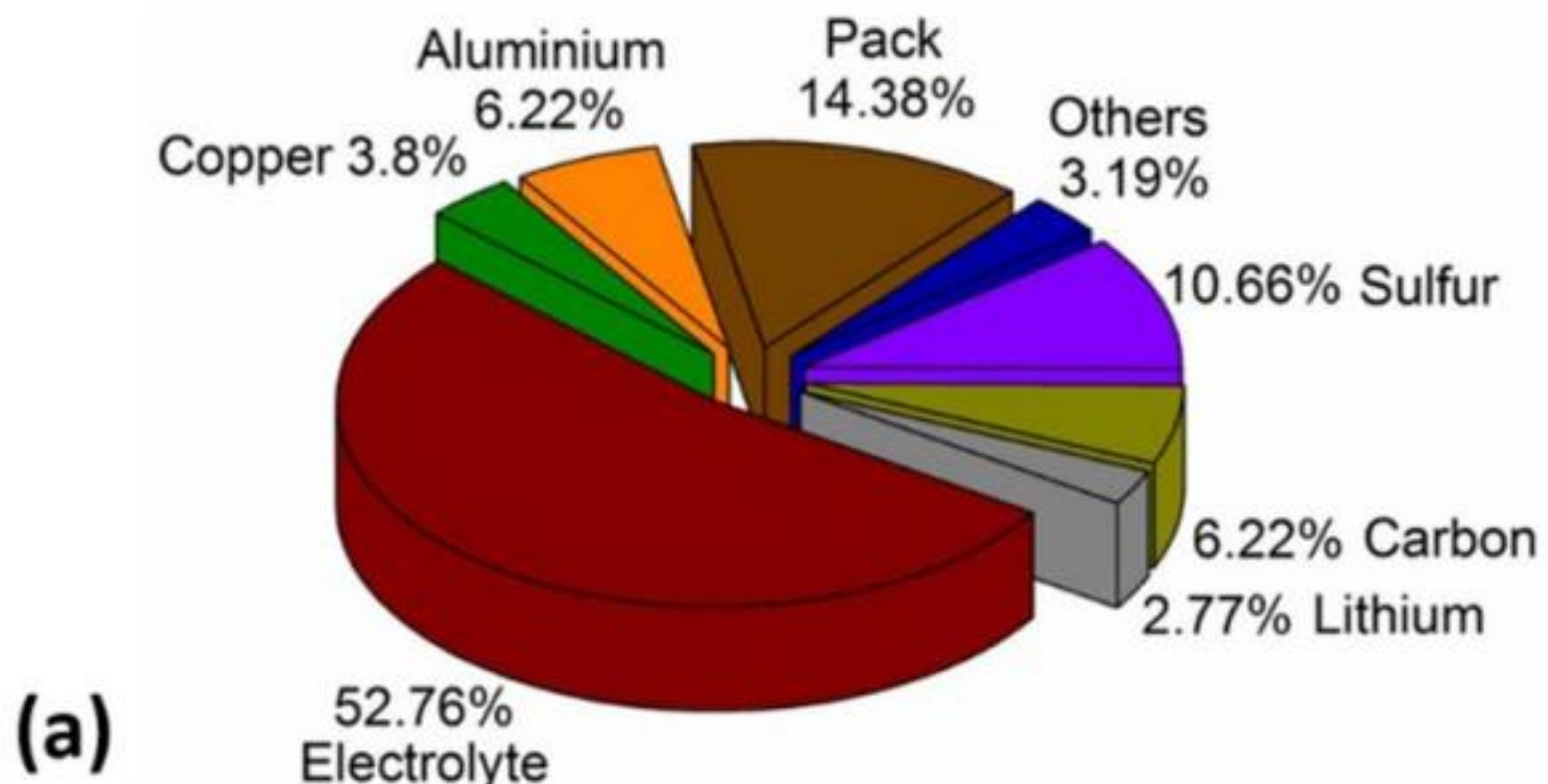


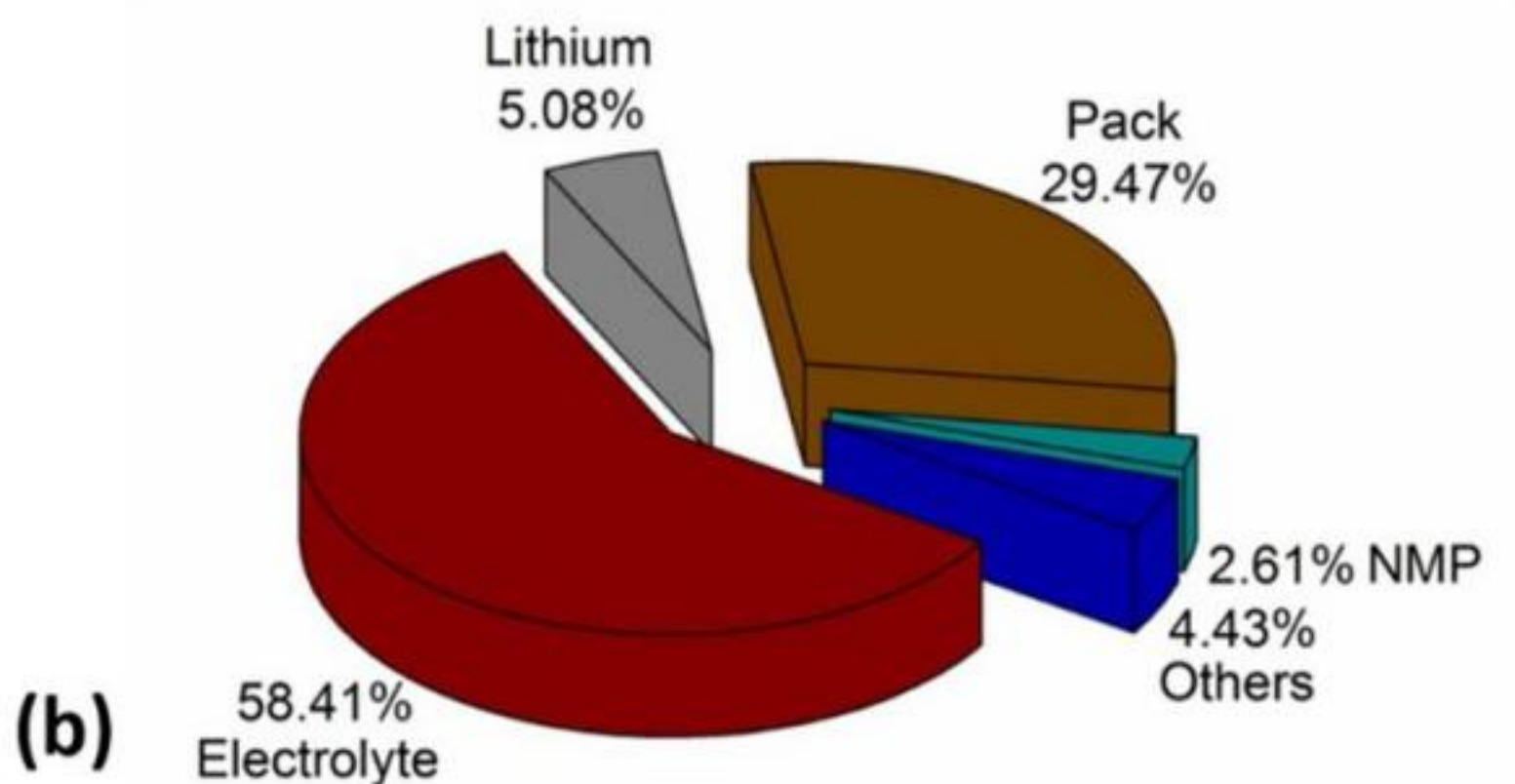
Figure 20. Roadmap of electrode-level modelling of LiS batteries to optimise electrode design, characteristics and architecture. This approach would include generation of electrode morphology using x-ray CT characterisations, combined use of electrochemical modelling with particle-level DNS models and an electrode-level PNM model to evaluate the effect of

Figure 7. Comparison of the critical solid electrolyte volume/capacity E/C ratio to the thickness of polymer, oxide, and sulfide solid electrolytes, extracted from data reported by Sun *et al* [51]. The shaded area represents the critical region of

$<5 \mu\text{l mA}^{-1}\text{h}^{-1}$.



(a)



(b)

Others	
Material	Ratio (%)
Separator	1.87
Binder	0.89
Tab	0.42

Others	
Material	Ratio (%)
Separator	1.47
Tab	1.16
Copper	0.91
Aluminium	0.41
Carbon	0.34
Binder	0.11
Sulfur	0.03

Figure 28. Typical (a) weight and (b) cost constituents of a Li–S pouch cell, illustrating areas in which cost reduction may be obtained. Adapted using data extracted from Yang *et al* [7].

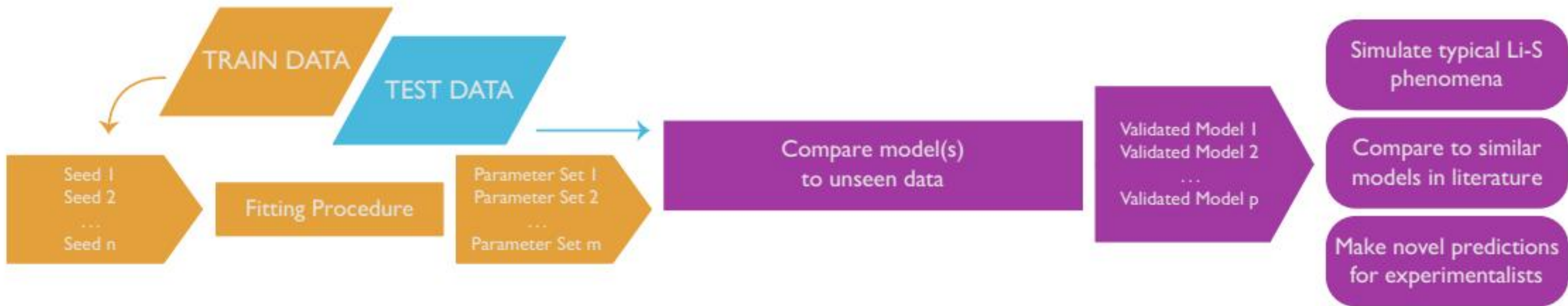
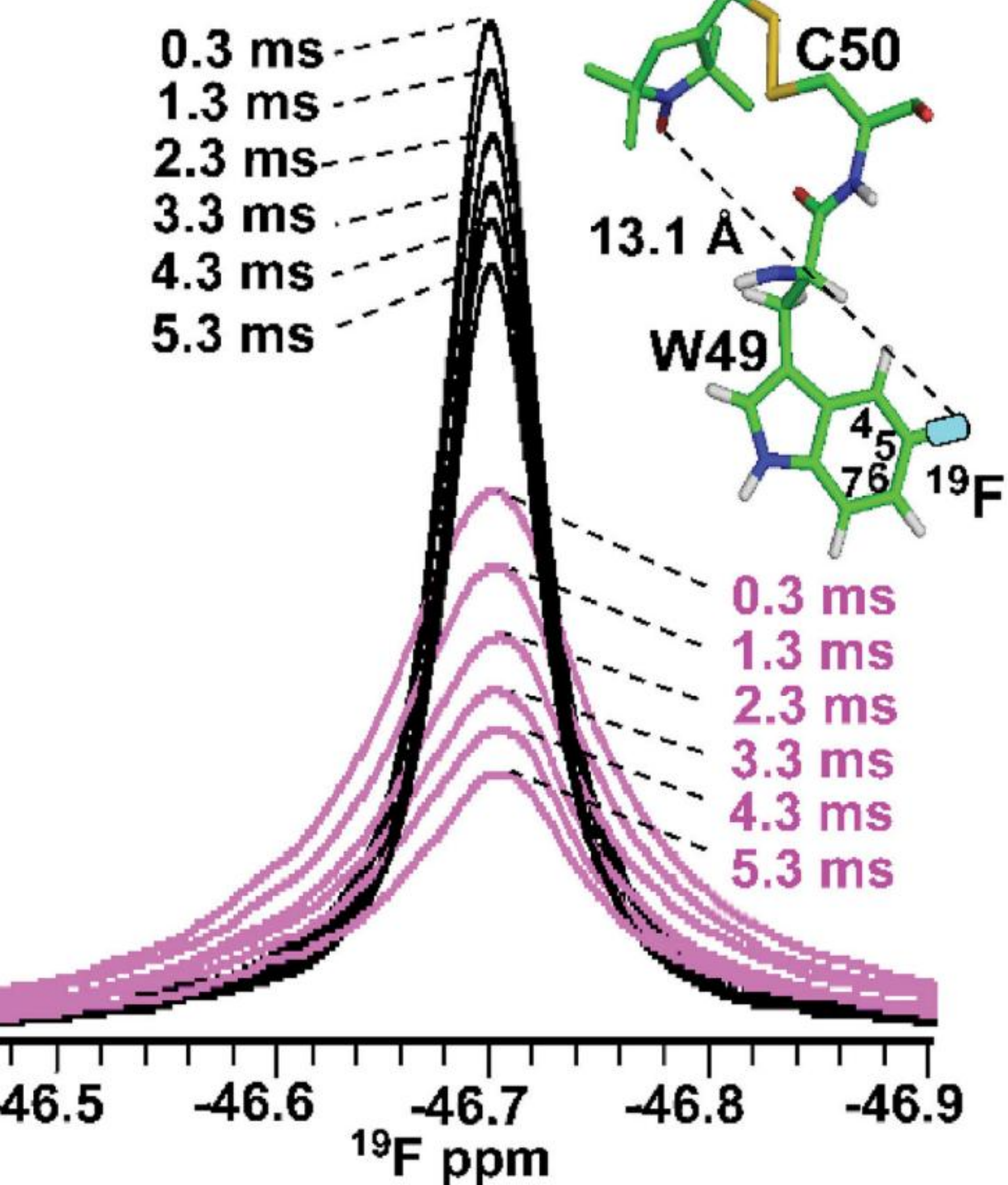
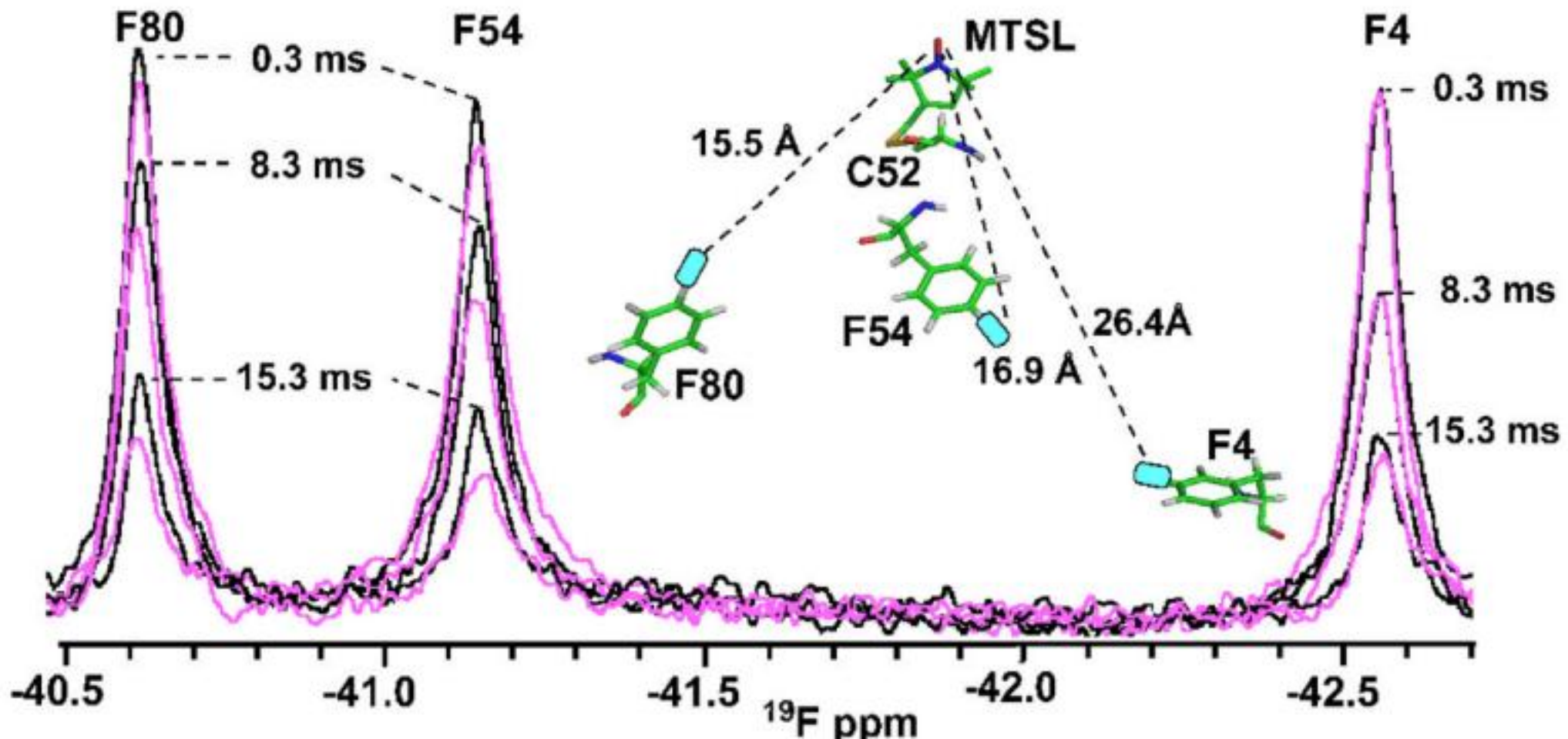


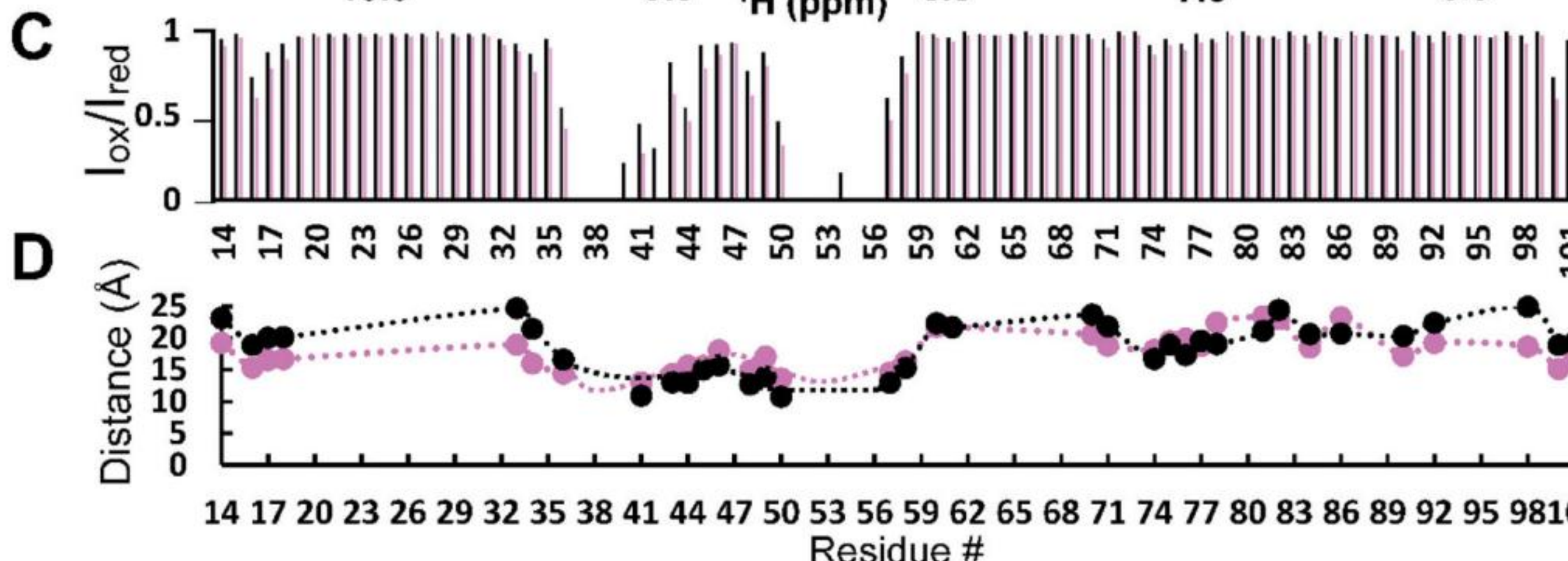
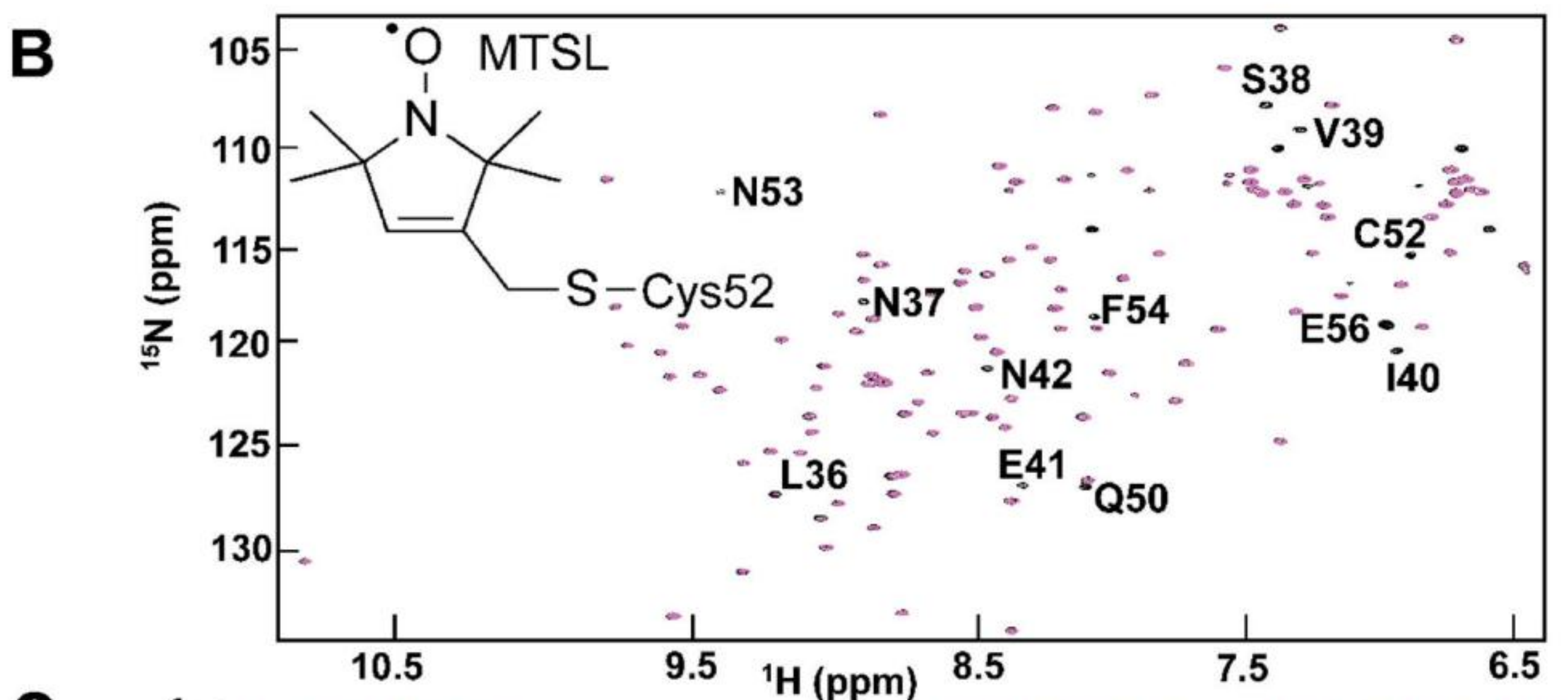
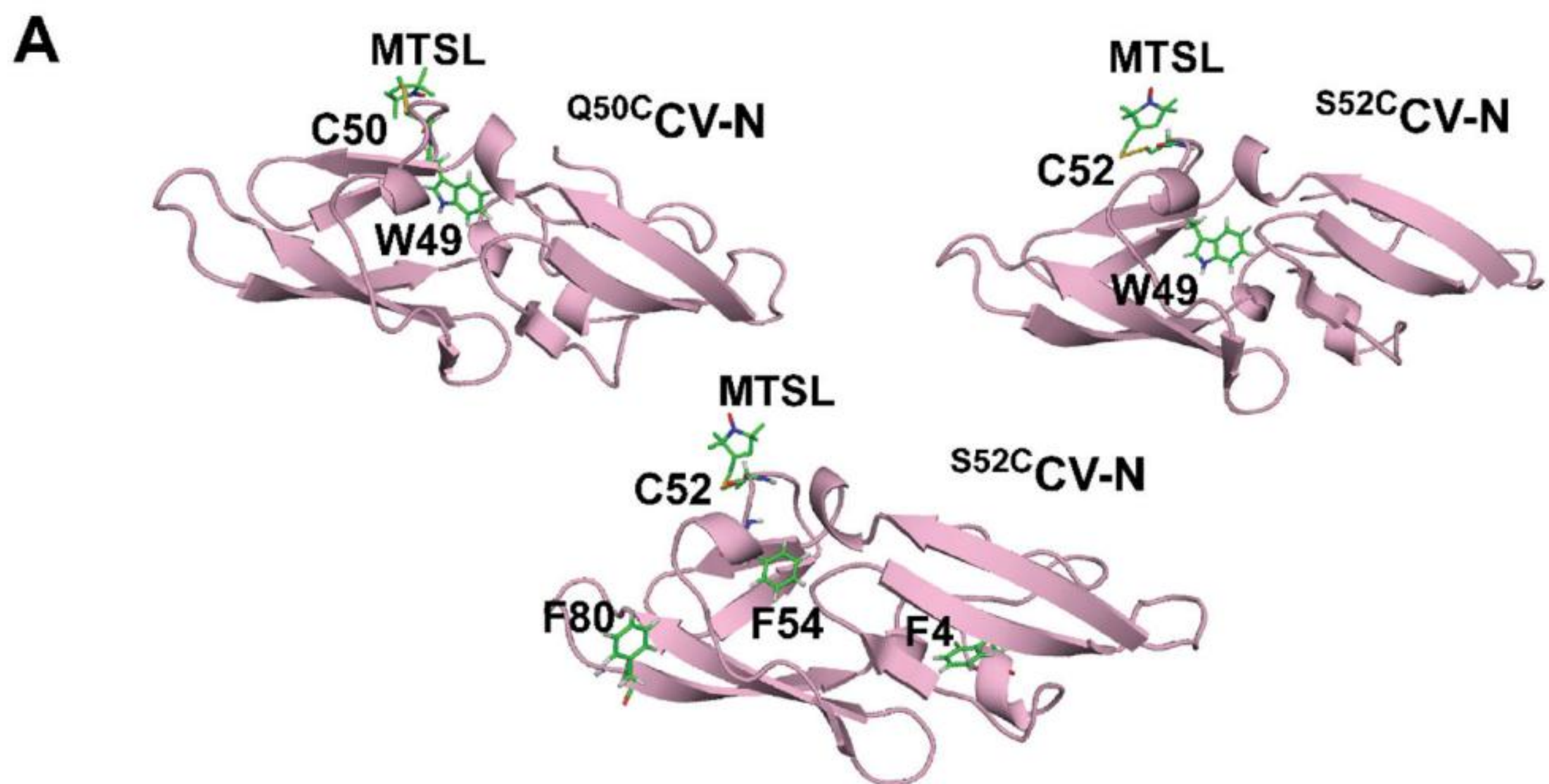
Figure 21. Model validation workflow showing the separation of empirical data into separate test and train sets. A number $n > 1$ of initial seeds to the fitting procedure are given, producing a number $m < n$ viable parameter sets. Each parameter set is then used to simulate the experiments performed to produce the test data. From the m parameter sets, a number $p < m$ will accurately model the unseen data. Each of the p parameter sets yields p models that have been appropriately validated. These models can be



MTSL

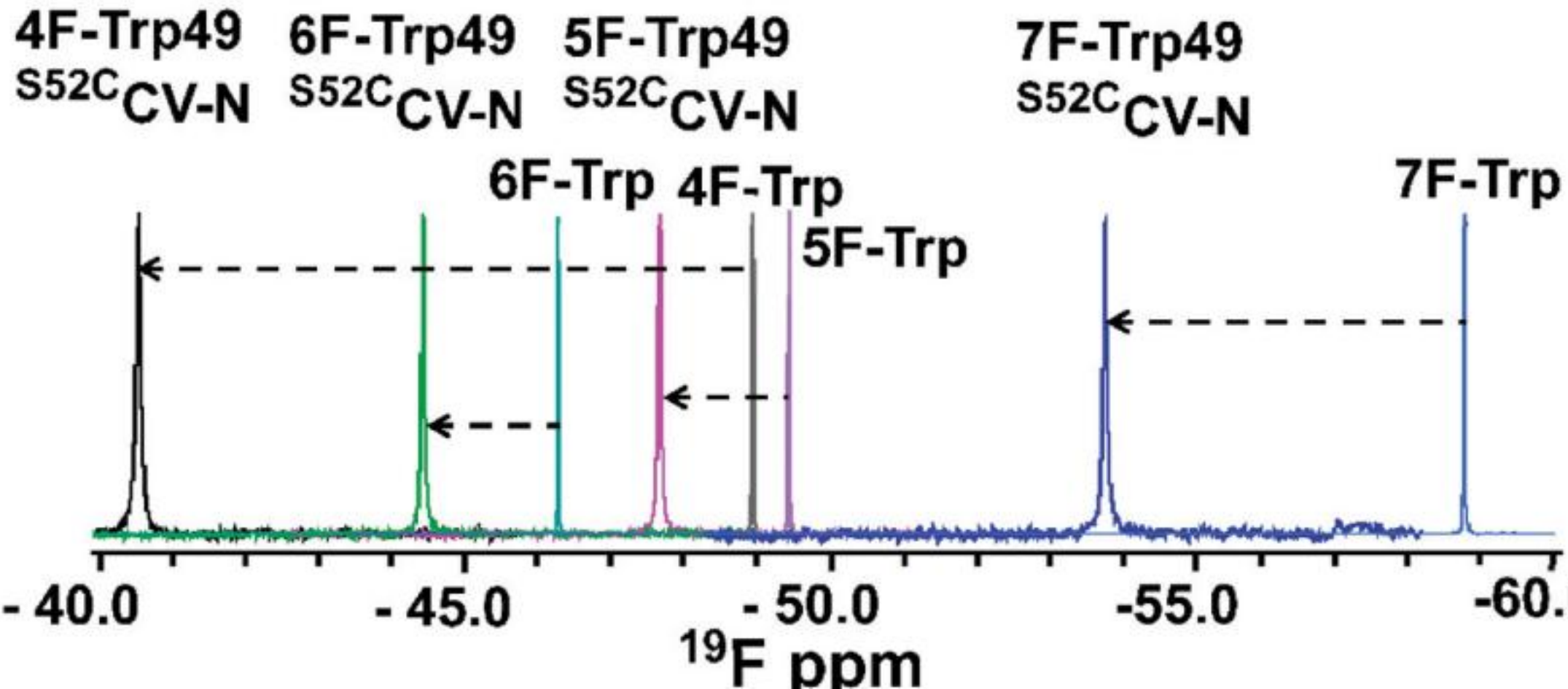




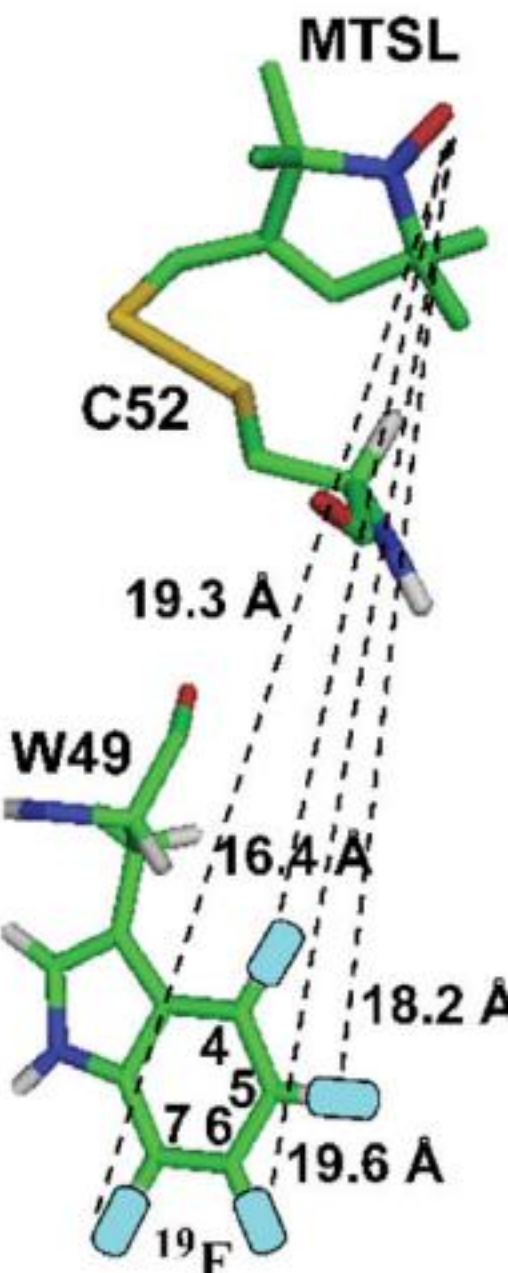
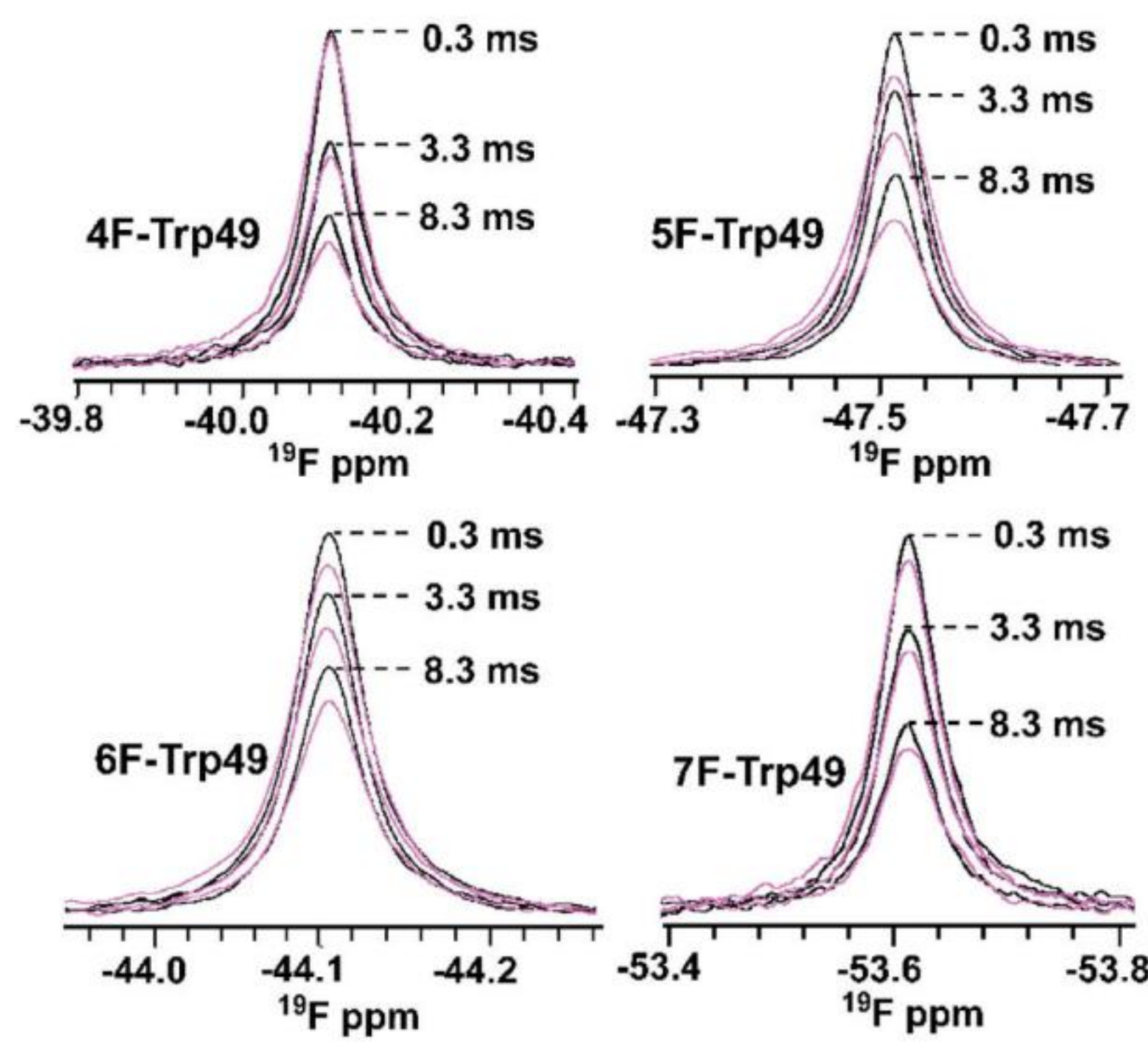


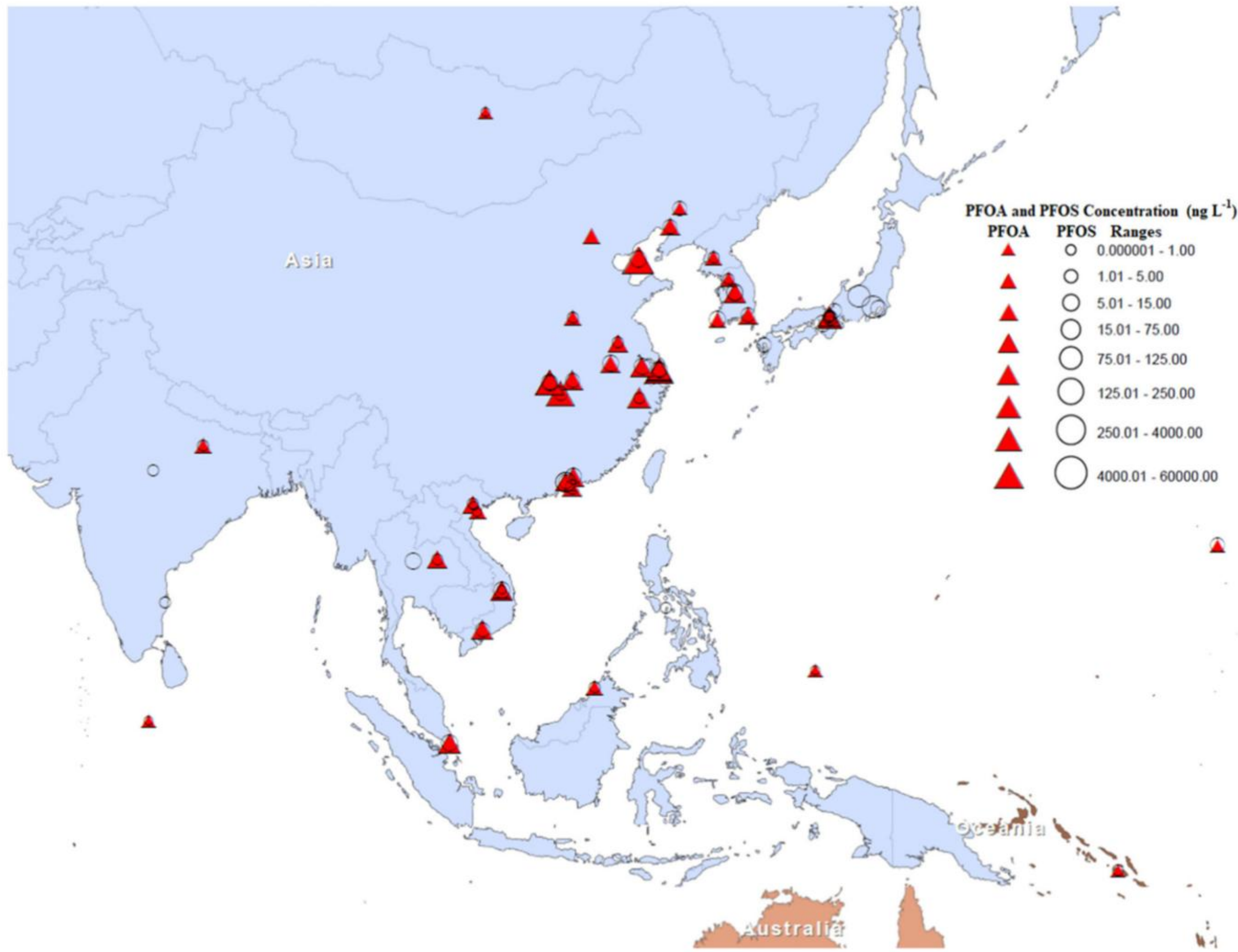


4,5,6, or 7-fluoro-Trp

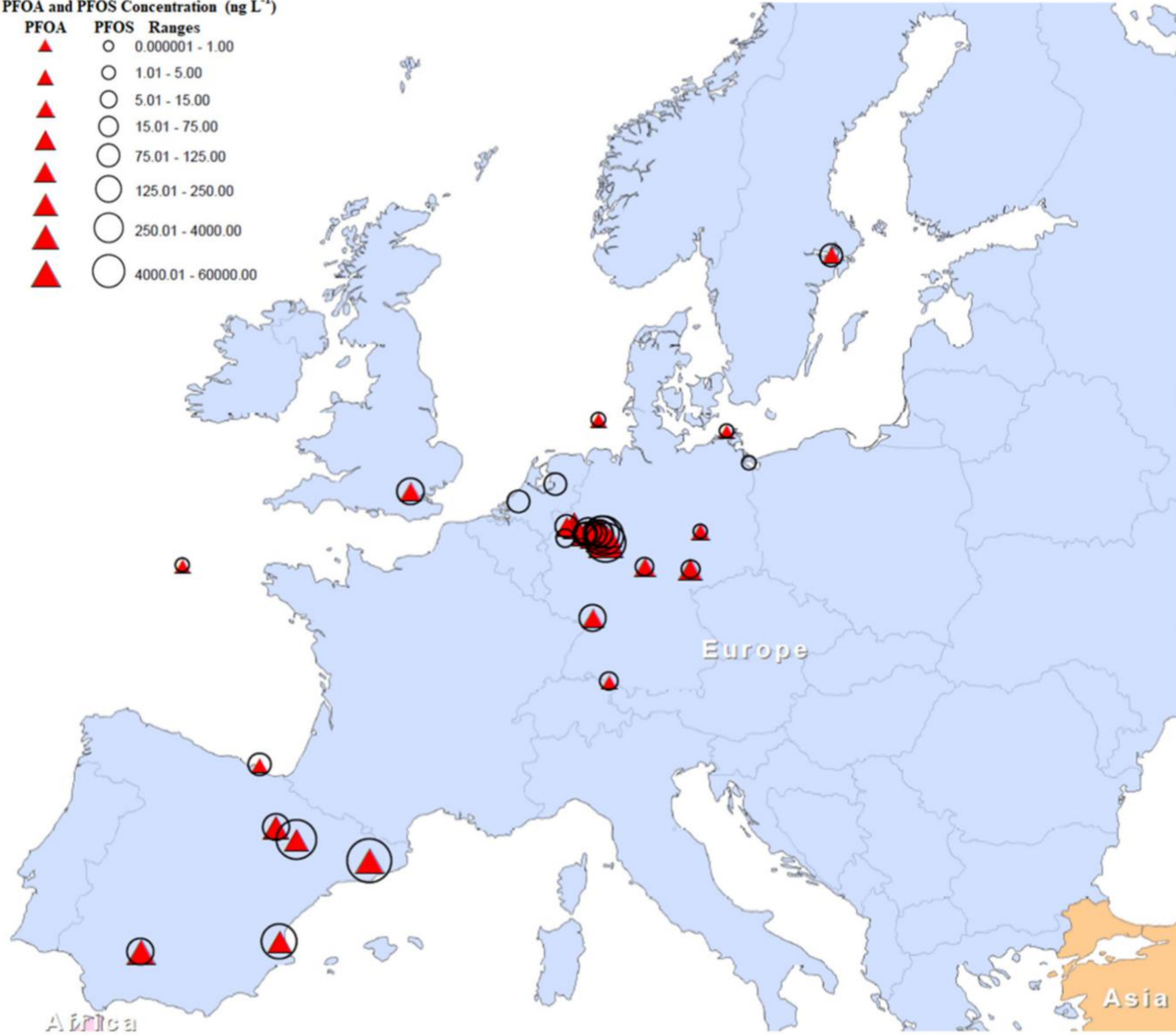
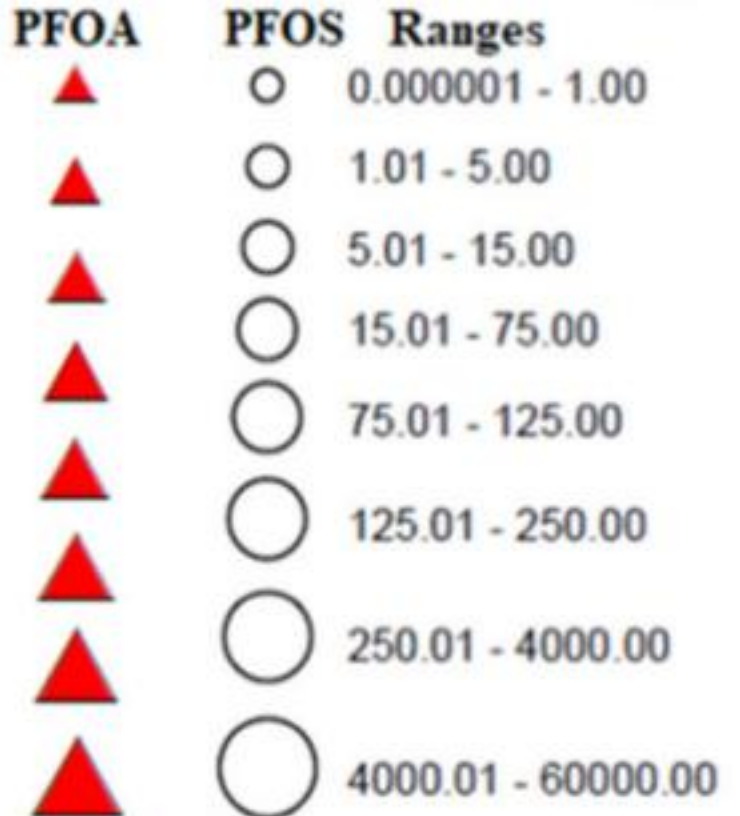




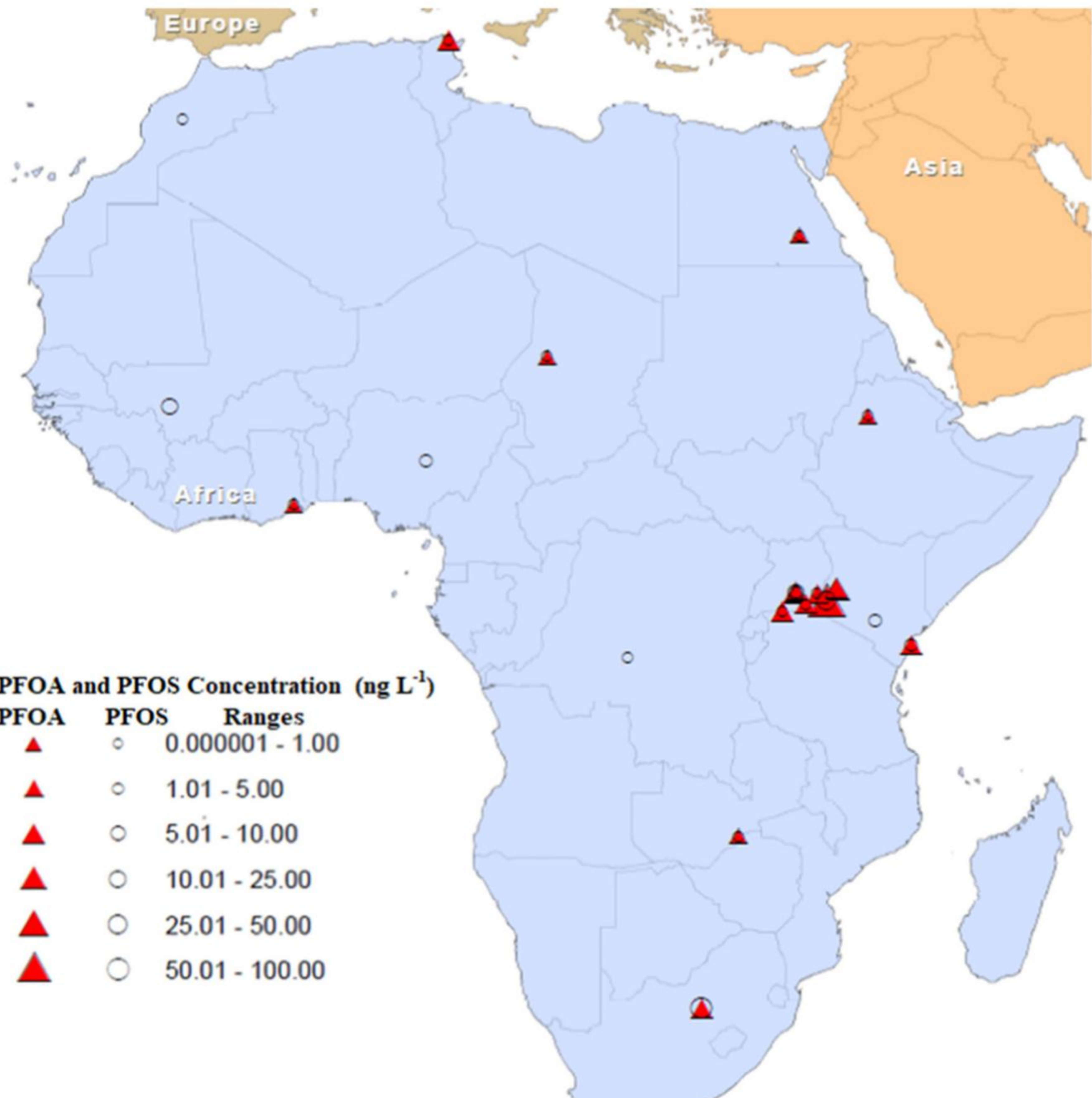




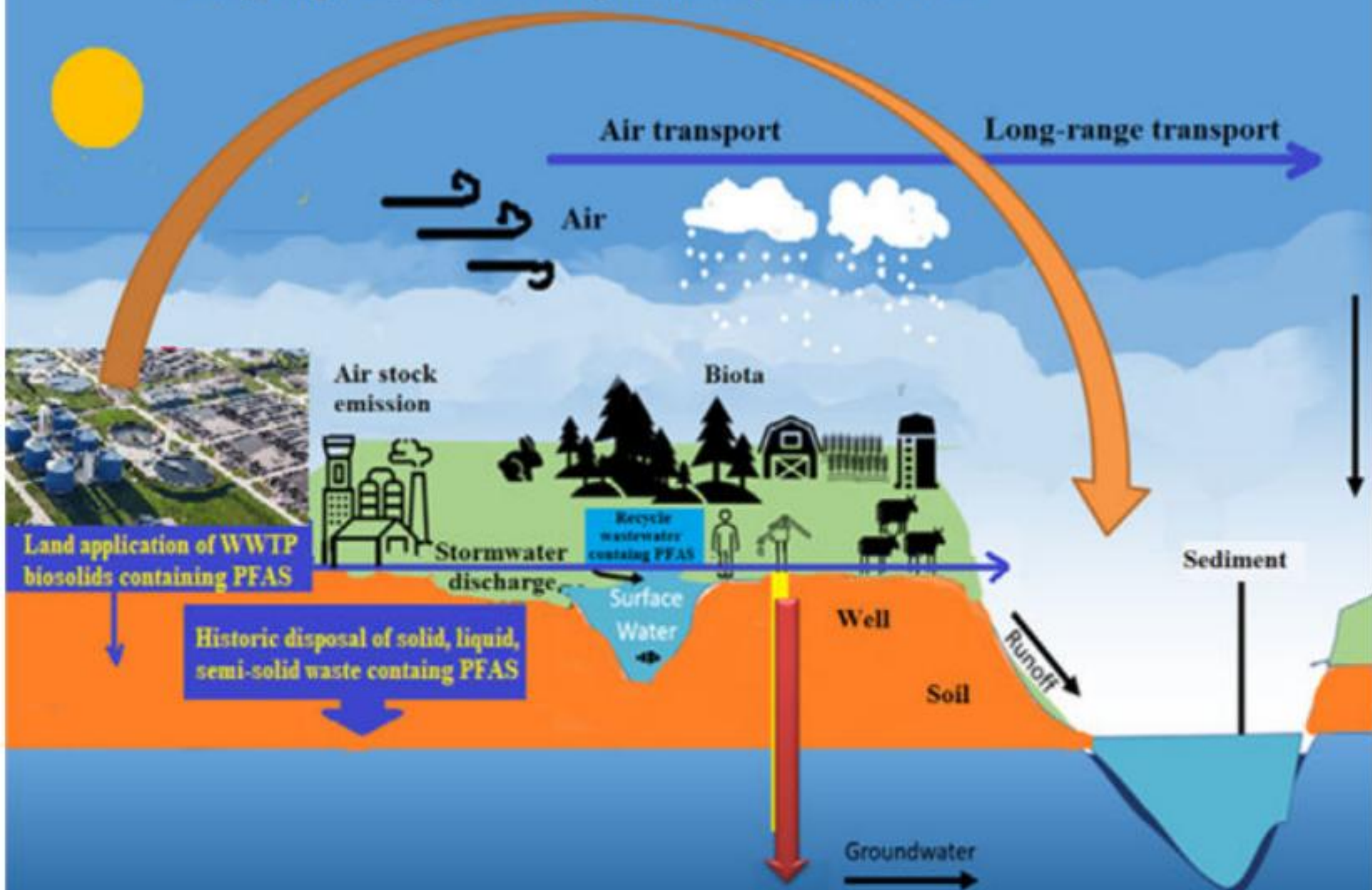
PFOA and PFOS Concentration (ng L^{-1})

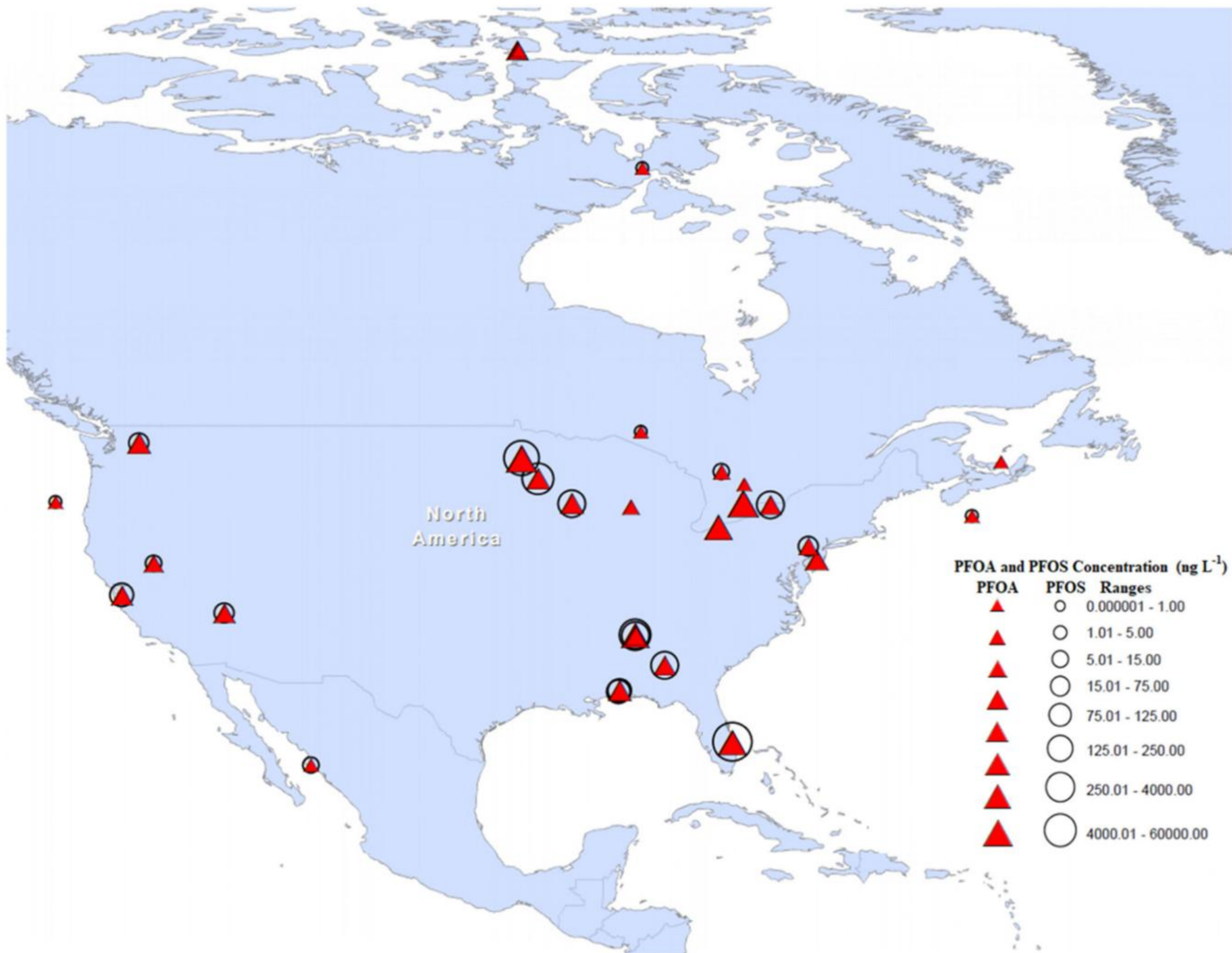




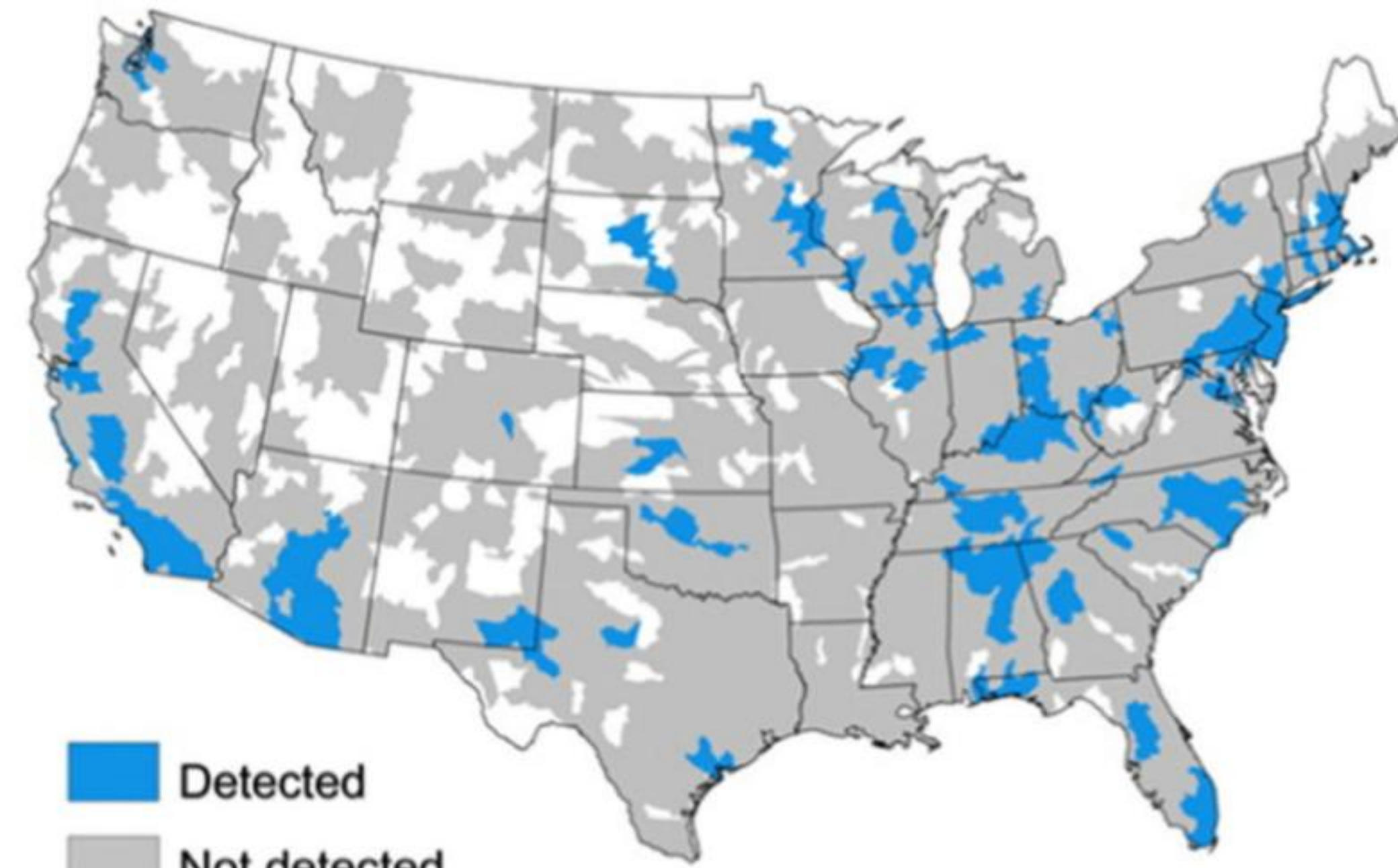


Long-range atmospheric transport and deposition of PFAS

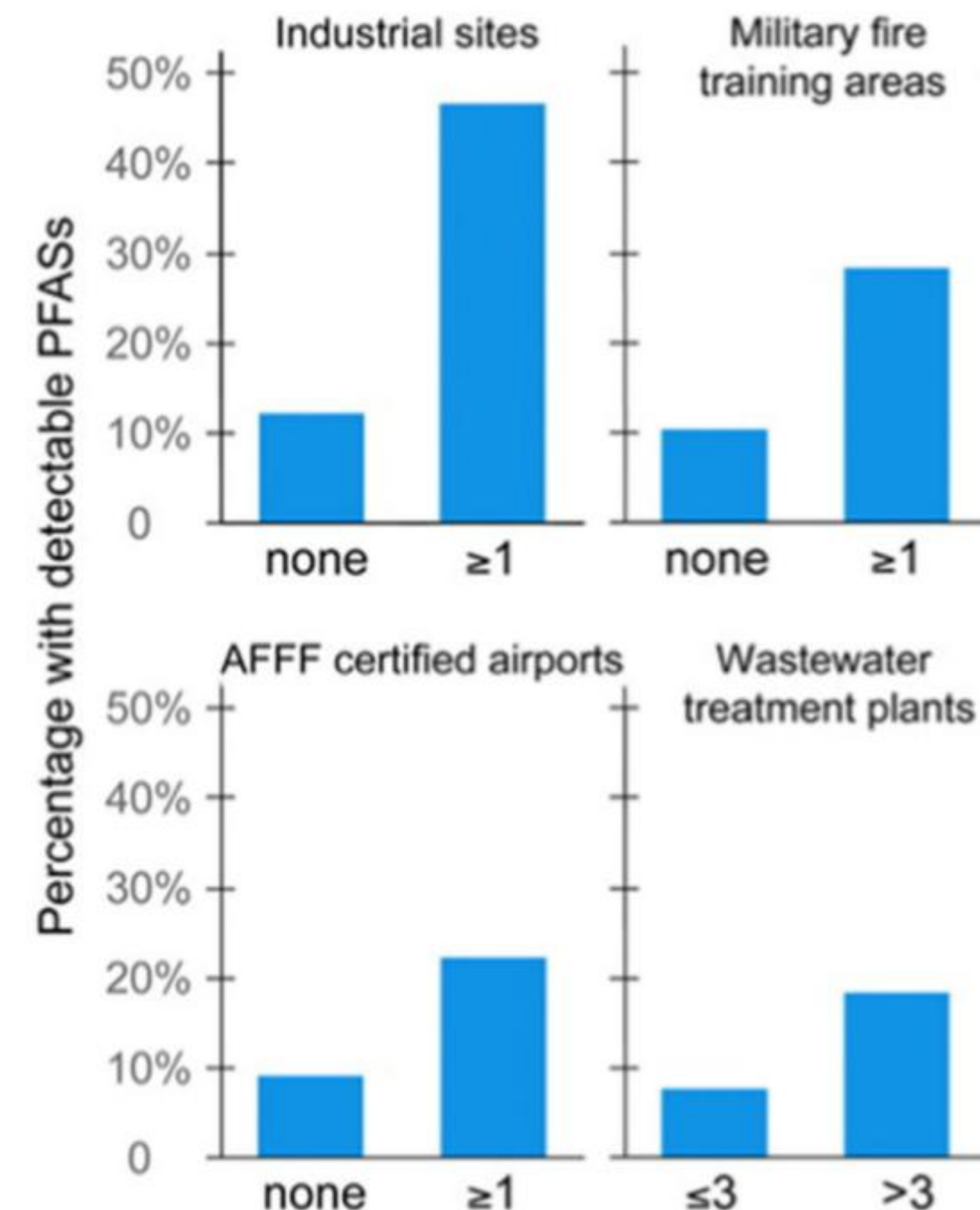


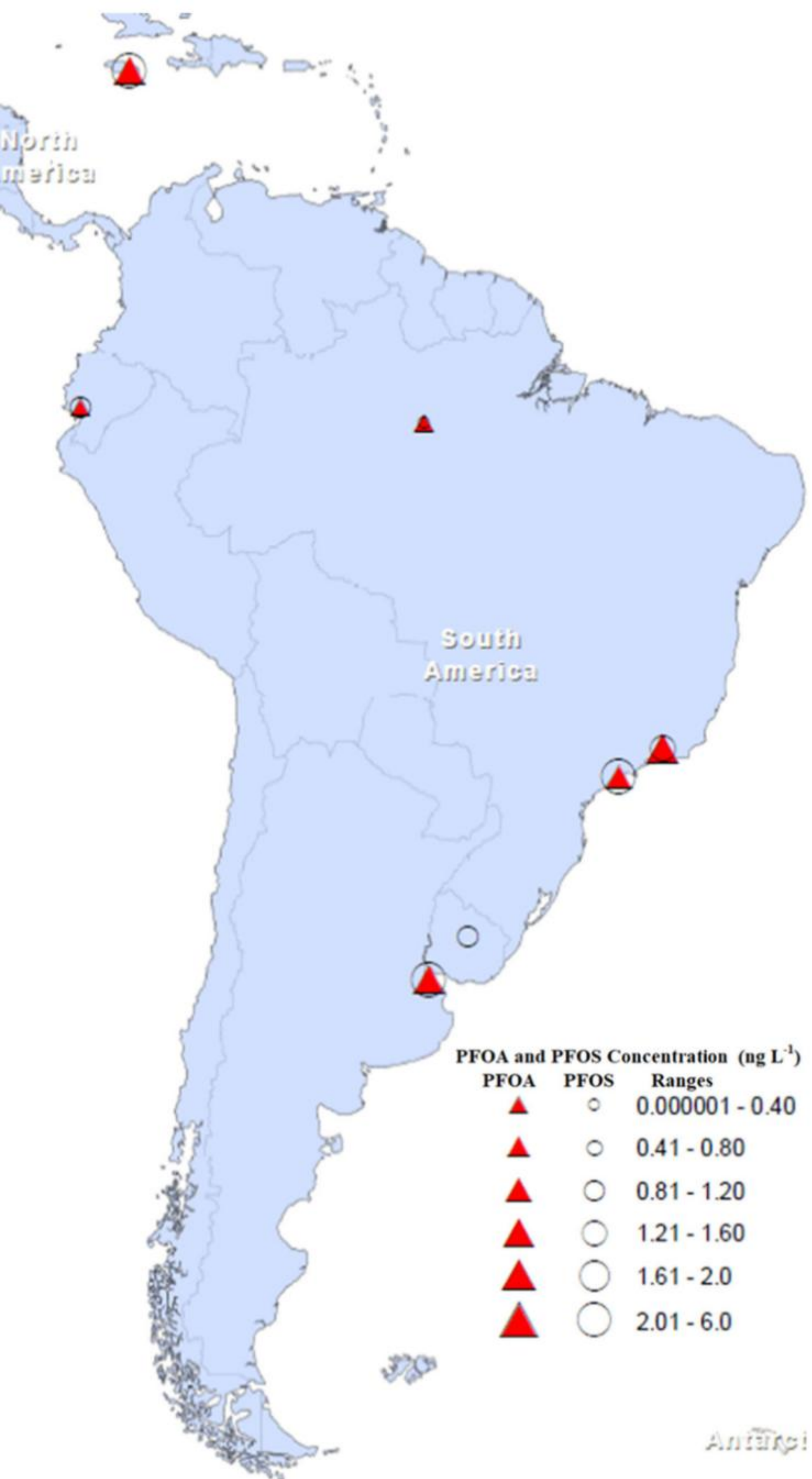


Hydrological units with detectable PFAS



Detected
Not detected
No data











NON SOLUS